

**Imperial College of Science,
Technology and Medicine
(University of London)
Department of Computing**

Quantification of Myocardial Strain Using Harp MRI

By

Fani Deligianni

**Submitted in partial fulfilment
of the requirements for the MSc
Degree in Computing Science of the
University of London and for the
Diploma of Imperial College of
Science, Technology and Medicine.**

September 2002

Contents

<i>Contents</i>	1
<i>List of Figures</i>	4
<i>Acknowledgements</i>	6
<i>Abstract</i>	7
<i>Introduction</i>	8
Chapter 1 – Heart structure and Physiology	10
1.1 <i>Introduction</i>	10
1.2 <i>Cardiac Anatomy and Physiology</i>	10
1.3 <i>Electrophysiology of the heart</i>	11
1.4 <i>Cardiac Cycle</i>	12
1.5 <i>Cardiac Gating</i>	13
1.6 <i>Myocardial Perfusion</i>	14
1.7 <i>Common Cardiovascular Diseases</i>	15
1.7.1 <i>Coronary Artery Disease</i>	15
1.7.2 <i>Myocardial Ischemia</i>	15
1.7.3 <i>Infarction</i>	16
1.7.4 <i>Myocardial Remodeling</i>	17
1.7.5 <i>Heart Failure</i>	17
1.8 <i>References and Bibliography</i>	18
Chapter 2 – Cardiac Imaging	19
2.1 <i>Introduction</i>	19
2.2 <i>Computed Tomography (CT) – Principles</i>	20
2.2.1 <i>Conventional X-Ray Images</i>	20
2.2.2 <i>From X-rays imaging to Computed Tomography (CT)</i>	21
2.2.3 <i>Cardiac CT Imaging</i>	23
2.2.4 <i>Safety considerations – Limitations of Computed Tomography</i>	24
2.3 <i>Nuclear Medicine – Principles</i>	24
2.3.1 <i>Nuclear Medicine</i>	24
2.3.2 <i>Nuclear Medicine in Cardiac Imaging</i>	25
2.3.3 <i>Safety considerations – Limitations of Nuclear Medicine</i>	26
2.4 <i>Ultrasound Imaging – Principles</i>	27
2.4.1 <i>Basic Principles</i>	27
2.4.2 <i>The Ultrasound Coordinate System – Transformation</i>	28
2.4.3 <i>Doppler Effect</i>	30
2.4.4 <i>Limitation of the Ultrasound techniques</i>	30
2.5 <i>Magnetic Resonance Imaging</i>	31
2.5.1 <i>Basic Principles</i>	31
Alignment:.....	32
Precession:.....	32
Resonance:.....	33
Relaxation:.....	33
2.5.2 <i>Gradients</i>	34
Slice selection:.....	35
Phase encoding:.....	36
Frequency encoding:.....	36
K-space:.....	36
2.5.3 <i>Advantages and Limitations</i>	37
2.6 <i>Discussion</i>	39
2.7 <i>References and Bibliography</i>	40
Chapter 3 - Quantification of Intrinsic Cardiac Mechanics	42
3.1 <i>Introduction</i>	42
3.2 <i>Eulerian and Lagrangian Strain – Strain Tensor</i>	42
3.3 <i>Strain Rate</i>	45
3.4 <i>Strain – Wall Thickening</i>	46

3.5	<i>Coordinate systems</i>	46
3.6	<i>Different Methods of Measuring Cardiac Strain Using MR</i>	47
3.6.1	<i>Non – Invasive Approaches for Measuring Myocardial Deformation</i>	48
	Correspondence Approaches:.....	48
	Velocity Fields Approaches:	49
3.7	<i>Discussion</i>	51
3.8	<i>References – Bibliography</i>	51
Chapter 4 – Myocardial Tagging with Magnetic Resonance		54
4.1	<i>Introduction</i>	54
4.2	<i>Measuring Myocardial Contractility Using MR Tagging</i>	54
4.3	<i>Spatial Modulation of Magnetisation (SPAMM)</i>	56
4.4	<i>Complementary Spatial Modulation of Magnetisation (CSPAMM)</i>	58
4.4.1	<i>Extension of CSPAMM and further improvements</i>	61
4.5	<i>Delay Alternating with Nutations for Tailored Excitation (DANTE)</i>	62
4.6	<i>Discussion</i>	63
4.7	<i>References and Bibliography</i>	63
Chapter 5 – HARP MRI		66
5.1	<i>Introduction</i>	66
5.2	<i>Introducing HARP – Basic Principles</i>	66
5.2.1	<i>Tagging MRI – Mathematical Description</i>	67
	1-D 1-1 SPAMM:	67
	2-D 1-1 SPAMM:	68
	Generalised SPAMM:	69
	CSPAMM:.....	69
5.2.2	<i>Harmonic Images</i>	70
5.2.3	<i>Tagging MRI – Signal Processing Perspective</i>	71
5.2.4	<i>Filtering of Spectral Peak</i>	73
5.2.5	<i>Apparent motion</i>	74
5.3	<i>HARP MRI – Calculating velocity fields</i>	75
5.4	<i>HARP MRI – Calculating strain fields</i>	77
5.5	<i>Discussion</i>	78
5.6	<i>References and Bibliography</i>	79
Chapter 6 – Vector Fields Restoration		81
6.1	<i>Introduction</i>	81
6.2	<i>Vector Fields Restoration</i>	81
6.3	<i>Discussion</i>	84
6.4	<i>References and Bibliography</i>	84
Chapter 7 – Experiment Setup and Results		86
7.1	<i>Introduction</i>	86
7.2	<i>Overview</i>	86
7.3	<i>Scanning Sequence and Various Parameters</i>	88
7.4	<i>From raw data to HARP Images</i>	90
7.4.1	<i>Reconstruction of Complex Images</i>	90
7.4.2	<i>Reconstruction of CSPAMM – Fourier Domain</i>	91
7.4.3	<i>Band-pass Filter – Harmonic Images</i>	91
7.4.4	<i>Angle Image – Wrapping effects</i>	92
7.5	<i>Calculating Velocity Fields Using Harmonic Phase Images</i>	92
7.5.1	<i>Derivatives – Median Filter</i>	92
7.5.2	<i>Unwrapping the subtraction of two successive frames</i>	93
7.5.3	<i>Velocity Fields</i>	93
7.6	<i>Calculating Strain Fields Using Harmonic Phase Images</i>	94
7.6.1	<i>Principal Eigenvalue and Eigenvector</i>	94
7.7	<i>Eliminating noise – Mask</i>	94
7.8	<i>Restoration of Vector Fields</i>	95
7.9	<i>Results</i>	96
7.9.1	<i>Comparing SPAMM and CSPAMM velocity fields</i>	96
7.9.2	<i>Based on CSPAMM: Comparing patient data and normal data</i>	96

Velocity Fields:.....	96
Strain Maps:.....	97
7.10 Discussion.....	98
Chapter 8 – Conclusions and Future Work.....	118
8.1 Summary.....	118
8.2 Future Work.....	121
Appendix – Implementation.....	123
1. Introduction.....	123
2. Interface.....	123
2.1. Main Application.....	123
2.2. Tab Controls.....	126
Info Tab:.....	127
Velocity Tab:.....	127
Scale Tab:.....	128
Zoom Tab:.....	129
3. Description of the Object Orientated Model.....	131
3.1. Manipulating MRI Image Data.....	131

List of Figures

<i>Figure 1.1: Cardiac Anatomy [Masood02]</i>	11
<i>Figure 1.2: a) Cardiac Electrophysiology, [Masood02], b) The conduction system, [http://www.tmc.edu/thi/conduct.html], c) Electrocardiogram</i>	13
<i>Figure 2.1: Cardiovascular Imaging: a) Computed Tomography, b) Nuclear Medicine, c) Ultrasound, d) Magnetic Resonance</i>	20
<i>Figure 2.2: Ultrasound Coordinate system</i>	28
<i>Figure 2.3: Resonance of hydrogen nucleus in a magnetic field B_0</i>	31
<i>Figure 3.1: Deformation of a 3D object: a) Normal strain e_x, b) Shear strain e_{xy}</i>	45
<i>Figure 3.2: Global - Local Coordinate systems</i>	46
<i>Figure 4.1: a) Horizontal tags, b) Vertical Tags</i>	54
<i>Figure 4.2: a) Time frame 2/16, b) Time frame 7/16, c) Time frame 11/16, d) Time frame 15/16</i>	56
<i>Figure 4.3: Time frame 8/16 (ABS) - a) Before CSPAMM subtraction</i>	58
<i>Figure 5.1: Fourier Transform – a) SPAMM spectrum, b) CSPAMM spectrum</i>	69
<i>Figure 5.2: Spectral Peak Filtering – a) Fourier domain of CSPAMM and filter, b) Corresponding Harmonic Image</i>	73
<i>Figure 5.3: Apparent Motion</i>	74
<i>Figure 5.4: Wrapping effects – a) Relationship between the subtraction of wrapped and unwrapped images, b) Wrapped angle of Harmonic Image, c) Subtraction of two angle images of successive frames, d) Unwrapping the subtraction of the two angle images</i>	75
<i>Figure 5.5: Strain eigenvectors and eigenvalues – The circle is transformed to ellipse by homogeneous motion</i>	77
<i>Figure 6.1: Vector Fields Restoration</i>	82
<i>Figure 7.1: a) Overview, b) Short axis View of normal data, c) Short axis View of patient data, d) Colour-map used</i>	86
<i>Figure 7.2: Scanning Sequence a) Horizontal Tags, b) Vertical Tags</i>	88
<i>Figure 7.3: Raw data a) Magnitude image, b) Phase image</i>	90
<i>Figure 7.4: Geometrical inconveniences a) Vertical Tags, b) Horizontal Tags</i>	90
<i>Figure 7.5: Angle Images of 4th frame a) Horizontal Tags, b) Vertical Tags</i>	92
<i>Figure 7.6: The subtraction of two subsequent angles images a) Before Unwrapping, b) After unwrapping</i>	93
<i>Figure 7.7: a) Velocity Field Before Filtering, b) Mask, c) Velocity Field After Filtering</i>	94
<i>Figure 7.8: Average value for the anterior/septal region in both patient and normal. The difference in the two values can be seen although the trend of the strain development through the cardiac cycle is similar</i>	98
<i>Figure 7.9: CSPAMM and SPAMM Magnitude Images a-b) 3rd Time Frame, c-d) 9th Time Frame, e-f) 12th Time Frame</i>	100
<i>Figure 7.10: SPAMM – CSPAMM Fourier Spectrum a-b) 3rd Time Frame, c-d) 9th Time Frame, e-f) 12th Time Frame</i>	101

Figure 7.11: Spectral Peak Filtering CSPAMM, Vertical Tags – frame 4: a-b) normal: 10 58 0 256, c-d) Over filtering: 30 40 0 256, e-f) Under filtering: 0 150 0 256.....	102
Figure 7.12: Velocity Fields, 3-4 frames, $U_x - U_y$ components a-b) Normal Filtering, b-c) Over Filtering, e-f) Under Filtering	103
Figure 7.13: Vertical Tags Angle Derivatives before and after median filtering a) X-axis derivative before median filtering, b) X axis Derivative after Median Filtering, c) Y-axis derivative before median filtering, d) Y-axis Derivative after median filtering	104
Figure 7.14: Velocity Fields 3-4 frames a) U_x component, b) U_y component, c) Absolute Value, d) Vectors.....	105
Figure 7.15: Eigenvalues and Eigenvectors of the 7th frame of patient data a) Principal eigenvalue, b) Principal Eigenvector, c) The other eigenvalue, d) Eigenvector perpendicular to Principal direction	106
Figure 7.16: Velocity Fields a) Before Restoration, b) After Restoration	107
Figure 7.17: $U_x - U_y$ velocity components from CSPAMM images a-b) 3-4 time frames, c-d) 5-6 time frames, e-f) 11-12 time frames	108
Figure 7.18: $U_x - U_y$ velocity components from SPAMM images a-b) 3-4 time frames, c-d) 5-6 time frames, e-f) 11-12 time frames	109
Figure 7.19: $U_x - U_y$ velocity components from CSPAMM images – Normal Volunteer data a-b) 1-2 time frames, c-d) 2-3 time frames, e-f) 3-4 time frames.....	110
Figure 7.20: $U_x - U_y$ velocity components from CSPAMM images – HCM patient data a-b) 1-2 time frames, c-d) 2-3 time frames, e-f) 3-4 time frames	111
Figure 7.21: Normal Volunteer Velocity Fields Through out the cardiac cycle, LV a) 1-2 frame, b) 2-3 frame, c) 3-4 frame, d) 4-5 frame, e) 5-6 frame, f) 6-7,frame g) 7-8 frame, h) 8-9 frame, i) 9-10 frame, j) 10-11 frame, k) 11-12 frame, l) 12-13 frame.....	113
Figure 7.22: Patient Data with HCM LV & RV, a) 1-2 frames, b) 2-3 frames, c) 3-4 frames, d) 4-5 frames, e) 5-6 frames, f) 6-7 frames, g) 7-8 frames, h) 8-9 frames, i) 9-10 frames, j) 10-11 frames, k) 11-12 frames.....	115
Figure 7.23: Normal Volunteer, Principal Eigenvalues – left column, Principal Eigenvectors – Right Columns, a-b) 3 rd frame, c-d) 5 th frame, e-f) 11 th frame	116
Figure 7.24: Patient Data, Principal Eigenvalues – left column, Principal Eigenvectors – Right Columns, a-b) 3 rd frame, c-d) 5 th frame, e-f) 11 th frame	117
Figure 0.1: Overview of the HARP MRI application	124
Figure 0.2: a) Info Tab, b) Velocity Tab, c) Scale Tab, d) Zoom Tab	126
Figure 0.3: Different Visualisation Scheme	130
Figure 0.4: Object Orientated Model of Manipulating MRI Image Data	131

Acknowledgements

I would like to thank Miss Masood and also Professor Guang- Zhong Yang for his encouragement and overall supervision. I would also like to express my sincere thanks to Mr. Paramate Horkaew for his kind advices in terms of implementation issues.

The code that implements the FFT transforms used by 'HARP MRI' application is based on the free licence software FFTW. I respectfully acknowledge its authors.

<http://www.fftw.org/>

Abstract

In this study the *HARP MRI* technique is adapted in order to calculate velocity fields and strain maps throughout the cardiac cycle. The implications of *HARP* principles are investigated step by step and detailed analysis is given for various parameters affecting the quality and accuracy of the results. The proposed technique was implemented with *CSPAMM* tagged images and *HARP* for the rapid calculation of deformation and strain tensors. Velocity fields are estimated from both *CSPAMM* and *SPAMM* images in order to validate whether it is possible to assess myocardial motion through out the whole cardiac cycle. It has been demonstrated that *CSPAMM* images are more appropriate in terms of *HARP* filtering and resistant to tag fading. Vector de-noising and restoration were applied to eliminate noise and improve the effectiveness of the current study. Results were compared with both a normal volunteer and a patient in order to validate the potential value of this technique in a clinical environment. Finally, a flexible research tool to visualize and process both anatomical and functional *MR* images has been developed to fulfil these requirements by using *Visual C++ /MFC*.

Introduction

The heart is the most vital organ of the body and regarded as a symbol of life and health. Cardiac muscle works as a perfected electrical pump, beating about once every second during our lifetime. Its physiology and function have fascinated researchers from many disciplines for centuries. Although cardiac function seems to be independent of the human brain, it is dramatically affected by both lifestyle, stress and emotions. Before 1900, very few people died of heart disease. The industrial revolution has made life easier and less strenuous. However, the combination of a sedentary lifestyle, a rich diet and a psychologically stressful rhythm led to an increase in clogged blood vessels, heart attacks and strokes.

Cardiovascular disease is the leading cause of death in industrialized countries. More than two of five Americans die of cardiovascular disease and nearly half of deaths in Britain are caused from heart failure. Its appearance depends on an undetermined combination of genetics and lifestyle. Technically, a heart attack occurs when the supply of blood to the heart muscle is reduced or stopped. Surprisingly, many people who die appear to be fit and healthy. However, while a heart attack is sudden its causes are not.

Diagnosis of the disease in its early stages and treatment can lead towards prevention, thus significantly reducing mortality and alleviating the patients' symptoms. Certain clues about the healthy status of the heart can be deduced from the physiology and motion of cardiac muscle. Cardiac imaging provides physicians with the most valuable information for monitoring cardiac function and derive appropriate diagnosis and treatment. Not only can these factors improve patient's life and decrease mortality but can also limit costs. Furthermore, it is a valuable tool for evaluating the effectiveness of new drugs designed to restore the damage of stunned heart tissue. 3D reconstruction of the cardiac circle climaxes the exploration of heart tissue behaviour and its mechanical characteristics and thus its contribution in exploring and understanding of cardiac function is tremendous.

CT, Nuclear Medicine, Ultrasound and *MRI* are the most common, *non-invasive*, cardiac imaging techniques. Contrary to *CT* and *Nuclear Medicine* that expose the patient to considerable amount of ionising radiation, there is no evidence that *MRI* is hazardous. Furthermore, advantages of *MRI* over *Ultrasound* include the ability to

image arbitrary scan planes and the ability to study flow in any direction. *CMRI* has unique advantages towards the other techniques as it can provide diagnostic information in anatomy, structure, global and regional function and contraction patterns in patients. Therefore, it has the potential of integrating several scanning techniques into a single sequence examination in order to increase diagnostic accuracy, decrease cost and make patients life easier.

HARP MRI is an innovative way that brings *MRI* closer to this objective as it overcomes the limitations of conventional *MRI* techniques that require the post-processing of many hours and hamper the establishment of *CMRI* as a standard clinical tool for in-vivo quantification of myocardial deformation and viability.

The first chapter of this thesis briefly describes the cardiac physiology and function. Its objective is to highlight those factors that lead to an accurate and early diagnosis of heart disease. The second chapter is devoted to different cardiac imaging techniques. It highlights their advantages and limitations, as well as justifies why *MRI* is considered to be the most suitable technique for fully assessing cardiac function and 3D anatomy. The third chapter introduce the mathematical definitions, essential to describe the mechanical properties of the beating heart muscle. It also provides the reader with a brief overview of the current common non-invasive techniques of measuring myocardial deformation and contraction. The fourth chapter is about *MRI* tagging. Methods and refinements are mentioned. *SPAMM*, *CSPAMM*, *DANTE* and their contribution to research of the cardiac motion are analysed. It also constitutes a basic theoretical background for the introduction of *HARP MRI* that is represented in the following chapter. *HARP MRI* is the core of the theoretical background behind this study. It is a detail reference that integrates the on going research under a uniform and consistent scheme. Chapter six, vector restoration, analysis the de-noising method and proposes a computational easy way to apply it. Chapter seven describes the experimental part and the visualization process. Experiment setup and results are described there as well as vector restoration for visualization enhancement. Chapter 8 concludes the report, summarises the work done and suggests future directions of research. Finally, a brief overview of the software development, '*HARP MRI*' application, and its object oriented design is presented in a supplementary appendix.

Chapter 1 – Heart structure and Physiology

1.1 Introduction

The heart is a helically wound muscle structure that is ingeniously designed to push the blood to the lungs and then back to body. Its function reveals both complex mechanical and electrical properties, which make the muscle pump ceaselessly and allow it to adjust its function according to the different demands placed on it. Physicians gather information about anything that can be observed and be related to abnormal behaviour. They are particularly interested in relating the macroscopic muscle structure to its functional behaviour in order to predict when and how things go wrong in disease, the extent of damage and the amount of functional reserve the muscle has. It is essential for cardiac imaging to look at the myocardium in a way that is accessible and clear for the physicians. This chapter will provide the reader with basic information about cardiac physiology and function as well as certain definitions and concepts about how its mechanical deformation can be described mathematically.

1.2 Cardiac Anatomy and Physiology

The heart muscle is well protected, located between the lungs in the middle of the chest, behind and slightly to the left of the breastbone. The heart consists of four *chambers*, four *valves* and various *vessels* bringing blood to and carrying it away from the heart by *veins* and *arteries*, Figure 1.1. The upper chambers are called the *left* and *right atria*, and the lower chambers are called the *left (LV)* and *right (RV) ventricles*. A wall of muscle called the *septum* separates the left and right atria and the left and right ventricles. The atria act as reservoirs for venous blood, with a small pumping action to assist ventricular filling. In contrast, the ventricles are the major pumping chambers for delivering blood to the pulmonary (right ventricle) and systemic (left ventricle) circulations. The left ventricle is the largest and strongest chamber in the heart and does the majority of the work. The left ventricle's chamber walls are only about a half-inch thick, but they have enough force to push blood through the aortic valve and into your body, [Masood02]. Four valves ensure that blood flows only one way, from atria to ventricle (*tricuspid* and *mitral* valves), and then to the arterial circulations (*pulmonary* and *aortic* valves). The myocardium consists of muscle cells,

which can contract spontaneously, and pacemaker and *conducting* cells, which have a specialised function. The function of the Left Ventricle has been exhaustively investigated and its motion has been related to various diseases. The Right Ventricular wall motion is not well understood yet and there are only few studies that have focused on right ventricular function.

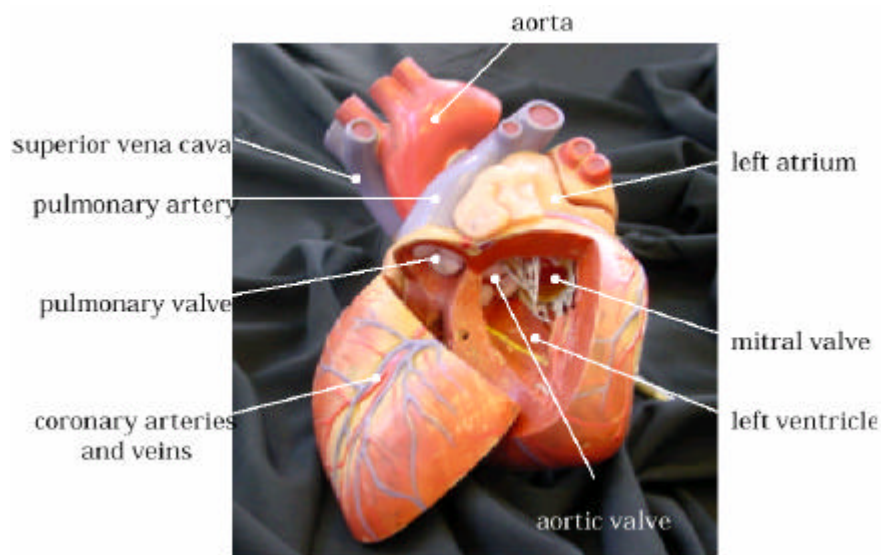


Figure 1.1: Cardiac Anatomy [Masood02]

It worth mentioning that the basic imaging planes physicians look at can be grouped with respect to the heart, such as *horizontal and vertical long axis* and *short axis*, and planes oriented with respect to the major axes of the body, [Manning02]. Planes that are parallel or at 90° angles to the long axis of the body are called *transaxial* and *body-plane orthogonal views*, respectively. In [Pennel02] there is an attempt to record and standardize the different options, based on principles that have evolved from cardiac anatomy and clinical needs.

1.3 Electrophysiology of the heart

Myocardial contraction results from a change in voltage across the cell membrane, *depolarisation*, which leads to an action potential. Although contraction may happen spontaneously, it is normally in response to an electrical impulse. This impulse starts in the *sinoatrial (SA) node*, a collection of *pacemaker cells* located at the junction of the right atrium and superior vena cava, Figure 1.2-b. These specialised cells depolarise spontaneously, and cause a wave of contraction to pass across the atria.

Following atrial contraction, the impulse is delayed at the *atrioventricular (AV) node*, located in the septal wall of the right atrium. From here special fibres allow rapid conduction of the electrical impulse via right and left branches, causing almost simultaneous depolarisation of both ventricles.

As the heart undergoes depolarization and re-polarization, the electrical currents that are generated spread not only within the heart, but also throughout the body. This electrical activity generated by the heart is generally measured by an array of electrodes placed on the body surface and the resulting tracing is called an *electrocardiogram (ECG, or EKG)*, Figure 1.2-c. The different waves that comprise the ECG represent the sequence of depolarization and re-polarization of the atria and ventricles. A *P-Wave* represents atrial systole, while a *QRS complex* represents ventricular systole and *T-Wave* ventricular diastole.

ECG is important not only because indicates abnormalities in cardiac function but also because it can be used in cardiac gating, a method employed to reduce motion artifacts produced as a result of heart motion and pulsatile blood flow. This method is common in cardiac imaging, especially in *MRI*, and it will be fully explained later. Although the ECG shows heart rate and rhythm and can indicate myocardial damage, it gives no information on the adequacy of contraction.

1.4 Cardiac Cycle

Figure 1.2-a , from [Masood02] indicates the relationship between electrical and mechanical events in the cardiac cycle. Briefly, *systole* refers to contraction, while *diastole* refers to relaxation. Both contraction and relaxation can be isometric, when changes in intra-ventricular pressure occur without a change in length of the muscle fibres. The cycle starts with depolarisation at the sinoatrial node leading to atrial contraction. Until this time blood flow into the ventricles has been passive, but the atrial contraction increases filling by 20-30%. Ventricular systole causes closure of the atrio-ventricular valves and contraction is isometric until intra-ventricular pressures are sufficient to open the pulmonary and aortic valves, when the ejection phase begins. The volume of blood ejected is known as the *stroke volume*. At the end of this phase ventricular relaxation occurs, and the pulmonary and aortic valves close. After isometric relaxation ventricular pressures fall to less than atrial pressures. This

leads to opening of the atrio-ventricular valves and the start of ventricular diastolic filling. The whole cycle then repeats following another impulse from the sinoatrial node.

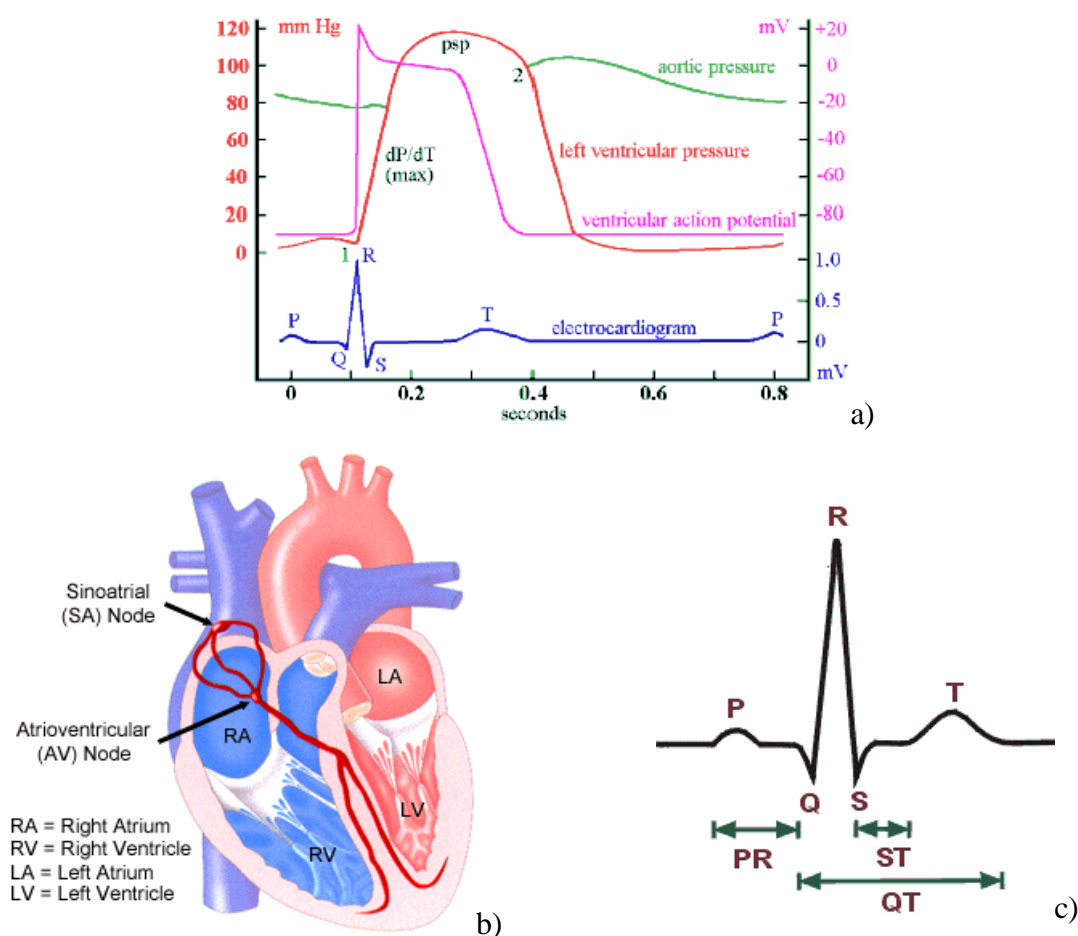


Figure 1.2: a) Cardiac Electrophysiology, [Masood02], b) The conduction system, [<http://www.tmc.edu/thi/conduct.html>], c) Electrocardiogram

1.5 Cardiac Gating

Most cardiac imaging techniques have to compensate for the cardiac motion in order to obtain good quality images. *Gating techniques* are useful whenever data acquisition is too slow to occur during a short fraction of the cardiac cycle. Image blurring due to cardiac-induced motion occurs for imaging times of above approximately 50 ms in systole, while for imaging during diastole the critical time is of the order of 200–300ms. The principle of cardiac gating is that data from each slice is always acquired when the heart is at the same phase of cardiac activity in order to reduce the phase mismatching produced as a result of heart motion. It uses the R wave Figure 1.2-c to trigger the scanning process and thus the effective scanning time during one cardiac

cycle depends totally on the time interval between each R wave. This is called the *R to R interval* and is controlled by the patient's heart rate.

There are three approaches to gating heart studies: *Prospective gating*, *retrospective gating*, also known as *retrograde triggering*, and *self-gating*. Prospective gating uses an ECG signal to initiate data acquisition at a present time after the peak of the R-wave and it allows sequential scanning to be performed at a single, predetermined phase of the cardiac cycle. Prospective gating schemes are affected by the device not knowing what the heart rate will be. Indeed, the length of the interval that follows a particular R-wave is not known until the cycle has been completed and thus irregular heart beats cannot be rejected. Prospective gating presupposes exact reproducibility of the heart motion in successive cycles, a condition which is violated in practise, especially in cases of cardiac arrhythmia.

On the other hand, retrospective gating, [Roerdink93], combines data acquisition in parallel with ECG recording and this allow image data to be reconstructed at different phases of the cardiac cycle. It is less sensitive to arrhythmia since it is possible to achieve a true match of the image data to the ECG trace retrospectively.

Finally, self-gating is also retrospective, but does not use an ECG signal. In self-gating, slices are selected as per the size of the heart, that is, in terms of its extension. This selection can be done globally or for portions of the heart separately. The idea is that instead of using the timing of the ECG signal, the system decides when is the desired end itself.

1.6 Myocardial Perfusion

Myocardial perfusion measures the blood flow per unit of myocardial tissue and characterizes the delivery of blood to heart tissue. The beating heart works ceaselessly and thus it has high demands in oxygen and nutrients. Indeed, the myocardium is dependent primarily on aerobic metabolism for energy supply, meaning that this tissue is heavily dependant upon oxygen delivery for maintenance of a minimal level of normal function. The major determinants of oxygen demand are ventricular wall stress, heart rate and myocardial contractility. The blood supply to the myocardium is via large epicardial coronary arteries, Figure 1.1, [Massood02]. The myocardium is perfused by coronary vessels that exit from the aorta in right and left trunks to divide

into progressively smaller branches that cover the surface of the heart. These smaller branches penetrate the myocardium to supply it with blood flowing from the outside, *epicardium*, to the inside, *endocardium*. Thus, the endocardium has the lowest perfusion pressure and is the most susceptible to compromised coronary blood flow. The occlusion of these arteries is related with various cardiovascular diseases, which lead to significant dysfunction of myocardial tissue. Therefore, methods for displaying the distribution of blood to myocardial tissue play an important role to prediction of viability of the myocardium and treatment of diseases such as ischemia and coronary artery disease. The most common imaging modalities widely used for evaluating perfusion is *Nuclear Medicine (SPECT, PET)* and *MRI*. Both will be analysed at the second chapter.

1.7 Common Cardiovascular Diseases

1.7.1 Coronary Artery Disease

Significant contraction problems occur when the blood supply to the heart is impaired by *Coronary Artery Disease (CAD)*. CAD is the end result of atherosclerosis, which is a complex disease process involving the narrowing or complete blockage of coronary arteries due to atheroma caused by the deposition of atheromatous plaques containing cholesterol and lipids. This plaque formation begins with the deposition of lipids with activated macrophages in the intima of arteries, aided by injury to the endothelial cell barrier. The plaque grows with the addition of increasing amounts of cholesterol with resulting narrowing of the arterial lumen and compromise of blood flow. The factors that determine whether and how fast the plaque grows are not completely understood. However, the levels of low density *lipoproteins (LDL)*, specifically oxidized LDL, in the blood correlate with the severity of atherosclerosis. The plaque can grow to completely occlude the lumen of the coronary artery, causing myocardial ischemia and/or infarction.

1.7.2 Myocardial Ischemia

Ischemic heart disease (IHD) is the single leading cause of death in industrialized countries. It refers to a condition in which there is acute, intermittent, or permanent compromise in oxygen supplied to the myocardium. IHD is most commonly due to a

chronic and/or acute reduction in blood flow in the arteries that supply the myocardium with blood, and thus it is closely related to coronary artery disease. Low-flow ischemia is further characterized by inadequate removal of metabolites, which leads to diminished contractility. Indeed, ischemic myocardium does not contract well, leading to decreased contractility and very often a decrease in cardiac output (rate blood flow resulting from heart pumping action). The decrease in myocardial contractile activity is often segmental, relating to the particular coronary blood vessel or vessels that were occluded, leading to *infarction* of the portion of the myocardium supplied by that vessel. In addition, ischemic myocardium is less compliant, 'stiff', making it less able to relax in response to blood entering its chambers from the venous circulation, increasing chamber pressure. This increased intra-chamber pressure has adverse consequences on myocardial and pulmonary function. Finally, the endocardium is more likely to suffer these ischemic functional effects than the epicardium for the reasons stated above. Patients with myocardial ischemia without myocardial infarction might be without obvious symptoms. Imaging techniques allow us the opportunity to diagnose its presence and to institute measures to prevent the potentially fatal consequences of infarction.

1.7.3 Infarction

Myocardial infarction (MI) is a subset of myocardial ischemia in which there is permanent damage to the myocardium. In other words, it is an area of dead tissue, *necrosis*, resulted from a localised deprivation of oxygen. Myocardial infarction occurs initially within the subendocardium, the outer layer of endocardium. The consequence of myocardial infarction is the altered biomechanical function of the heart. The time between the onset of ischemia and muscle cell death is about 15 to 20 minutes in most cases. Almost always the infarction occurs in the left ventricle and left ventricular function may be significantly diminished. The larger the affected area of the myocardium is the greater the loss of contractility. All myocardial infarctions have a central area of necrosis that is surrounded by an area of injury. Myocardial tissue does not regenerate after injury so the necrotic tissue is replaced by scar tissue that may inhibit contractility. If a large area of tissue is involved the heart as a pump may be compromised and the symptoms of congestive heart failure will be seen.

1.7.4 Myocardial Remodeling

Functional changes in the heart due to heart disease can lead to structural remodelling of the ventricle. Indeed, LV enlargement must occur in order to maintain or restore forward output in the presence of an infarct exceeding a certain size. *Myocardial Remodeling* refers to the changes in shape and size of the myocardium that can follow a myocardial infarction (MI). The process of LV enlargement can be influenced by three independent factors that is, infarct size, infarct healing and LV wall stress. The process is a continuum, beginning in the acute period and continuing through and beyond the late convalescent period. During the early period after transmural MI the infarcted region is particularly vulnerable to distorting forces; once healed, the scar itself is relatively non distensible and much more resistant to further deformation. Therefore late enlargement is due to complex alterations in LV architecture involving both infarcted and non infarcted zones. This late chamber enlargement is associated with lengthening of the contractile regions rather than progressive infarct expansion. These observations indicate that a combination of a pressure-type hypertrophy resulting in increased tissue diameter, with a volume-type hypertrophy, resulting in tissue elongation, is resulted from MI. In fact, an enlarged ventricle can eject a larger stroke volume, despite unchanged tissue shortening.

The disadvantage of dilatation is the extra workload imposed on normal, residual myocardium and the increase in wall tension, which represent the stimulus for hypertrophy. *Hypertrophic Cardiomyopathy (HCM)* is a heart disease where areas of muscle enlarge and thicken. HCM causes significant ventricular wall hypertrophy while ventricular chamber size may be reduced making it unable to fill with adequate amount of blood. If hypertrophy is not adequate to match increased tension, then a vicious cycle will start which determines further and progressive dilatation, [Brower01]. Whether this process is reversible is unknown. Ventricular remodelling is a significant factor in the process resulting in heart dysfunction and eventually failure.

1.7.5 Heart Failure

Heart Failure (CHF) is defined as a condition in which, in the presence of adequate venous return, a cardiac abnormality makes this organ unable to pump blood at a rate

that satisfies the metabolic needs of tissues. While *forward heart failure* refers to decreased tissue perfusion caused by reduced cardiac output leading to tissue dysfunction, *backward heart failure* refers to tissue congestion caused by abnormally elevated venous pressures. When heart function declines, the body recruits many mechanisms in an attempt to maintain adequate cardiac output and thereby adequate tissue perfusion. These mechanisms are important to recognize because recognizing their presence can help detect early heart failure in patients who are doing and feeling well. Such patients with heart failure but whose compensatory mechanisms have allowed them to maintain reasonable, but somewhat less normal, heart function are said to have *compensated heart failure*.

1.8 References and Bibliography

- [Manning02] Warren J. Manning and Dudley J. Pennell, 'Cardiovascular Magnetic Resonance', chapter 8: 'Normal Cardiac Anatomy, Orientation and Function', New York; Edinburgh : Churchill Livingstone, c2002
- [Masood02] Sharmeen Masood, 'Macroscopic Structure and Physiology of the Normal and Disease Heart', PhD thesis, supervised by G-Z Yang
- [Pennel02] Manuel D.Cerqueira, Neil J. Weissman, Vasken Dilsizian, Alice Jacobs, Sanjiv Kaul, Warren K. Laskey, Dudley J. Pennel, John A. Rumberger, Thomas Ryan, Mario S. Verani, 'Standardized Myocardial Segmentation and Nomenclature for Tomographic Imaging of the heart', *Circulation* 2002; 105:539-542
- [Roerdink93] J.B.T.M. Roerdink and M. Zwaan, 'Cardiac magnetic resonance imaging by retrospective gating: mathematical modelling and reconstruction algorithms', *Euro. Journal of Applied Mathematics* 4, 1993, pp. 241-270
- [Brower01] Gregory L. Brower and Joseph S. Janicki, 'Contribution of ventricular remodeling to pathogenesis of heart failure in rats ', *American Journal of Physiology Heart and Circulatory Physiology* 2001 Feb; 280(2): H674-H683

Chapter 2 – Cardiac Imaging

2.1 Introduction

There are plenty of different medical imaging techniques that not only provide for diagnosis but also serve to assist planning and monitoring the treatment of malignant diseases. All imaging methods rest on the physics of the interaction of energy and biological tissue. It is necessary for the energy to penetrate the body and be partially absorbed or scattered. However, different imaging techniques are based on separate physical interactions and thus provide measurements of different physical properties of biological structures. The different approaches do not emulate but complement each other in the solution of different problems. What may be a quite impossible task for one method may be solvable by another. It is important for both clinicians and patients to request the appropriate images in order to reach a clear diagnosis by the quickest, most accurate, least inconvenient, least harmful and least painful way.

In terms of Cardiac Imaging there are additional considerations that trouble scientists. Assessment of myocardium function requires both anatomical and functional information. Respiratory and cardiac motion causes non-negligible artifacts that should be compensated. Finally, spatial and temporal resolution, image contrast, signal to noise ratio (SNR) and cost are significant factors that should be balanced. There are four cardiac imaging techniques worth mentioning: *Computed Tomography (CT)*, *Nuclear Medicine*, *Ultrasound* and *Magnetic Resonance Imaging (MRI)*. This chapter investigates their basic principles and highlights their contribution in cardiac imaging.

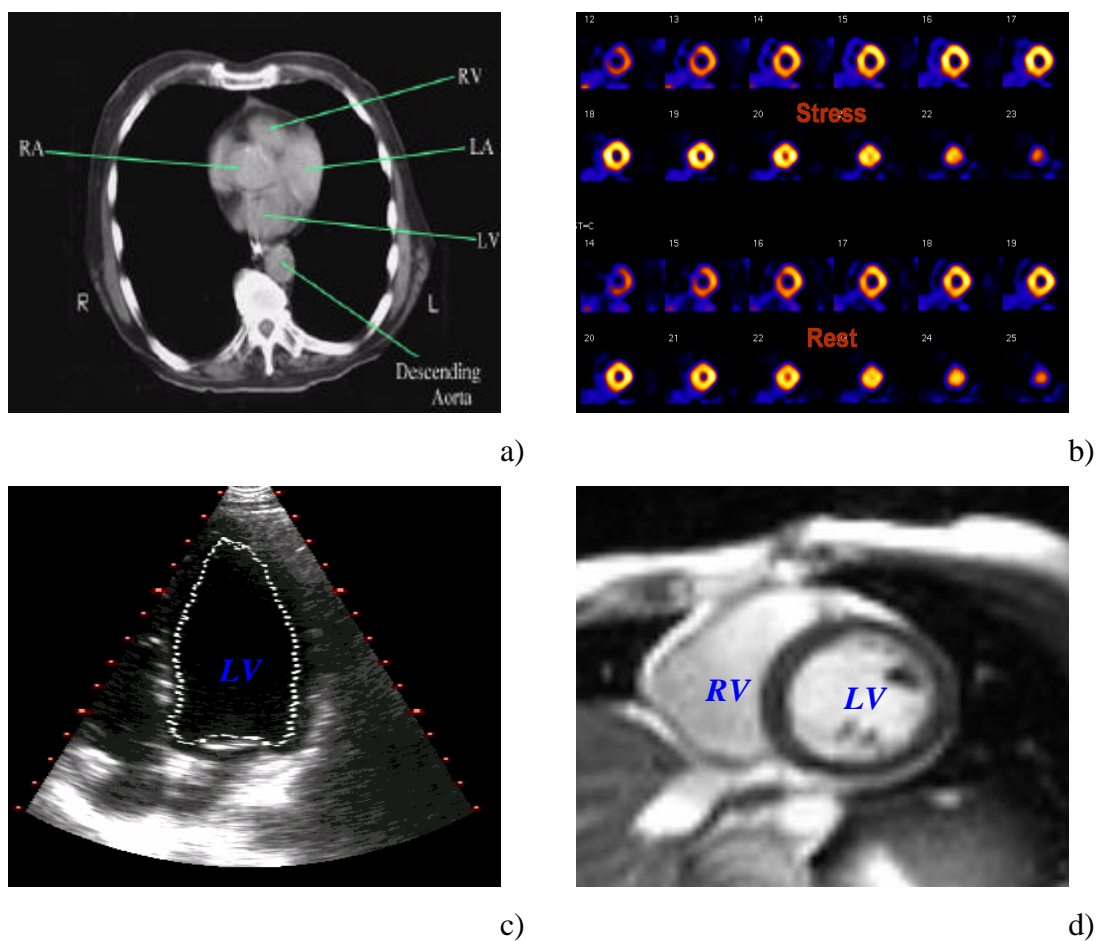


Figure 2.1: Cardiovascular Imaging: a) Computed Tomography, b) Nuclear Medicine, c) Ultrasound, d) Magnetic Resonance

2.2 Computed Tomography (CT) – Principles

2.2.1 Conventional X-Ray Images

Computed Tomography (CT) imaging Figure 2.1-a, also known as *Computerized Axial Tomography (CAT)*, is based on radiology with *X-Rays*. Conventional xray imaging has evolved over the past 100 years, but the basic principal is still the same as in 1895. All X-Ray imaging is based on the absorption of x rays as they pass through the different parts of a patient's body. It is the special energy and wavelength of the x-rays, which allow them to pass through the body part and create the image of the internal structures. Depending on the amount absorbed in a particular tissue a different amount of x-rays will pass through and exit the body. The radiographic image is formed by the interaction of x-ray photons with a photon detector and is therefore a distribution of those photons, which are transmitted through the patient and are recorded by the detector. These photons can pass through the patient either with or

without interacting. The latest carry the most useful information as they indicate the probability that a photon will pass through the patient without interacting. This probability depends on the sum of the x-ray *attenuating* (weakened) properties of all the tissues the photon traverses. Therefore, the image is a projection of the attenuating properties of all the tissues along the paths of the x-rays. The final image is a two-dimensional projection of the three-dimensional distribution of the x-ray attenuating properties of tissue, [Webb92].

If the transmission of photons is very low, then very few photons will reach the image receptor and the *radiation dose* to the tissue will be very high. If the transmission is close to unity then there will be very little difference in transmission through different types of tissue and the contrast in the image will be poor. Thus, the choice of energy should be a compromise between the requirements of low dose and high contrast. It is the differences in absorption and the corresponding varying exposure level of the film that creates the images, which can show broken bones, clogged blood vessels, cancerous tissues and other abnormalities.

However, one of the major limitations of conventional planar radiography is its inability to produce sectional information. The image produced represents the total attenuation of the x-ray beam as it passes through the patient. Thus, it is impossible to distinguish any depth information on the acquired image. Furthermore, the blood in the blood vessels and details of the heart anatomy cannot be seen on a conventional radiograph because of its inability to distinguish soft tissue.

2.2.2 From X-rays imaging to Computed Tomography (CT)

The development of computed tomography (CT) in the early 1970's revolutionized medical radiology. CT is a digital imaging process, which produces cross-sectional images (slices) of anatomy. The x-ray beam interrogates only part of the body that is inside the slice. This eliminates the problem of depth information as x-rays are passed through the body only in directions that are contained within and are parallel to the plane of the slice.

CT systems consist of two main parts: a physical measuring technique, which integrates the local density along certain paths and a mathematical reconstruction algorithm, which calculates the local concentrations from the obtained raw data,

called *projection data*. Therefore, a fundamental task of CT systems is to make an extremely large number of highly accurate measurements of x-ray transmission through the patient in a precisely controlled geometry. A basic system generally consists of a *gantry*, a *patient table*, a *control console*, and a *computer*. The gantry contains the *x-ray source*, *x-ray detectors*, and the *data acquisition system (DAS)*.

CT technology has been evolved through five scanners generations. The objective is to sufficiently reduce the acquisition time in order to acquire volume information of the beating heart. The fifth generation of CT scanners are unique in that the x-ray source is an integral part of the system design. The detector array remains stationary, while a high-energy electron beam is electronically swept along a semicircular tungsten strip anode. X-rays are produced at the point where the electron beam hits the anode, resulting in a source of x-rays that rotates about the patient with no moving parts. Projection data can be acquired in approximately 50 ms, which is fast enough to image the beating heart without significant motion artefact. An alternative fifth generation design, called the dynamic spatial reconstructor (DSR) scanner, is in use at the Mayo Clinic. This machine is a research prototype and is not available commercially. Volume CT images can be produced in as little as 10 ms.

The requirement for faster times, and in particular for fast multiple scans for three-dimensional images, has resulted in the development of spiral (helical) scanning systems. Multiple images are acquired while the patient is translated through the geometry in a smooth continuous motion rather than stopping for each image. Projection data for multiple images covering a volume of the patient can be acquired in a single breath hold at rates of approximately one slice per second. The reconstruction algorithms are more sophisticated because they must accommodate the spiral or helical path traced by the x-ray sources around the patient.

Another development in the technology is *electron beam CT*, also known as *EBCT*. Although the principle of creating cross-sectional images is the same as for conventional CT, whether single- or multi-slice, the EBCT scanner does not require any moving parts to generate the individual snapshots. As a result, the EBCT scanner allows a quicker image acquisition than conventional CT scanners. EBCT has sufficient temporal resolution to image the heart within a defined phase during the heart cycle.

2.2.3 Cardiac CT Imaging

Currently the various scanning techniques, used to image the heart can be summarized as follows, [Regn02], [Ohnersorge00]:

1. Single slice sequential (transaxial) imaging with stop and go off the patient table and with the acquisition of single discrete slices at each level. This type of single slice operation is typically used with EBCT scanners in combination with prospective ECG triggering. The temporal resolution is 100ms and is still unique to EBCT. The limitations of the single slice sequential technique is to achieve the desired volume coverage within a single breath hold. Even if a single breath hold wide beam collimations of 3mm (slice thickness) is applied the typical examination time will be 30-40s. Clearly, a high resolution technique, like 1mm/0.5mm (slice width/image increment) is impractical due to scan times up to 120s and due to dose considerations. Furthermore, since single slices are acquired with the table travel in between there is the danger of misregistration due to heart motion in between successive acquisitions. Finally, the prospective triggering is sensitive to irregular heart rates and arrhythmias.
2. Multislice sequential (transaxial) imaging with the simultaneous acquisition of multiple slices at each table position. Typical techniques are based on a 4 by 2.5 mm collimation and a 0.5s full rotation time. Four slices are acquired simultaneously with a temporal resolution of 250ms using a half-scan acquisition and reconstruction technique. Therefore, the probability of misregistration between neighbouring sections is reduced. However, beam collimations of 4 by 2.5 (slice width 2.5 mm) are used to achieve fast volume coverage and the sensitivity to irregular heart beats still remains.
3. Single slice spiral imaging with continuous table translation. Although spiral scanning is basically capable of performing it no continuous sampling can be achieved because of heart motion.
4. Multislice spiral imaging with four straight lines representing the continuous acquisition of four data sets, simultaneously. The volume coverage is now sufficient to cover the relevant cardiac anatomy with high resolution techniques, such as 4 by 1 mm beam collimations. Therefore, spiral scanning with

retrospective gating can be applied for high quality images of *CT angiography (CTA)* and *Calcium scoring (Ca-scoring)*, which can detect small amount of calcium plaque in coronary arteries. It has been found that the temporal resolution is sufficient to provide virtually motion free imaging of calcified plagues even for patients with higher heart rates up to 120 bpm.

2.2.4 Safety considerations – Limitations of Computed Tomography

The basic inevitable limitation of CT is the exposure of patients to harmful radiation. A quantitative feel for the situation can be gained from that the average risk of inducing a fatal malignancy in a human tissue subjected to a dose of 10mSv may lie in the region of 10^{-4} and the overall risk in the development embryo or early foetus lies in the range 0-1 per 1000, [Webb88]. CT produces a very larger patient dose than single x-ray radiography because it combines information from several radiographs. A single CT scan produces a dose exceeding 4 years of natural background radiation, [Guy00], and thus CT can be used neither for mass population screening nor as a real time 3D visual aid to surgery.

2.3 Nuclear Medicine – Principles

2.3.1 Nuclear Medicine

Contrary to X-ray and CT imaging, *Nuclear Medicine*, Figure 2.1-b also called *radionuclide scanning*, does not image the anatomy of the body but it monitors the distribution of radioactive elements that has been inhaled or injected, for this purpose, inside the body. The distribution of these agents, also called *radiopharmaceuticals*, is determined by factors such as blood flow, blood volume and a variety of metabolic processes. Thus, temporal changes in the spatial distribution of radiopharmaceuticals can be obtained by multiple images and show basic function of the organ or system being examined. This form of imaging is also known as *dynamic scintigraphy*.

Similarly, to X-ray imaging planar images based on radionuclide scanning contain information from a three-dimensional object and thus, it is often difficult to determine

the function of tissue deep in the body. Tomographic studies obtained by taking multi-view acquisition overcome most problems caused by the projection of 3D information on a single planar view. This technique is called *Emission Computed Tomography (ECT)* and although it has some features in common with X-Ray CT there are some important differences. X-Ray CT is based on the determination of photon attenuation in body tissue, while in ECT there is a basic need to correct for the effect of photon attenuation whilst determining the distribution of radioactivity within the body. This problem deteriorates the quality of image in terms of signal to noise ratio, especially, when the radioactive agent has low concentration. Furthermore, in X-rays the position of both source and detector are known while in ECT the location and the strength of the source of radiation are determined by using a lead *collimator*. The collimator selects the direction of the photons incident on the camera. Moreover, it defines the geometrical field of view of the camera and essentially determines both the spatial resolution and sensitivity of the system.

The technique of ECT can be classified into two separate modalities. *Single-photon emission computed tomography (SPECT)* and *Positron emission tomography (PET)*. SPECT involves the use of radioisotopes where a single γ -ray is emitted per nuclear disintegration, while PET makes use of radioisotopes where two γ -rays are emitted simultaneously when a positron from a nuclear disintegration annihilates in tissue, [Webb88]. The two γ -rays have to leave the annihilation site, travelling in nearly opposite directions in order to conserve linear momentum. Therefore, the two γ -rays together define a line that passes close to the point of emission of the original positron, [Guy00]. In SPECT the collimator, which is inherently inefficient, determines the line of sight through the patient for any given projection, while in PET a collimator is not required. Therefore, the key difference between SPECT and PET arises from how the two schemes define a line of sight. In SPECT, this becomes increasingly less well defined with depth, resulting in a reduced spatial resolution in comparison to PET.

2.3.2 Nuclear Medicine in Cardiac Imaging

SPECT and PET are used widely in cardiac imaging in order to detect coronary artery disease and evaluate the extent and severity of coronary stenosis, assess myocardial viability, and outcome and efficacy of therapy. Nuclear Medicine is established on the

principal of imaging the distribution of the radioisotope agent. Therefore, using SPECT or PET, perfusion can be easily estimated. Thallium stress cardiac imaging (SPECT) can distinguish between high and low risk groups after uncomplicated acute myocardial infarction. SPECT was found to provide incremental prognostic information towards the identification of cardiac death. The number of diseased vessels was found to be the single most important determinant of myocardial viability. PET is currently the standard most accepted for the definitive determination of myocardial viability. Finally, PET permits the *in vivo*, non-invasive quantitative measurement of myocardial blood flow.

2.3.3 Safety considerations – Limitations of Nuclear Medicine

Similarly to CT and X-ray scanning, Nuclear Medicine is based on the principles of radiology and thus, inherently, it reflects the same hazards. Indeed, the amount of radiation from a nuclear medicine procedure is comparable to that received during a diagnostic X-ray CT. Moreover, the design of radiopharmaceuticals substances is a challenge as it should fulfil several, often conflicting constraints. While the half life of the isotope must match the cycle time of the metabolic process under consideration, great care has to be taken in order for it not to be toxic and be fully removed by the natural clearance processes in a short time after the investigation has taken place. Furthermore, the agent should have the ability to target a specific organ or disease and it should ideally only emit γ - rays since any accompanying emission would make a large contribution to the patient dose by the complete absorption within the patient body but none to the external image. However, the isotopes used in PET studies, where the emission of a positron is a crucial initial part of the method, cannot meet this ideal.

Relatively poor spatial resolution and signal to noise ratio are inherent problems for all nuclear medicine imaging methods in comparison to x-ray or MR. Indeed, limited count rates in radioisotope studies show up as a degradation of image quality. However, as ECT is not an anatomical imaging technique by nature, it is not sensible to compare image quality directly with those obtained from anatomical modalities such as CT, ultrasound and magnetic resonance. The effectiveness of Nuclear Medicine does not lie in very high resolution but rather in its ability to monitor and

image metabolic processes with very high sensitivity. Therefore, its contribution in measuring myocardium perfusion is significant. However, with myocardial ischemia the subendocardial layer, the upper layer of endocardium, is accordingly most susceptible to necrosis. This potential advantage of myocardial perfusion can only be sufficiently appreciated if the imaging modality provides spatial resolution on the order of 2mm or better, [Manning02]. The spatial resolution of PET and SPECT is not sufficient to detect blood flow deficits limited to the subendocardial layer, while CMR offers the possibility of quantitatively assessing both perfusion and function with high accuracy.

2.4 Ultrasound Imaging – Principles

2.4.1 Basic Principles

Ultrasound, Figure 2.1-c is a diagnostic procedure that uses high frequency sound waves to observe the heart beating and imaging the tissue structure. Ultrasound refers to sound waves with higher frequencies than human beings can perceive (20 KHz). Medical ultrasound applications use frequencies between 500 KHz and 30 MHz. Unlike X-rays, but by analogy with light, ultrasound suffers refraction and reflection at interfaces between media of different acoustic refractive indices, to an extent that makes it possible to build focusing systems. Moreover, ultrasonic waves propagate sufficiently slowly that, for the distances travelled in the body transit times are easily measurable. On the other hand the propagation speed is fast enough that all of the data needed for a complete image may be gathered and reconstructed within 10-20msec, which results in vivo visualizing of the beating heart. Coupled with the very low risk of hazard and the low cost of equipment, ultrasound is one of the most frequently used in diagnostic cardiac imaging.

The optimal ultrasound frequency represents a trade-off between the need to acquire ultrasound images with a high degree of spatial resolution, dictating use of higher frequencies, and the need to obtain adequate "penetration" in the tissue. Imaging depth into tissue is limited by attenuation of the ultrasound waves, and this becomes more severe as the ultrasound frequency is increased.

In medical ultrasound an ultrasound transducer is placed against the patient skin surface, directly over the region to be imaged. The transducer sends a very brief pulse

of ultrasound into the tissue. The pulse travels along a *beam*. Interfaces (*i.e.* moving red blood cells) along the way reflect some of the ultrasound energy back to the transducer. The originally transmitted signal undergoes a detectable change in frequency caused by the moving blood cells, *Doppler Effect*. Similarly, the Doppler effect occurs if the interface is stationary (*i.e.* tissue) and the transducer is moving or reversely when the interface is moving and the transducer is stationary. Therefore, it can be applied to tissue as well as blood cells, *Tissue Doppler*. The transducer, in turn, converts the reflected energy into echo signals, which are sent into amplifiers and signal processing circuits inside the imaging machine's hardware. The exact, microsecond delay between when the transducer first launched the ultrasound pulse and when it picked up an echo tells the machine how far the reflecting interface is from the transducer. Ultrasound images are formed very rapidly, essentially, in real-time with low-cost equipment. Summarizing, ultrasound provides two types of information: tissue position and velocity from the Doppler signal. Unfortunately, Doppler effect is angle dependent, which means that only the component of velocity in the direction of beam can be measured.

2.4.2 The Ultrasound Coordinate System – Transformation

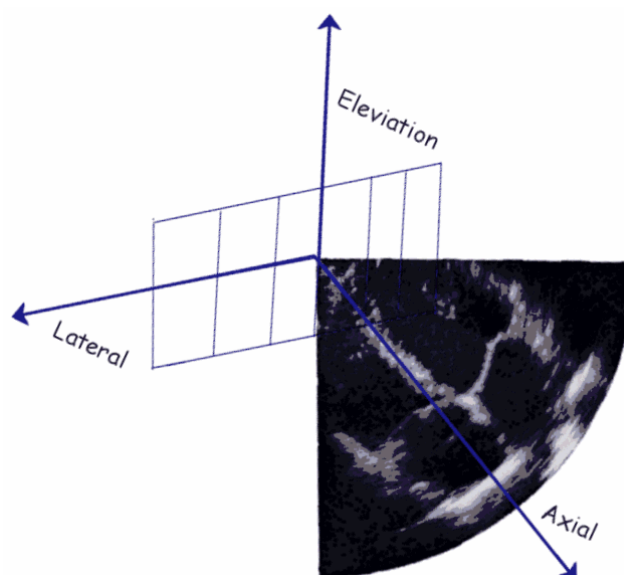


Figure 2.2: Ultrasound Coordinate system

According to [D'hooge00], an ultrasound coordinate system, Figure 2.2, can be defined, with its centre at the position of the transducer and the following three axes:

- *The Axial (A) axis:* It is along the direction of propagation of the ultrasound beam, pointing away from the transducer.
- *The lateral (L_a) axis:* It is within the image plane, perpendicular to the axial direction and pointing towards the left of the image.
- *The elevation (E) axis:* It is perpendicular to both the axial and the lateral direction, defined in such a way that the A - L_a - E coordinate system is right-handed. Thus, the elevation axis is defined perpendicular to the image plane.

When different coordinate systems exist, it is important to be able to transform measurements within one system to measurements using another system. This gives us the flexibility to integrate information and compare the validity of different techniques. There are no closed-form mathematical expressions to describe the transformation between the ultrasonic coordinate system and other coordinate systems since the mathematical formulation depends on the echocardiographic view used and on the myocardial wall studied. However, coordinate transformation can be straightforward when a component in one coordinate system corresponds directly to a component to one component from the other coordinate system. This is when the ultrasonic beam is either parallel or perpendicular to the myocardial wall. Therefore, when the ultrasound beam is parallel to the interventricular septum, the axial strain component corresponds to the longitudinal component. Similarly, when the ultrasound beam is perpendicular to the posterior wall, the axial component in one coordinate system corresponds to the radial component in the other.

Currently, only the axial component of the myocardial function can be measured using ultrasound techniques. Thus, when attempting to measure local strain, no oblique cross-sections of the ventricle should be acquired. In other words, the ultrasound beam should be either perpendicular to the myocardial wall or parallel to the septum. However, due to heart motion during the cardiac cycle, this is often not possible.

2.4.3 Doppler Effect

The *Doppler Effect* is the shift in frequency and wavelength of waves which results from a source moving with respect to the medium, a receiver moving with respect to the medium, or even a moving medium. In other words, when a source of a signal or an object that reflects a signal moves with respect to an observer, the observer receives the emitted signal with different frequency from its actual frequency. The perceived frequency f' is related to the actual frequency f_0 and the relative speeds of the source v_s , observer v_o , and the speed v of waves in the medium by:

$$f' = f_0 \left(\frac{v \pm v_o}{v \pm v_s} \right) \quad \text{Eq. 2.1}$$

The choice of using the plus (+) or minus (-) sign is made according to the convention that if the source and observer are moving towards each other the perceived frequency f' is higher than the actual frequency f_0 . Likewise, if the source and observer are moving away from each other the perceived frequency f' is lower than the actual frequency f_0 .

The Doppler Effect holds true for every type of wave, including light, electromagnetic waves and sound waves.

2.4.4 Limitation of the Ultrasound techniques

There are certain limitations that reduce the efficiency of the ultrasound techniques.

- *Angle dependency of Strain Measurements:* A basic limitation of all ultrasonic methods is that only the axial component can be computed, [D'hooge00] and [Santos01]. Since only the axial strain component can be measured with the current cardiac ultrasound strain estimation techniques, and the heart can be visualized in a limited number of views, the strain components cannot be measured for all myocardial segments. This phenomenon results from the fact that the Doppler probe measures not velocity but the component of velocity in the direction of the beam.
- *Transformations:* Transformation between the ultrasonic coordinate system and another coordinate system can be done only by making sure that the ultrasonic

beam is either perpendicular or parallel to the myocardial wall. This is a way to overcome partially the first limitation as well.

- *Image quality*: Ultrasonic techniques illustrated in [D'hooge00] are very sensitive to noise because both require the calculation of a temporal or spatial gradient or an integral. Thus, the spatial resolution of this technique becomes relatively poor after attempts to remove the noise and smooth the acquired strain rate data. The spatial resolution can be either 1-3mm or 2-5mm with respect to the method that is used. This means that two independent measurements cannot be made accurately for points closer than these values apart. A spatial resolution of 2-5mm may be prohibitive for studying local intramural gradients in strain rate or strain.

2.5 Magnetic Resonance Imaging

2.5.1 Basic Principles

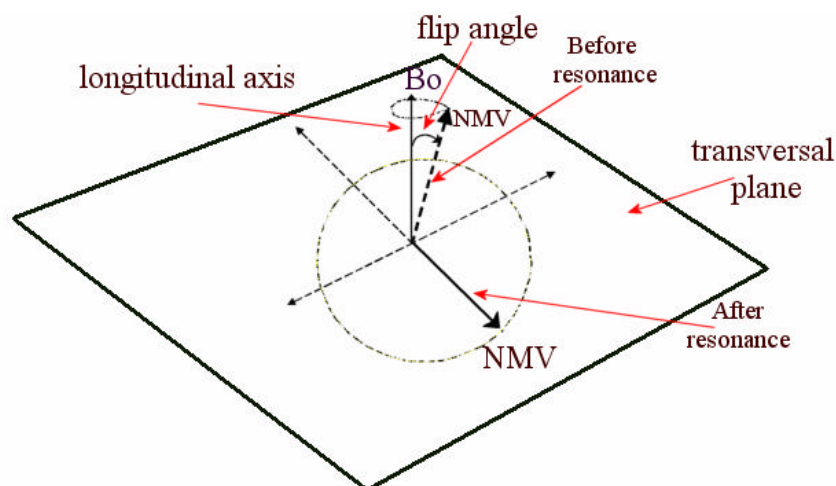


Figure 2.3: Resonance of hydrogen nucleus in a magnetic field B_0

Magnetic Resonance Imaging (MRI) is an imaging technique, Figure 2.1-d, discovered in 1946 by Bloch and Purcell. MRI is a relatively new imaging modality, at the peak of its evolution. It is used primarily in medical settings to produce high quality images of the inside of the human body. *Cardiovascular MR (CMR)* is developed rapidly the last fifty years and established as the only imaging modality that has the potential of combining anatomical, functional and perfusion information in a single scanning session. Similarly to ultrasound does not expose patients to

ionising radiation, while real time 3D visualisation of the beating heart from any point of view is an objective of the on going research.

The principles of MRI rely on the spinning motion of specific nuclei present in biological tissue. Atoms with odd number of protons and/or neutrons possess this nuclear property, known as *spin angular momentum*, often referred to as *spin*. These can be described as charged spheres spinning around an axis, Figure 2.3. Because these spins have charge, they act as tiny magnetic dipoles. These are called *MR active nuclei*. The hydrogen nucleus is the MR active nucleus used in clinical MRI. Most of the human body consists of fat and water that results in a ratio of 63% hydrogen atoms in the human body. Therefore, this technique is able to give both physical and biochemical information about the different types of tissues in the human body.

Under normal conditions the spin axis of MR active nuclei are pointing in random directions such that the net magnetic moment M , the sum of all spins is zero. In the presence of an external magnetic field, however, these spins exhibit three interesting properties:

Alignment:

Spins tend to align either parallel or anti-parallel to the applied field, with a slightly greater number in the parallel position, thus resulting in a net magnetisation or magnetic moment (*Net Magnetization Vector – NMV*). This process is also known as *polarization* or *alignment*. The ratio of parallel to anti-parallel spins is related to the strength of the applied field.

Precession:

The influence of B_o produces an additional spin, which is called *precession* and causes the magnetic moments (*Net Magnetization Vector – NMV*) to follow a circular path around B_o , [Kaut98], Figure 2.3. The speed of the NMV is called *precessional frequency* (ω_0) and is governed by the Larmor equation:

$$\omega_0 = B_o \cdot g \quad \text{Eq. 2.2}$$

Where g is the *gyro-magnetic ratio*, an atomic property that is dependent on the type of the nucleus and the external field strength. This means that when spins are perturbed from their preferred axis of alignment, they rotate about this axis at the Larmor frequency. However, individual dipoles are randomly, *out of phase*.

Resonance:

Resonance is a phenomenon that occurs when an object is exposed to an oscillating perturbation that has a frequency close to its own natural frequency of oscillation. Subsequently, when a nucleus is exposed to an external perturbation similar to its precessional frequency then it absorbs energy and causes the NMV to move out of alignment away from B_0 and be *in phase*. In other words, the projections of the magnetic moments on the transverse plane are on the same direction for each proton. The precessional frequency of hydrogen corresponds to the radio frequency (RF) band of the electromagnetic spectrum. The angle to which the NMV moves out of alignment is called the *flip angle*. Usually the flip angle is 90° relative to B_0 , which can be also called the *longitudinal axis/plane*. The plane at 90° to B_0 is called the *transverse plane* Figure 2.3. Apparently, the resonated NMV produces a moving magnetic field. According to Faraday's law of induction if a receiver coil or any conductive loop is placed in the area of a moving magnetic field a voltage is induced in this receiver coil. This is called *Nuclear Magnetic Resonance (NMR)* signal.

A radio frequency pulse can be described as a time-varying magnetic field B_1 , applied to the plane perpendicular to B_0 . If the duration of the RF pulse is t then the flip angle is:

$$\mathbf{a} = \mathbf{g} \cdot B_1 \cdot t \quad \text{Eq. 2.3}$$

and the transverse magnetization immediately after the pulse is:

$$M_{xy} = M \cdot \sin(\mathbf{g} \cdot B_1 \cdot t) \quad \text{Eq. 2.4}$$

This transverse magnetisation induces current in a receiver coil, producing the signal used in MRI. Flip angles are commonly used in MR experiments by setting $t = \mathbf{p}/(2 \cdot \mathbf{g} \cdot B_1)$. For such pulses, all of the magnetisation is flipped into the transverse plane, achieving the strongest possible signal.

Relaxation:

This signal is what the MRI uses to form an image dependent on the amount of the hydrogen atoms in the particular tissue. The frequency of the signal is the same as the Larmor frequency, while the magnitude of the signal depends on the amount of magnetization along the transverse plane. It is essential to understand that the

acquisition of MR images is possible only during *relaxation*, the process by which the NMV loses its energy and is aligned again to B_0 .

Two different types of relaxation are observed in magnetic resonance experiments: *longitudinal, or spin lattice, relaxation* and *transversal or spin-spin relaxation*. *Spin lattice relaxation* is the process of the total net magnetisation NMV aligning over time with the stationary magnetic field B_0 :

$$M_z = M_0 \left(1 - e^{-t/T_1}\right) \quad \text{Eq. 2.5}$$

where T_1 is called the *spin-lattice relaxation time*, and M_0 is the equilibrium magnetization that depends on the proton density and the magnetic field strength, B_0 .

Spin-spin relaxation is due to interactions between spins in the sample (out of phase) and it causes exponential relaxation at the transverse plane:

$$M_{xy} = M_{xy0} e^{-t/T_2} \quad \text{Eq. 2.6}$$

where T_2 is called the spin-spin relaxation time, and M_{xy0} is the transverse magnetisation immediately after the RF pulse, which is equal to M_0 for the 90° RF pulses. Different tissues have different proton density and subsequently different relaxation times T_1, T_2 , which means that their respective transverse magnetization components vary. This variation constitutes the contrast of MR images and is controlled by a great range of parameters analysed in [Kaut98]. If a sequence of 90° RF pulses with a period of T_R , *time of repetition*, is used and the time between the RF pulses is denoted T_E , *time to echo*, ignoring the relaxation effect during the measurement, the transverse magnetisation is:

$$M_{xy}(t) = M_0 \left(1 - e^{-T_R/T_1}\right) \cdot e^{-T_E/T_2} \cdot e^{j\omega t} \quad \text{Eq. 2.7}$$

2.5.2 Gradients

If a receiver coil is placed along the object, the transverse magnetization induces current in the coil. This signal is the integral of the magnetization over the entire volume, [Nayak01]:

$$S(t) = \iiint \hat{M}_{xy}(x, y, z, t) \cdot e^{j(\mathbf{w}(x,y,z,t)t + \mathbf{j}(x,y,z,t))} dx dy dz \quad \text{Eq. 2.8}$$

The task of *spatial encoding* is to vary $\mathbf{w}(x, y, z, t)$ and $\mathbf{j}(x, y, z, t)$ over the volume for every measurement in such a way that can be possible to distinguish the origin of the signal and reconstruct the corresponding image. By using *linear gradients* during reception, a linear frequency shift as a function of space can be applied, thus resulting in a linear phase that accumulates over time.

Magnetic Field Gradients are generated by coils of wire situated within the bore of the magnet. This gradient field interacts with the main static magnetic field, so that the magnetic field strength along the axis of the gradient coil is altered in a linear way. The magnetic field experienced by a nucleus at a position r is given by the sum of the main magnetic field in this position $B_o(r)$ and any applied magnetic-field gradients. In the case of linear gradient field and a homogeneous main field we can write:

$$B(r) = B_o(r) + G_r \quad \text{Eq. 2.9}$$

Where G_r is the component of gradient along the direction of r .

Gradients perform many tasks. In fact, changes in the magnetic field B_o results in altering the Larmor frequency, which is also the frequency of the signal received from different parts of the body when the phenomenon of resonance occurs. In other words, nuclei that experience an increased magnetic field strength due to the gradient increase their precessional frequency, whereas nuclei that experience a lower magnetic field strength due to the gradient decrease their precessional frequency. Therefore, the position of a nucleus along a gradient can be identified according to its precessional frequency.

We need three gradients along the three main axes (X, Y, Z) in order to be able to determine the exact origin of the signal received. The first one selects the image plane of the scanning, *slice selection* (Z), and the rest determine the frequency (X) and the phase (Y) encoding. *Frequency encoding* is performed when the gradient affect the frequency of the signal and *phase encoding* when it affects the phase of the signal.

Slice selection:

If a spatially varying field $B(r)$ is followed by an RF pulse that contains a selected set of frequencies, magnetic resonance will occur only in a sub volume whose Larmor frequency are included in the RF pulse. This technique is common in selective excitation and the selected slice will be:

$$z = \frac{\mathbf{w}}{\mathbf{g} \cdot \mathbf{G}_Z} - \frac{B_0}{G_Z} \quad \text{Eq. 2.10}$$

In order to select of uniform thickness sinc RF pulses are used.

Phase encoding:

After the excitation pulse, the distribution of transverse magnetization in the sample is essentially 2D. If we apply a linear field of gradient G_y , the Larmor frequency distribution will also be linear in y . This will cause variation in the phase of magnetization. After time t , the phase of point (x, y) is determined by the equation:

$$\mathbf{j}(x, y) = (\mathbf{w}(x, y) - \mathbf{w}_0)t = \mathbf{g}G_y y t \quad \text{Eq. 2.11}$$

After the gradient is switched off, the precession frequency returns to a constant value over the plane, while the phase remains proportional to y .

Frequency encoding:

Finally, if a constant gradient G_x is applied to the sample, the frequency of precession will change linearly with location, giving us the x spatial encoding:

$$\mathbf{w}(x, y) = \mathbf{g}G_x x \quad \text{Eq. 2.12}$$

K-space:

For simplicity, if the excited region is a slice in the x - y plane, then equation (7) can be written as, [Nayak01]:

$$S(t) = S(k_x(t), k_y) = \iint \hat{M}_{xy}(x, y, t) e^{-j(k_x x + k_y y)} dx dy = F_{\hat{M}}(k_x, k_y) \quad \text{Eq. 2.13}$$

where $k_x = -\mathbf{g}G_x t$, $k_y = -\mathbf{g}G_y t$ and $F_{\hat{M}}$ is the Fourier transform of the magnetisation at time t . The frequency and phase steps essentially map every location in the excited slice with a distinct pair of a frequency and a phase of the magnetisation precession. The integral of this pattern is the Fourier transform of the magnetisation. The signal measured in one such iteration produces a row in the spatial frequency space (k_x, k_y) , also referred as k -space. Subsequently, each received signal is stored in K Space, which is a 2D matrix with the horizontal axis corresponding to phase and the vertical axis to frequency. After repeating this process several times for different values of G_y the image of transverse magnetisation can be recovered by applying the inverse discrete Fourier transform.

K-space must be sufficiently sampled according to the *Nyquist theorem* to avoid object domain aliasing. If the range of frequencies is reduced, the spatial resolution of the image will go down and the image will look blurred. If the spacing between the measured frequencies is increased the reconstruct image will suffer from wrapping effects, which is that a smaller field of view will be replicated over the image space. The extent of k-space coverage determines the image resolution. The *field of view (FOV)* is the bandwidth of frequency and phase that is accomplished during scanning, and thus the anatomy covered, and its value is determined by the steepness of the gradients slope along the frequency and the phase axis. The larger the FOV the bigger the image plane we visualize and the lower resolution it has.

2.5.3 Advantages and Limitations

The introduction of the Cardiac Magnetic Resonance Imaging (CMRI) over a decade ago has led to development of revolutionary, non-invasive analysis tools for in vivo assessment of heart performance. CMRI has been used to develop and refine models of normal and abnormal myocardial motion, to better understand the correlation of coronary artery disease with myocardial motion abnormalities, to understand the effects of treatment after myocardial infarction, and in combination of stress testing for the early detection of myocardial ischemia, [Kerwin00]. CMRI has unique advantages towards other techniques, as it can provide diagnostic information in anatomy, structure, global and regional function and contraction patterns in patients. This has been indicated in various studies and verified in [Sperling02], where findings from ECG, ECG-gated SPECT, echocardiography and cardiac MRI are presented for a case with HCM.

Contrary to CT and Nuclear Medicine there is no evidence that MRI is hazardous. MRI accurately depicts cardiac structure, function and perfusion with an overall capacity superior to any other single imaging modality. The advantages of MR are the fine discrimination of the soft tissue and blood in myocardium and the high-resolution imaging of the anatomy of the heart in tomographic planes of any desired position and orientation. The last property makes possible the acquisition of 3D information, which is important for the modelling of the heart's motion. Furthermore, the ventricular

assessment of myocardial function using MRI is independent of any ventricular geometry assumptions and has been shown to be accurate and reproducible, [Earls02]. Studies have been performed to determine whether MR imaging can be used to reliably measure global myocardial blood flow and coronary flow reserve in patients with coronary artery disease as compared with such measurements obtained by positron emission tomography (PET). The results are promising, suggesting that MR imaging flow quantification could potentially be used for measuring global myocardial blood flow in patients in whom interventional treatment for coronary artery disease is being evaluated, [Koskenvuo01]. Furthermore, the sensitivity of myocardial perfusion imaging is directly related to its spatial resolution. Indeed, MR for perfusion imaging can detect defects in the subendocardium and lead towards early diagnosis of ischemia and myocardial infraction.

Disadvantages of MRI are long imaging time, the low portability and the comparatively high cost of the equipment. Furthermore, the motion of the object imaged, or of a part of it, during the imaging sequence results in a blurring of the entire image or this part of image, respectively. These phenomena are called *motion artifacts*. The solution to eliminate motion artefacts is to immobilize the patient or imaged objects. This is not possible when the motion is caused by the heart beating or the patient breathing. The solution to these cases is to gate the imaging sequence to the cardiac or respiratory cycle of the patient. Thus, we trigger the acquisition encoding steps to occur at a fixed delay time during the cardiac cycle. By doing this the imaged object is always in the same position. This solves the problem of motion artifacts but limits the number of different scanned position to a number depending on the heart rate. Therefore, the MRI temporal resolution is limited up to a point. This limitation can be overcome by the development of new techniques that continuously acquire images of the heart at sufficient high rates, without cardiac gating and breath-holding. These methods are in early developmental and validation stages, however their results are promising to date.

Apart from its spatial resolution image quality is characterised by its *signal to noise ratio (SNR)*. SNR is determined by the amount of measured magnetisation relative to thermal noise in the image. Transverse magnetisation depends on the power and duration of the RF pulse and on the time interval between excitation pulses T_R . Although, there are several ways to improve the SNR many of the parameters are

limited by physiological factors. Current techniques cannot increase the gradient strength or the RF power significantly as it might cause tissue damage.

2.6 Discussion

This chapter briefly describes a variety of approaches to cardiovascular imaging, intending to emphasize their advantages and weaknesses. It would be useful to summarize their basic features that play a significant role in early, accurate and harmless diagnosis of various, malicious heart diseases, such as ischemia and infraction.

Both X-ray CT and Nuclear Medicine expose the patient to considerable amount of ionising radiation. Indeed, the quality of the acquired images is a compromise between their sensitivity/resolution and the tolerable amount of dose. On the other hand, Ultrasound and MRI permits the massive monitoring of the myocardium function and they have the potential for in vivo 3D visualisation of the cardiac cycle. There is no direct or indirect evidence that any hazard might arise from their normal diagnostic use and this permits their use to systematically record and analyse normal and abnormal causes.

The latest reconstruction techniques in MRI report temporal resolution of 13msec and spatial resolution of 4.1mm, [Earls02]. When designing image sequences, one must make decisions about trade-offs between temporal resolution, spatial resolution and signal strength. In other words, spatial resolution can be increased reversely to temporal resolution and vice versa. X-ray CT has yield temporal and spatial resolution of 50-100msec and 3-2.5mm, respectively, using EBCT scanners, [Regn02]. Ultrasound has temporal resolution of 10msec, while it spatial resolution is about 1-5mm, [D'hooge00].

Advantages of MRI over Ultrasound include the ability to image arbitrary scan planes and the ability to study flow in any direction. Ultrasound is restricted by physical acoustic windows and is limited to imaging flow towards or away from the transducer. The main advantage of MRI over X-ray CT and Nuclear Medicine techniques is that harmful ionising radiation is not used. In addition, MRI is capable of studying a wide variety of processes such as myocardial perfusion, wall motion, valvular flow, and coronary arteries –all in a single examination.

Cardiovascular MRI has the potential to combine all aspects of non-invasive cardiological diagnosis. It offers greater sensitivity and specificity than other techniques, with precisely reproducible slice planes and good spatial and temporal resolution. In its present form, CMR offers significant advantages in studies of cardiac physiology and function, while on-going research can be expected to increase its scope still further. One important area for future work is the integration of several MRI based techniques into a single sequence examination or imaging protocol. In real time imaging this would mean developing ways by which an operator could quickly switch between different imaging sequences while staying focused on anatomical landmarks.

2.7 References and Bibliography

- [D'hooge00] J. D'hooge, A. Heimdal, F. Jamal, T. Kukulski, B. Bijnens, F. Rademakers, L. Hatle, P. Suetens and G. R. Sutherland, 'Regional Strain and Strain Rate Measurements by Cardiac Ultrasound: Principles, Implementation and Limitations', Review Article, Eur J Echoardiography 1, 154-170, 2000
- [Santos01] A. Santos, MJ Ledesma-Carbayo, N. Malpica, M. Desco, JC Antoranz, P. Macros-Alberca and MA Garcia-Fernandez, 'Accuracy of heart strain rate calculation derived from Doppler tissue velocity data', Medical Imaging: Ultrasonic Imaging and Signal Processing, 2001
- [Jersey01] University of Medicine and Dentistry of New Jersey – Robert Wood Johnson Medical School, 'An Electronic Journal for Cardiac Ultrasound', on <http://www2.umdnj.edu/~shindler/index.html>
- [Kaut98] Westbrook Catherine and Kaut Carolyn, 'MRI in Practice', second edition, 1998
- [Guy00] Chris Guy, 'An Introduction to The Principles of Medical Imaging', London: Imperial College Press, 2000
- [Webb92] 'The Physics of Medical Imaging', edited by Steve Webb, chapter 1, 4, Bristol: Hilger, c1988

- [Regn02] K. Klingenbeck-Reng, T. Flohr, B. Ohnesorge, J. Regn and S. Schaller, 'Strategies for cardiac CT imaging', *The International Journal of Cardiovascular Imaging* 18; 143-151, 2002
- [Ohnersoge00] B. Ohnersoge and T. Flohr, 'Non-invasive Cardiac Imaging with Fast Multi-slice Cardio CT', *Electromedica*, 68; 1-10, 2000
- [Koskenvuo01] Koskenvuo JW, Hartiala JJ, Knuuti J, Sakuma H, Toikka JO, Komu M, Saraste M, Niemi P., 'Assessing coronary sinus blood flow in patients with coronary artery disease: a comparison of phase-contrast MR imaging with positron emission tomography', *AJR Am J Roentgenol* 2001 Nov;177(5):1161-6
- [Nayak01] Krishna Nayak, 'Fast Cardiovascular Magnetic Resonance Imaging', PhD thesis awarded by Fannie and John HERTZ Foundation, 2001
- [Earls02] James P. Earls, Vincent B. Ho, Thomas K. Foo, Ernesto Castillo and Scott D. Flamm, 'Cardiac MRI: Recent Progress and Continued Challenges', *Journal of Magnetic Resonance Imaging* 16:111-127, 2002
- [Edvardsen02] Thor Edvardsen, Bernhad L. Gerber, Jerome Garot, David A. Bluemke, Joao A.C. Lima, Otto A. Smiseth, 'Quantitative Assessment of Intrinsic Regional Myocardial Deformation by Doppler Strain Rate Echocardiography in Humans – Validation Against Three-Dimensional Tagged Magnetic Resonance Imaging', *Circulation*, 2002; 106:50-56
- [Sperling02] Sperling RT, Parker JA, Manning WJ, Danias PG, 'Apical hypertrophic cardiomyopathy: Clinical, electrocardiographic, scintigraphic, echocardiographic and magnetic resonance imaging findings of a case', *Journal of Cardiovascular Magnetic Resonance* January 2002, 291-295

Chapter 3 -

Quantification of Intrinsic Cardiac Mechanics

3.1 Introduction

The myocardium is a non-linear viscoelastic anisotropic active material. In order to gain insight into the mechanisms behind heart diseases and to determine their causes, knowledge of the mechanical behaviour of the cardiac muscle is important. Furthermore, the energy consumption of various portions of the myocardium can be estimated by the distribution of mechanical stress throughout the cardiac muscle. Continuum mechanics deals with the movement of materials when subjected to applied forces. The concept of strain, a measure of length change or displacement gradient, and stress, the force per unit area on an infinitesimally small plane surface within the material, are of fundamental importance in assessing the regional function of ventricular muscle and measuring myocardial viability in order to classify whether a heart beats normally or not. In this chapter the basic mathematical formulations are presented, while the most common non-invasive techniques of measuring myocardial strain and strain rate, based on MR, are discussed.

3.2 Eulerian and Lagrangian Strain – Strain Tensor

While investigating the tissue motion it is useful to introduce the mathematical definitions that describe the deformation of its shape locally and globally. Mathematically, the motion can be described by the function $m(p, t)$, called *forward map*, which relates the reference position p to its deformed position m at time t . The reference position p usually in cardiac imaging is defined as the spatial position of p at end diastole, thus when $t = 0$ then $p = m(p, 0)$. Inversely, the *reference map* is the function that relates the spatial position m at time t to the corresponding reference position p . The reference map often is easier to measure than the forward map. However, for visualisation and diagnostic purposes a related motion measurement, strain, is considered more valuable and can be computed from either map.

Strain (\mathbf{e}) is defined as the deformation of an object, normalized to its original shape. Therefore, in 1D this can be written as:

$$\mathbf{e} = \frac{L - L_0}{L_0} \quad \text{Eq. 3.1}$$

With L the length of the object after deformation and L_0 its original length. From Eq.3.2 strain takes negative values when the object is shortening and positive values during its lengthening.

Lagrangian strain ($\mathbf{e}_L(t)$) is the instantaneous strain defined for each moment of the deformation process:

$$\mathbf{e}_L(t) = \frac{L(t) - L(t_0)}{L(t_0)} \quad \text{Eq. 3.2}$$

With $L(t)$ the length of the object at time instance t and $L(t_0) \equiv L_0$ its initial length.

The deformation can also be expressed relative to the length at a previous time instance:

$$d\mathbf{e}_N(t) = \frac{L(t+dt) - L(t)}{L(t)} \quad \text{Eq. 3.3}$$

With dt an infinitesimally small time interval and $d\mathbf{e}_N(t)$ the infinitesimally amount of deformation occurring during this time interval.

Therefore, *natural or Eulerian strain* ($\mathbf{e}_N(t)$) is the instantaneous strain derived from the integration of the Eq.3.3:

$$\mathbf{e}_N(t) = \int_{t_0}^t d\mathbf{e}_N(t) \quad \text{Eq. 3.4}$$

The difference between the Lagrangian (Eq.3.2) and the Eulerian or natural strain (Eq.3.4) is that in the latter the reference value is not constant over time but changes during the deformation process. In the case where the rate of deformation is constant as a function of time, the Lagrangian strain $\mathbf{e}_L(t)$ and the Eulerian strain $\mathbf{e}_N(t)$ have a non-linear relationship:

$$\mathbf{e}_N(t) = \ln(1 + \mathbf{e}_L(t)) \text{ or } \mathbf{e}_L(t) = \exp(\mathbf{e}_N(t)) - 1 \quad \text{Eq. 3.5}$$

However, if the strains are small (of the order of 5-10%) Lagrangian and Eulerian strain values are approximately equal.

For a 3D object the deformation is not limited to lengthening or shortening in one direction. It can lengthen or shorten along the x, y, z axes or can distort by the relative displacement of the borders of the object. The first type of deformation is called *normal strain*, since its associated motion is normal to the border of the object. The second one is called *shear strain* since its associated motion is parallel to the border of the object. For a 3D object there are three normal strains, along the x, y, z axes and six shear strains, xy, xz, yz, yx, zx, zy .

We can write the above components in matrix form referred to as the *strain tensor* F , in order to have a more convenient mathematical formulation:

$$F = \begin{bmatrix} \mathbf{e}_x & \mathbf{e}_{xy} & \mathbf{e}_{xz} \\ \mathbf{e}_{yx} & \mathbf{e}_y & \mathbf{e}_{yz} \\ \mathbf{e}_{zx} & \mathbf{e}_{zy} & \mathbf{e}_z \end{bmatrix} \equiv \begin{bmatrix} \frac{\Delta x}{x} & \frac{\Delta x}{y} & \frac{\Delta x}{z} \\ \frac{\Delta y}{x} & \frac{\Delta y}{y} & \frac{\Delta y}{z} \\ \frac{\Delta z}{x} & \frac{\Delta z}{y} & \frac{\Delta z}{z} \end{bmatrix} \equiv \begin{bmatrix} \mathbf{e}_x & \mathbf{q}_{xy} & \mathbf{q}_{xz} \\ \mathbf{q}_{yx} & \mathbf{e}_y & \mathbf{q}_{yz} \\ \mathbf{q}_{zx} & \mathbf{q}_{zy} & \mathbf{e}_z \end{bmatrix} \quad \text{Eq. 3.6}$$

The shear strain components can be also uniquely determined by the angles $\mathbf{q}_{xy}, \mathbf{q}_{yx}, \mathbf{q}_{xz}, \mathbf{q}_{zx}, \mathbf{q}_{yz}, \mathbf{q}_{zy}$ since their tangents are equal to $\mathbf{e}_{xy}, \mathbf{e}_{yx}, \mathbf{e}_{xz}, \mathbf{e}_{zx}, \mathbf{e}_{yz}, \mathbf{e}_{zy}$, respectively. In Figure 3.1 a normal and a shear strain are depicted.

Knowledge of the strain tensor at a point allows us to find the fractional change in length of an infinitesimal line segment oriented along any direction [Axel92]. Any vector $\vec{\mathbf{c}} = (x, y, z)$ within the element in its initial state will be transformed by motion to a later vector $\vec{\mathbf{c}}' = (x', y', z')$ by the relation:

$$\vec{\mathbf{c}}' = F \cdot \vec{\mathbf{c}} \quad \text{Eq. 3.7}$$

In other words, defining these nine strain components defines completely the deformation of the object. The number of independent strain components could be reduced in the case of homogeneous, isotropic and incompressible media. However, the heart is a complex three-dimensional fibre-wound structure with mechanical properties that are nonlinear, anisotropic, time varying and spatially inhomogeneous, [Masood00].

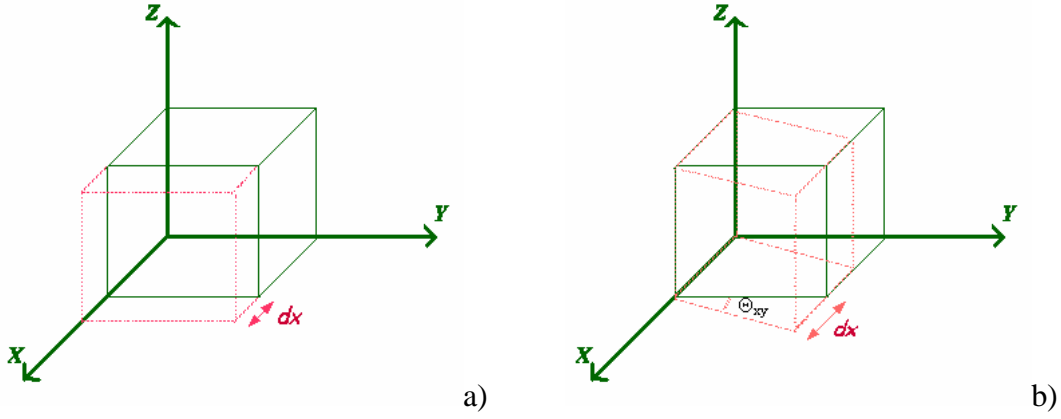


Figure 3.1: Deformation of a 3D object: a) Normal strain e_x , b) Shear strain e_{xy}

3.3 Strain Rate

Strain Rate (\dot{e}) is the speed at which strain deformation occurs and has unit sec^{-1} . Since a 3D object has nine strain components all occurring at a specific rate, nine strain rates can be defined. Since both Eulerian and Lagrangian Strain can be defined, both Lagrangian and Eulerian strain rate can be calculated, Eq.3.8, Eq.3.9, respectively.

$$\dot{e}_L(t) = \frac{\Delta e_L(t)}{\Delta t} = \frac{L(t) - L(t_0)}{t - t_0} = \underbrace{\frac{L(t) - L(t_0)}{t - t_0}}_{\text{Strain Deformation}} \frac{1}{L(t_0)} = \frac{\bar{L}(t)}{L(t_0)} \quad \text{Eq. 3.8}$$

$$\dot{e}_N(t) = \frac{de_N(t)}{dt} = \frac{\frac{L(t+dt) - L(t)}{L(t)}}{dt} = \underbrace{\frac{L(t+dt) - L(t)}{dt}}_{\text{Strain Deformation}} \frac{1}{L(t)} = \frac{L'(t)}{L(t)} \quad \text{Eq. 3.9}$$

Strain deformation is defined as the change in shape that occurs during a period of time Δt per unit time and has unit $m \cdot \text{sec}^{-1}$.

The above definitions infer that both strain and strain rate are closely related and they can be derived one from the other just as velocity can be derived from distance.

3.4 Strain – Wall Thickening

Wall Thickening (WT) is defined as

$$WT = \frac{T_{ES} - T_{ED}}{T_{ED}} \quad \text{Eq. 3.10}$$

with T_{ES} and T_{ED} end-systolic and end-diastolic, respectively. In other words, wall thickening is the myocardial strain measured in one dimension. Since it compares the end-systolic with the end-diastolic wall thickening, which is fixed, the wall thickening parameter measures Lagrangian strain. Thus, the rate at which the myocardial wall thickens and this is the 1D strain rate.

3.5 Coordinate systems

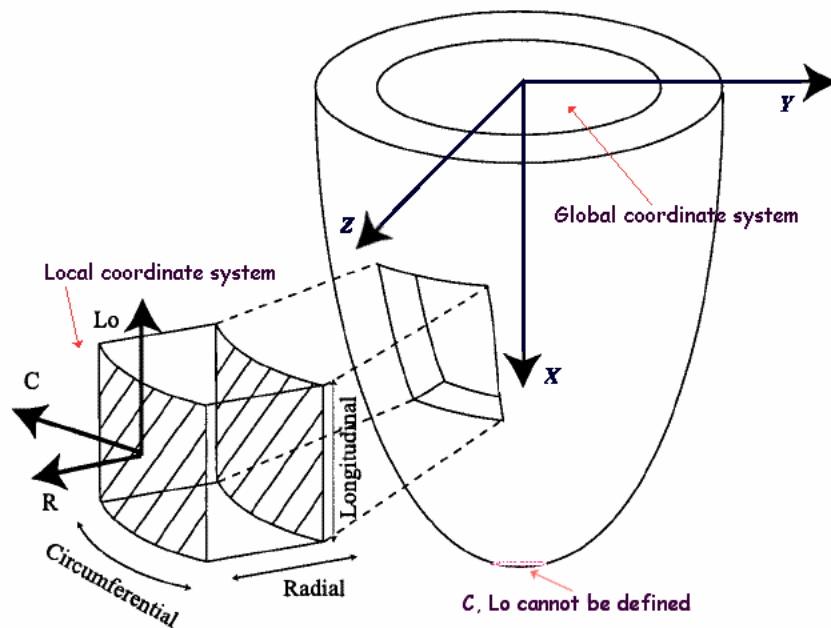


Figure 3.2: Global - Local Coordinate systems

In order to investigate the motion of cardiac tissue as a whole we have to define a coordinate system where a unique coordinate can be ascribed to every single spatial point. Using the most appropriate coordinate system is important, as it facilitates interpretation of the measurements and reduces the mathematical complexity required to describe the deformation. Therefore, it depends on the scanning method used to acquire the motion information and the technique used to process this information.

Generally, either a global Cartesian coordinate system or a local coordinate system can be defined, Figure 3.2.

A *global Cartesian System* (x, y, z) is depicted in Figure 3.2 and can describe the whole heart or the left ventricle (LV). Lagrangian strain is easily estimated here since the calculation of the distances between each axis and a spatial point is straightforward.

However, the local coordinate system, Figure 3.2, facilitates the physical interpretation of the strain measurements of the heart and may be more appropriate for heart motion simulation as the natural or Eulerian strain can be easily estimated. For cardiac applications, it has been suggested that it may be more appropriate to measure the natural strain, since in that case the measured values are less dependent on the definition of the initial length L_0 , Eq.3.2. In the local coordinate system each point can be interrogated in any myocardial wall using three mutually perpendicular axes:

- *The radial (R) axis:* It is perpendicular to the epicardium, pointing outwards, away from the cavity.
- *The longitudinal (L_0) axis:* It is perpendicular the radial axis, tangential to the epicardium, and pointing towards the base of the ventricle, away from the apex.
- *The circumferential (C) axis:* It is perpendicular to both the radial and the longitudinal axis, defined in such a way that R- L_0 -C coordinate system is right handed.

We should point out that the spatial orientation of the three local axes relative to the global coordinate system is different for each point within the ventricle. Moreover, note that this coordinate system cannot be defined for the most distal point of the apex of the ventricle, as here neither a circumferential nor a longitudinal orientation can be defined.

3.6 Different Methods of Measuring Cardiac Strain Using MR

The estimation of regional 3D cardiac deformation is an important issue as ischemic heart disease is a major clinical problem. As it has already mentioned myocardial injury caused by ischemic disease is often regional. It is the fundamental goal of many forms of cardiac imaging and image analysis to measure the regional function of the

left ventricle (LV) in an effort to isolate the location and extent of ischemic or infarcted myocardium. Thus, the estimation of cardiac motion and deformation from MR images has been an area of major concentration in medical image analysis. Invasive and non-invasive techniques have been developed and applied in animals and humans in order to improve clinical diagnosis and treatment and assist research effort towards cardiac exploration.

Invasive approaches are based on implanting devices such as sonomicrometers and radiopaque markers. While this method is accepted as being accurate, only a sparse number of specific sites on LV can be measured due to difficulty in implanting the markers. Therefore, it is not possible to measure a large number of sites simultaneously. Furthermore, there is doubt whether these implanted devices can alter myocardial perfusion and function, [Papademetris00]. Although, this method has been used in humans, obviously, it cannot be applied in standard clinical use and massive monitoring.

Non-invasive methods of measuring strain and strain rate have the potential of in-vivo monitoring of the cardiac cycle, while they assess cardiac deformation for the whole myocardium through out the cardiac cycle. They can be applied limitlessly in clinical use, without exposing the patient's to any danger, thus most of the research effort has turned in this direction.

3.6.1 Non – Invasive Approaches for Measuring Myocardial Deformation

Correspondence Approaches:

These techniques exploit the correspondence between distinct features over time and thus material points can be tracked through out the cardiac cycle. These methods are based on three stages. The first stage requires the extraction of material landmarks or point features. During the second stage the correspondence between landmarks is established over time. Finally, the last stage consists of recovering the motion of the object from the sparse set of the landmarks' trajectories.

MR tagging is the only non-invasive method that can embed a large number of material landmarks in the MR image. The basic principles of MR tagging and their

impact in cardiac imaging is presented analytically in the next chapter. Here, the most common techniques to estimate initial displacement data from magnetic resonance tagging images are mentioned, [Young], [Aletras99]. These can be summarised as, [Papademetris00], tagging in multiple intersecting planes and variable brightness optical flow methods.

The multiple intersecting planes are either generated by imposing a tag-grid pattern in a single acquisition or by tagging along different planes in separate acquisitions and superimposing the tagged planes to create the grid later. Either the intersections points of the tagging grids or the whole of the tag planes can be used as features for the overall estimation scheme. This second approach is more robust to noise as it uses more of the tag-line and it can provide partial information in regions where intersection points are not well defined. However, only displacement perpendicular to tag-plane can be generated, which need to be processed later to generate a full displacement field.

Optical flow approaches attempt to model tag fading over time using a model for the Bloch equation and a variable brightness optical flow approach to extract the displacements from the whole image. Sinusoidal tagging patterns are primarily used, which provide for the smooth intensity fields needed for efficient optical flow computation. The quality of the estimated deformation fields is highest in the middle of the wall and can be very noisy near the myocardial boundaries. This method has the advantage of not having to detect tags explicitly but the brightness variation parameters must be either known or estimated.

Velocity Fields Approaches:

Velocity fields approach contains techniques that exploit time sequences of velocity fields. Instantaneous velocity is estimated everywhere inside the object of interest. These instantaneous Eulerian velocities can be derived from each pixel in an image acquisition. Afterwards, the deformation maps are recovered from the temporal sequence of snapshots of the velocity fields.

MR Phase Velocity Imaging relies on the fact that a uniform motion of tissue in the presence of a magnetic field gradient produces a change in the MR signal proportional to velocity. Indeed, the relationship between the phase of the signal and flow velocity is, [Manning02]:

$$\mathbf{j} = \mathbf{g} \cdot v \cdot \Delta A_g \quad \text{Eq. 3.11}$$

where A_g is the area of one gradient pulse, Δ is the time between the centres of the two gradient pulses, v is velocity and \mathbf{g} is the gyro-magnetic ratio. For a particular imaging sequence A_g , Δ and \mathbf{g} are constants, thus a quantitative measure of velocity can be determined measuring the phase shift.

The two principal approaches of utilizing the phase shift to produce a quantitative measure of velocity are *phase contrast (PC) velocity mapping*, [Zhu96], [Meyer96] [Zhu99-2] and [Arai99], and *Fourier flow imaging*. Normally, phase contrast velocity mapping uses spatial phase encoding gradient, while Fourier flow imaging uses a bipolar velocity phase encoding gradient. In terms of the second stage, there are two approaches in order to extract useful information from phase contrast images. These are based either on processing the data directly to estimate strain rate tensors, [Zhu97], or integrating the velocities, [Meyer96], via some form of tracking mechanism to estimate displacement over time, [Papademetris00].

Assembling the dense field phase velocity information into a complete and accurate 3D myocardial deformation map is a limiting problem for the current technology. Furthermore, current phase contrast velocities estimates near the endocardial and epicardial are less accurate, as the required size of a *region of interest (ROI)*, for signal to noise purposes, is typically large and can include regions from outside the myocardial wall. Thus, as with MR tagging the most accurate LV function is obtained from the middle of the myocardial wall and the least accurate information is usually near the endocardial and epicardial wall boundaries.

Furthermore, in practice serious numerical difficulties arise when Eulerian velocity fields are integrated in order to yield the path of each material point. At a given instance the estimated position may not correspond to the true position of the material point. Therefore, the velocity at this location will not coincide with the true velocity. If we integrate this velocity in order to estimate the position at the next instant, then errors in the position will be amplified, [Meyer96]. Effort has been done to correct these errors by forward and backward integration over time. However, this algorithm tends to underestimate motion due to limited temporal sampling. [Zhu96]-[Zhu99] proposed a new tracking scheme that solves this problem by integrating the velocity fields in the frequency domain. However, the improved accuracy of the Fourier

integration method comes at expense to noise or reproducibility. Extension of this work proposes a global model based computational method that uses the velocity samples from a large portion of the myocardium and all time frames, [Zhu99-1]. This approach may be more reproducible and can also be more efficient in estimating the whole-body strain field.

Finally, the time step between two velocity fields is not controllable and thus the integration can yield inaccurate results when the object is undergoing a large acceleration, [Meyer96]. For this case, one simple approach to improve the overall accuracy of the method is to adjust the velocity sensitivity of the sequence so that the velocity related phase shift is close to $2p$ for the maximum expected velocity, [Manning02].

3.7 Discussion

Currently, the most promising non-invasive technology used to characterize myocardial deformation patterns during the heart cycle is MRI tissue tagging. MR phase encoding has certain limitations. Velocity data are extremely noisy near the LV borders. This deteriorates the inherent accumulation error introduced by the integration of velocity fields in order to extract deformation. On the other hand, assessing myocardial strain and deformation from tagged images require considerable human intervention and thus is time consuming, which limits its application in clinical use. This project combines the principle ideas of both methods, using HARP MR images, in order to introduce a technique that has the potential to be fully automated and in real time.

3.8 References – Bibliography

- [Beache95] Beache GM, Wedeen VJ, Weisskoff RM, OOGara PT, Poncelet BP, Chesler DA, Brady TJ, Rosen BR, Dinsmore RE. 'Intramural Mechanics in Hypertrophic Cardiomyopathy: Functional mapping with Strain-Rate MR Imaging', *Radiology*, 197:117-124, 1995

- [Robson96] Matthew S. Robson and R. Todd Constable, 'Three-Dimensional Strain – Rate Imaging', *Magnetic Resonance in Medicine*, 36:537-546, 1996
- [Meyer96] Francois G. Meyer, Todd Constable, Albert J. Sinusas and James S. Duncan, 'Tracking Myocardial Deformation Using Phase Contrast MR Velocity Fields: A Stochastic Approach', *IEEE Transactions on Medical Imaging*, vol. 15, no. 4, August 1996
- [Zhu96] Yudong Zhu, Maria Dramgova and Norbert J. Pelc, 'Fourier Tracking of Myocardial Motion Using Cine-PC Data', *Magnetic Resonance in Medicine*, 35:471-480, 1996
- [Zhu97] Yudong Zhu, Maria Dragova and Nobert J. Pelc, 'Estimation of Deformation Gradient and Strain from Cine-PC Velocity Data', *IEEE Transactions on Medical Imaging*, vol. 16, no. 6, December 1997
- [Young98] Alistair A. Young, 'Model Tags: Direct 3D Tracking of Heart Wall Motion from Tagged Magnetic Resonance Images', *Proc Medical Image Computing and Computer-Assisted Intervention*. Boston October 11-13 1998
- [Aletras99] Antony H. Aletras, Robert S. Balaban and Han Wen, 'High-Resolution Strain Analysis of the Human Heart with Fast-DENSE', *Journal of Magnetic Resonance*, 140:41-57, 1999
- [Zhu99-1] Yudong Zhu and Norbert J. Pelc, 'A Spatiotemporal Model of Cyclic Kinematics and Its Application to Analyzing Non-rigid Motion with MRI Velocity Images', *IEEE Transactions on Medical Imaging*, vol. 18, no. 7, July 1999
- [Zhu99-2] Yudong Zhu and Norbert J. Pelc, 'Three-Dimensional Motion Tracking with Volumetric Phase Contrast MR Velocity Imaging', *Journal of Magnetic Resonance Imaging* 9:111-118, 1999
- [Arai99] Andrew E. Arai, Carl C. Gaither, Frederick Epstein, Robert S. Balaban and Steven D. Wolff, 'Myocardial Velocity Gradient Imaging by Phase Contrast MRI with Application to Regional

- Function in Myocardial Ischemia', *Magnetic Resonance in Medicine*, 42:98-109, 1999
- [Papademetris00] Xenophon Papademetris, 'Estimation of 3D Left Ventricular Deformation from Medical Images Using Biomechanical Models', Phd thesis, May 2000
- [McVeigh01] Elliot McVeigh and Cengizhan Ozturk, 'Imaging Myocardial Strain', *IEEE Signal Processing Magazine*, 44-56, November 2001

Chapter 4 – Myocardial Tagging with Magnetic Resonance

4.1 Introduction

Many cardiac diseases can affect the systolic function of the heart. A patient may have significant regional dysfunction while maintaining an ejection fraction within normal limits. Assessment and quantification of cardiac function is thus important for diagnosis and treatment of heart disease. Cine MRI has many limitations, especially for the measurement of regional systolic function. The three-dimensional motion of the curved heart wall through the fixed imaging plane can affect the apparent local motion in the two-dimensional image. In addition, the lack of identifiable landmarks within the heart wall makes assessment of motion very limited. Tagged MRI is a non-invasive technique that has the potential to significantly improve the evaluation of cardiac function, including the ability to provide novel information about regional function. Indeed, MR Tagging can be used to track specific myocardial points throughout the cardiac cycles without the use of invasive landmarks such as radiopaque markers or sonomicrometers. In this chapter the basic principles of CMR tagging are analysed and the evolution of the technique since its establishment in MRI is presented, [Axel89].

4.2 Measuring Myocardial Contractility Using MR Tagging

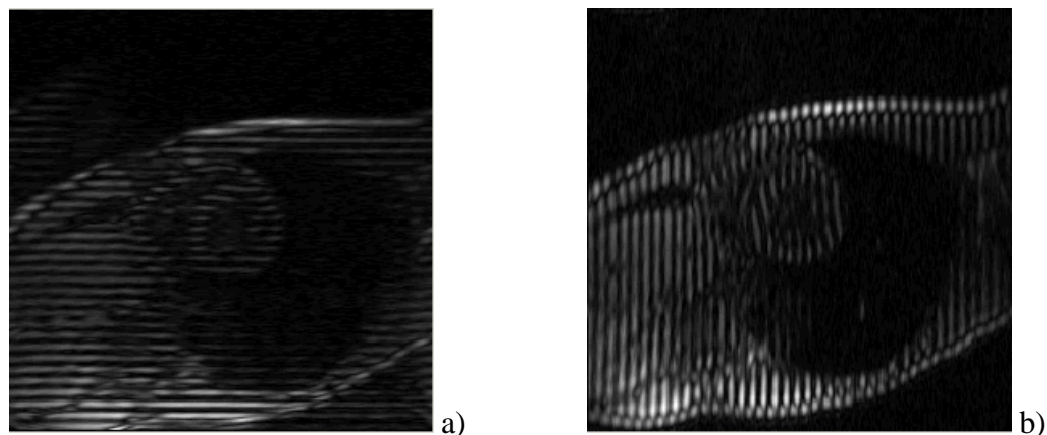


Figure 4.1: a) Horizontal tags, b) Vertical Tags

Once we have imaged the heart during the cardiac cycle we want to calculate the relative deformation of the myocardium between two different time frames. The primary problem is that the myocardium is quite uniform, providing few readily identifiable features in the images. The process of *MR tagging* uses a special pulse sequence to spatially modulate the longitudinal magnetization of the subject to create temporal dark features, called *tags*, in the myocardium, Figure 4.1. This grid provides landmarks that can be used to track the myocardial motion [Masood00]. As the altered magnetization is a property of the tissue and will move with it, any motion during the interval between tagging and imaging will be reflected in the corresponding displacement of the dark band in the images. The imposed tags can be either a Cartesian grid of points, [Axel89]-[Axel92], or a radial tagging in a polar coordinate system, [Bolster90]. Analysis of the motion of the tag features in many images taken from different orientations and at different times can be used to track material points in 3-D leading to detailed maps of the strain patterns within the myocardium, [Axel92], [Kerwin00].

Although, MR tagging has not been established as a standard clinical tool, it is a useful research tool. Results from MR tagging have been found to agree well with echocardiographic data, [Masood00]. It has been proven that tagging enables accurate measurement for diseases such as hypertrophic cardiomyopathy (HCM), [Dong94], arteriosclerosis and to better understand the correlation of coronary artery disease with myocardial motion abnormalities.

4.3 Spatial Modulation of Magnetisation (SPAMM)

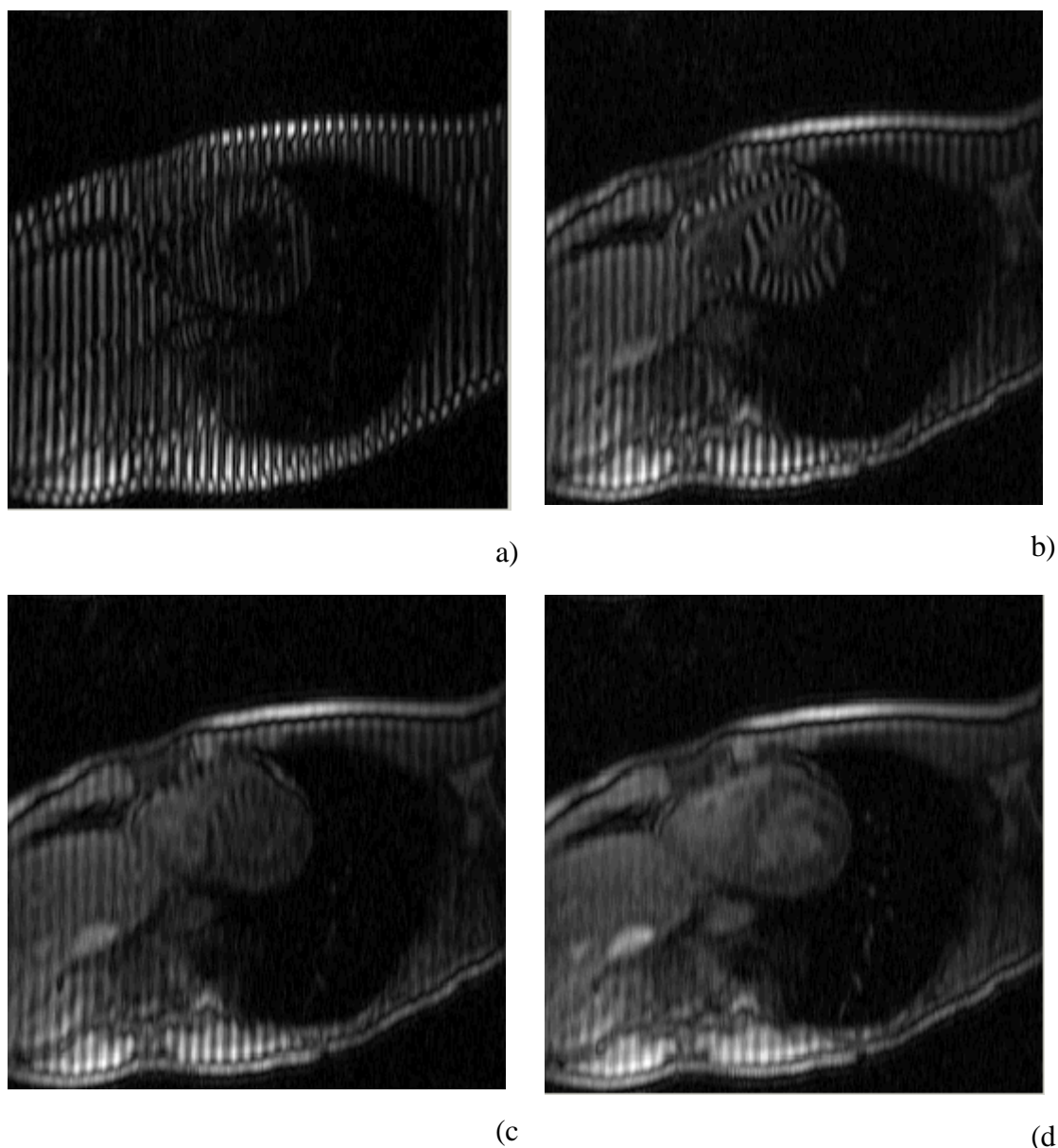


Figure 4.2: a) Time frame 2/16, b) Time frame 7/16, c) Time frame 11/16, d) Time frame 15/16

Tags have faded considerably

The most commonly used sequence of pulses for MR tagging produces a relatively simple spatial modulation of magnetization (SPAMM), [Axe1-1-89], [Axe1-2-89]. Starting from a condition of uniform longitudinal magnetization, the initial proposed scheme, [Axe1-1-89], involves a RF pulse, which turns the NMV into transverse magnetization with the same phase. Subsequently, a gradient pulse produces a periodic spatial modulation of the phase of the transverse magnetization ('wrapping') along the direction of the gradient. Finally, the second RF pulse mixes the modulated

transverse magnetization producing modulated longitudinal magnetization. In the subsequent imaging sequence the modulated longitudinal magnetization results in a corresponding intensity modulation in the final image, appearing as regularly spaced stripes, tags. The orientation of the tags is determined by the direction of the wrap gradient and the spatial frequency of the tag pattern is proportional to the strength and duration of the wrap gradient. A limitation of the technique it is that produces stripes with sinusoidal intensity profiles, which affect the three dimensional analysis of myocardial motion as their profile results in an overall decrease in the signal to noise ratio of the image making it more difficult to appreciate the underlying anatomy. The ideal saturation tag should have a rectangular intensity profile and the tag width to separation ration should be easy to vary.

An improved version of SPAMM is proposed by [Axel-89] and it considers the substitution of more RF pulses with their relative amplitudes distributed according to the binomial sequence, resulting in sharper stripes. In fact, this technique significantly improves the quality of stripes and permits the use of SPAMM to produce a two-dimensional grid of stripes. Generally, the applied tag pattern can be considered as a function $f(p)$, [Kerwin00], that modulates the steady-tissue magnetization of each material point p and must satisfy $|f(p)| \leq 1$. For a SPAMM sequence applied at $t = 0$ the tag pattern is:

$$f(p) = \sum_{n=0}^{N-1} a_n \cos(n g^T p) \quad \text{Eq. 4.1}$$

Where N is the number of pulses applied, a_n are coefficients determined by the flip angles of the RF pulses and g is the matrix of the gradient pulses.

Two SPAMM sequences are often applied in rapid succession with orthogonal direction resulting in a grid pattern given by:

$$f(p) = \sum_{n=0}^{N-1} a_n \cos(n g_1^T p) \cdot \sum_{n=0}^{N-1} a_n \cos(n g_2^T p) \quad \text{Eq. 4.2}$$

Where g_1, g_2 are the two gradients directions.

Neither 1-1 SPAMM nor high-order SPAMM provides the flexibility to alter the ration of tag width to tag separation. Later research has improved the contrast of tagging images and has added flexibility of tag spacing, thickness and high resolution.

[Wu02] proposes a sinc-modulated RF pulse train in the presence of constant gradient. This RF pulse train yields a rectangular profile of saturated magnetisation while the bandwidth of the sinc-function controls the width of the saturation tag. This method can be extended to 2D and 3D tagging without causing loss in untagged areas.

However, in SPAMM tagging the tag lines are not very well resolved, especially in the later frames of the cardiac cycle, as tag-fading occurs because of the relaxation of the magnetization. The contrast between the tissue and the tags decreases considerably during the later phases of the cardiac cycle, Figure 4.2. Thus, the tracking is possible only during systole or diastole and not for a complete heart circle. The problem of decaying and the multiple acquisitions, which are required to assemble 3D information, are serious limitations of this technique.

4.4 Complementary Spatial Modulation of Magnetisation (CSPAMM)

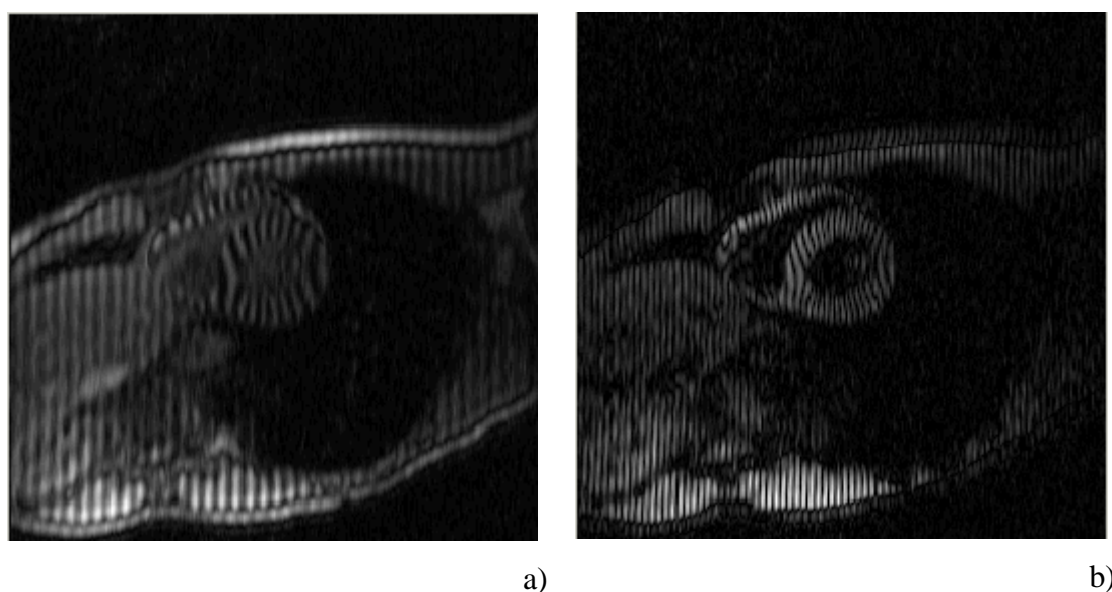


**Figure 4.3: Time frame 8/16 (ABS) - a) Before CSPAMM subtraction
b) – CSPAMM after subtraction**

SPAMM suffers from a rapid fading of the tags, restricting its application mainly to systolic phases of the cardiac cycle. However, left ventricular diastolic dysfunction has been increasingly appreciated as a major cause of heart failure, [Stuber99-1]. *Complementary Spatial Modulation of Magnetisation (CSPAMM)* is an innovative technique of tagging to improve the contrast of tags in the image and minimise their

fading during the later heart phase due to longitudinal relaxation, [Fischer93], Figure 4.3.

The ability of tagging identification can be measured objectively by introducing the *tagging contrast*. In [Fischer93] the tagging contrast is defined as the ratio between the amplitude of the tagging modulation, Q_T , and the maximum image amplitude within a specified area of the image. The improvement in contrast greatly enhances the possibility of using automatic tracking techniques. In order to explain how CSPAMM amplifies tagging contrast we should investigate the reasons for tag pattern fading.

We assume that n images, which lie on the (x, y) plane, are acquired with SPAMM multiphase imaging sequence. M_0 is a spatial dependent magnetization of the object before any MR experiment has been performed. M_{SS} is the magnetization component before the tagging sequence is applied. The sequence of pulses consist of a tagging grid at t_0 , the first RF pulse with flip angle a_1 at t_1 , the second RF pulse with flip angle a_2 at t_2 , and so on, and the n -th pulse with flip angle a_n at t_n .

The z magnetization M_z before the first RF imaging excitation pulse, at t_1 , can be expressed as the contribution of two components. The first component $Q_T(t_1)$ contains the tagging information and the second $Q_R(t_1)$ is the part of magnetization that has relaxed since the application of the tagging pattern.

$$M_z(t_1) = \underbrace{M_{SS} \cdot f(p) \cdot e^{-\frac{t_1}{T_1}}}_{Q_T(t_1)} + \underbrace{M_0 \left(1 - e^{-\frac{t_1}{T_1}}\right)}_{Q_R(t_1)} \quad \text{Eq. 4.3}$$

$f(p)$ is the tagging function, Eq.4.2 and T_1 is the relaxation time.

Subsequently, the longitudinal magnetization M_z before the RF excitation pulse of the k -th heart phase image can be written as:

$$M_z(t_k) = \underbrace{M_{SS} \cdot f(p) \cdot e^{-\frac{t_k}{T_1}} \cdot \prod_{j=0}^{k-1} \cos a_j}_{Q_T(t_k)} + \underbrace{\left(Q_R(t_{k-1}) \cos a_{j-1} - M_0 \right) e^{-\frac{t_k - t_{k-1}}{T_1}} + M_0}_{Q_R(t_k)} \quad \text{Eq. 4.4}$$

The xy magnetization, which contributes to the k -th image I_k is the sum of the tagging component $Q_T(t_k)$ and the relaxed component, $Q_R(t_k)$, rotated into xy plane by the excitation angle a_k :

$$I(t_k) = (Q_T(t_k) + Q_R(t_k)) \cdot \sin a_k \quad \text{Eq. 4.5}$$

The tagging contrast, considering the above definition and Eq.4.5, is given as:

$$\text{tagging - contrast} = \frac{Q_T(t_k)}{Q_T(t_k) + Q_R(t_k)} \quad \text{Eq. 4.6}$$

Therefore from Eq.4.4 and Eq.4.6 we can conclude that tagging fading in later images of the heart cycle results from the decrease of the tagging component $Q_T(t_k)$ and the increase of $Q_R(t_k)$, which inherently does not contain tagging information. $Q_T(t_k)$ reduces due to relaxation, which is expressed by the exponential component of $Q_T(t_k)$ in Eq.4.4 and the RF excitation pulses of the imaging sequence, expressed as the product sequence of cosines of the respective flip angles. $Q_R(t_k)$ increases at the later frames, especially when the relaxation time T_1 is small.

The basic idea of the tagging contrast enhancement proposed by [Fischer93] is based on eliminating the relaxed component $Q_R(t_k)$ by subtracting two images A and B with different tagging functions $f_A(p)$ and $f_B(p)$ respectively. The subtraction of both k -th images of the sequence leads to:

$$\begin{aligned} I_{CSPAMM}(t_k) &= A(t_k) - B(t_k) \propto \\ &\propto M_{SS}[f_A(p) - f_B(p)] \cdot e^{-\frac{t_k}{T_1}} \left(\prod_{j=0}^{k-1} \cos a_j \right) \sin a_k \end{aligned} \quad \text{Eq. 4.7}$$

Eq.4.7 shows that not only has the relaxation component $Q_R(t_k)$ been eliminated but further more we can amplify the tagging-contrast by choosing tagging functions $f_A(p)$ and $f_B(p)$ that satisfy the Eq.4.8:

$$f_A(p) + f_B(p) = 0 \quad \text{Eq. 4.8}$$

Experimentally, two tagging grids that satisfy Eq.4.8 can be induced by two sequences of 1-1 binomial SPAMM pulses. One of the four pulses has to be -90° and the rest 90° in order to obtain maximum tagging contrast. To obtain vertical and

horizontal tags, the imaging is repeated with a x tagging gradient and the a y tagging gradient. It should be noted that using CSPAMM doubles scan time needed.

4.4.1 Extension of CSPAMM and further improvements

Further improvements of scanning time are proposed in [Stuber99-1], where a combination of slice-following CSPAMM myocardial tagging with a segmented *echo-planar imaging (EPI)*, [Tang95], sequence together with an optimised RF excitation scheme enables to acquire images during a single breath-hold. Therefore, image acquisition duration is reduced from several minutes to some seconds. In addition, artifacts related to inconsistent depths of subsequent breath-holds are compensated. Hereby, systolic and diastolic phases of the cardiac cycle can be assessed reliably and fast with a high temporal resolution.

Imaging processing techniques have been developed that improve tagging contrast without increasing scanning time. Indeed, histogram modification has been reported that increase tagging contrast up to 40% by altering faded tagged images such that their intensity histograms approximate the shape of the first, unfaded image of the series, [Koerkamp99]. These techniques can be easily implemented and combined with existing MRI tagging methods in order to asses myocardial mechanic function.

Another limitation of tagging techniques is the low resolution of the tagging grid since only a limited number of labels are marked on the myocardium. This affects especially motion tracking of the right ventricle, because its wall thickness is relatively small with respect to the tag-line distance, [Stuber99-2]. Furthermore, a higher resolution of the tagging grid would also be important for the assessment of strain and strain tensors of the myocardium. In [Stuber99-2] an extension of CSPAMM, which allows a shift of the tagging grid to any position of the imaged slice, is proposed. This strategy is not limited to tagging techniques based on 1-1 SPAMM sequence but can be adapted to any tagging sequence, such as a higher order SPAMM and DANTE. The basic idea is that the tagging grid can be shifted to any desired location by the application of a phase shift to the tagging RF pulse linearly dependent on k-space position. Two images are acquired that are evaluated separately. The displacement of the labelled points of both images result in double resolution. However, the need of multiple acquisitions is a serious drawback of this technique.

4.5 Delay Alternating with Nutations for Tailored Excitation (DANTE)

In [Mosher90] is presented an alternative way of tagging similar to SPAMM. This pulse sequence distributes the power over a series of excitation bands by applying a series of short pulses separated with delay. The idea behind DANTE is to apply a small angle pulse and then wait for a small delay during which magnetization evolve according to chemical shift and coupling constant. By applying a second small pulse after the delay, constructive effect will be observed only on the magnetization that is properly lined up. Specifically, the DANTE pulse train causes selective excitation at the frequency of the scanner and at the DANTE harmonic frequencies. This results in placing tagging in one dimension. Repeating the process across along an orthogonal axis generates a grid pattern of tags.

The distance between tagging planes is determined by the magnitude of the applied field gradient and the DANTE inter-pulse delay. Tag thickness is inversely proportional to the total length of the composite DANTE pulse train. The tag to image contrast is a function of the spin lattice relaxation time T_1 the pulse repetition time TR , the flip angle of the tagging pulse and the time period between tag placement and the subsequent imaging sequence. The advantage of DANTE over SPAMM is the flexibility of tagging spacing and thickness and the high spatial resolution of tags.

In the *Double-DANTE Tagging (DDT)* experiment phase modulation of the DANTE pulse train can be used to excite the sample at two different frequencies, thereby doubling the number of tags. This can be extended to four frequencies, resulting in quadrupling the number of tags placed in a set period of time. A useful feature of DDT is the ability to measure absolute field strength with a single image. Thus, it can be used successfully to measure susceptibility effects in heterogeneous samples, which provides important diagnostic information that can assist in the interpretation of images obtained with other MRI techniques, [Mosher91-1]. Furthermore, it can be used to evaluate spectral artifacts generated by static magnetic field inhomogeneity and contribute towards developing methods for minimizing their effects, [Mosher91-2]. Research effort has been also focused on generating uniform contrast tags across the myocardium wall even in the presence of inhomogeneities of the main electromagnetic field, [Tsekos94].

There are various techniques, where the designing sequences of pulses combine SPAMM and DANTE, [McVeigh92], [Perman95], in order to increase the flexibility of tagging spacing and thickness, while minimise the time needed to produce the tagging pattern. These are also called *hybrid DANTE*.

4.6 Discussion

Tagged CMR is already a useful tool for cardiac research. It has made valuable contribution to the understanding of both normal and abnormal cardiac physiology, [Reichek99]. It has emerged that, normally, fiber strain is fairly uniform across the wall of the left ventricle, while in ischemic heart disease provides a measure of heterogeneity, which underlying myocardial viability. Tagging approaches are an efficient way of tracking tissue motion and certainly show promise because of the inherent capability of including discernible patterns that deform with the tissue. However, there are certain limitations that hamper its establishment as a standard clinical tool. It is difficult to track the tags over the complete LV cycle due to decay of the tags with time. Although, CSPAMM can be used to alleviate tagging fading, the tagging component $Q_T(t_k)$ is still susceptible to spin-lattice relaxation T_1 and the RF excitation pulses of the image sequence. Furthermore, multiple acquisitions are required to assemble 3D information. This increases the overall scanning time and requires multiple breath-holds that amplify the errors due to mismatch and motion artifacts. Thus, real-time display is not possible due to prolonged scanning time and the difficulty associated with assembling the detected tags into a robust 3D analysis and display.

4.7 References and Bibliography

- [Axel-1-89] L. Axel and L. Dougherty, 'MR imaging of motion with spatial modulation of magnetization', *Radiology*, 171:841–845, 1989
- [Axel-2-89] L. Axel and L. Dougherty, 'Heart wall motion: improved method of spatial modulation of magnetization for MR imaging', *Radiology*, 172:349, 1989.

- [Mosher90] Mosher TJ and Smith MB, 'A DANTE tagging sequence for the evaluation of transitional sample motion', *Magnetic Resonance in Medicine*, 15:334-339, 1990
- [Bolster90] Bradley D. Bolster, Elliot R. McVeigh and Elisas A. Zerhouni, 'Myocardial Tagging in Polar Coordinates with Use of Striped Tags', *Cardiac Radiology*, 173(3):769-772, 1990
- [Mosher91-1] Mosher TJ and Smith MB, 'Magnetic Susceptibility Measurement Using a Double-DANTE Tagging (DDT) Sequence', *Magnetic Resonance in Medicine*, 18:251-255, 1991
- [Mosher91-2] Mosher TJ and Smith MB, 'Mapping the Static Magnetic Field Using a Double-DANTE Tagging Sequence', *Journal of Magnetic Resonance*, 93:624-629, 1991
- [Axel92] Leon Axel, Roberto C. Goncalves and Daniel Bloomgarden, 'Regional Heart Wall Motion: Two-dimensional Analysis and Functional Imaging with MR Imaging', *Radiology*, 183(3):745-50, 1992 June
- [McVeigh92] Elliot McVeigh and Ergin Atalar, 'Cardiac Tagging with Breath-hold CINE MRI', *Magnetic Resonance in Medicine*, 28:318-327, 1992
- [Fischer93] Fischer SE, McKinnon GC, Maier SE, Boesiger P., 'Improved myocardial tagging contrast', *Journal of Magnetic Resonance and Medicine*, 30(2):191-200, August 1993
- [Tsekos94] Nikolas V. Tsekos, Michael Garwood, Hellmut Merkle, Ya Xu, Norbert Wilke and Kamil Ugurbil, 'Myocardial Tagging with B₁ Insensitive Adiabatic DANTE Inversion Sequences', *Magnetic Resonance in Medicine*, 34:395-1994
- [Dong94] Sheng-Jing Dong, John H. MacGregor, Adrian P. Crawley, Elliot McVeigh, Israel Belenkie, Eldon R. Smith, John V. Tyberg and Rafael Beyar, 'Left Ventricular Wall Thickness and Regional Systolic Function in Patients With Hypertrophic Cardiomyopathy', *Circulation*, 90:1200-1209, 1994
- [Perman95] William H. Perman, Lawrence L. Creswell, Stephan G. Wyers, Michael J. Moulton, Michael K. Pasque, 'Hybrid DANTE and Phase-Contrast Imaging Technique for Measurement of Three-dimensional

- Myocardial Wall Motion', *Journal of Magnetic Resonance Imaging*, 1995, 5:101-106
- [Tang95] Chao Tang, Elliot R. McVeigh and Elias A. Zerhouni, 'Multi-Shot EPI for Improvement of Myocardial Tag Contrast: Comparison with Segmented SPGR', *MRM* 33:443-447, 1995
- [Ruckert97] Daniel Ruckert, Segmentation and Tracking in Cardiovascular MR Images Using Geometrically Deformable Models and Templates', PhD thesis, Imperial College of Science, Technology and Medicine, Department of Computing, October 1997
- [Stuber99-1] M. Stuber, M.A. Spiegel, S.E. Fischer, M.B. Scheidegger, P.G. Danias, E.M. Pedersen and P. Boesiger, 'Single breath-hold slice-following CSPAMM myocardial tagging', *Magnetic Resonance Materials in Physics, Biology and Medicine* 9 (1999) 85-91
- [Stuber99-2] M. Stuber, Stefan E. Fischer, M.B. Scheidegger and P. Boesiger, 'Towards High-Resolution Myocardial Tagging', *Magnetic Resonance in Medicine* 41:639-643, 1999
- [Koerkamp99] M.A.M. Groot Kowrkamp, G. Snoep, A.M.M. Muijtjens and G. J. Kemerink, 'Improving Contrast and Tracking of Tags in Cardiac Magnetic Resonance Images', *Magnetic Resonance in Medicine* 41:973-982, 1999
- [Reichek99] Nathaniel Reichek, 'MRI Myocardial Tagging', *Journal of Magnetic Resonance Imaging*, 10:609-616, 1999
- [Geest99] Rob J. van der Geest and Johan H.C. Reiber, 'Quantification in Cardiac MRI', *Journal of Magnetic Resonance Imaging*, 10:602-608, 1999
- [Masood00] Masood S, Yang GZ, Pennell DJ, Firmin DN, 'Investigating intrinsic myocardial mechanics: the role of MR tagging, velocity phase mapping, and diffusion imaging', *Journal of Magnetic Resonance Imaging*, 12(6):873-83, 2000 Dec
- [Wu02] Ed X. Wu, Christopher W. Towe and Haiying Tang, 'MRI Cardiac Tagging Using a Sinc-Modulated RF Pulse Train', *Magnetic Resonance in Medicine* 48:389-393, 2002

Chapter 5 – HARP MRI

5.1 Introduction

HARP MRI stands for Harmonic Phase Magnetic Resonance Imaging and it is a revolutionary technique of extracting motion and strain information from tagged MR images. Invented and developed by [Osman98]-[Osman01] it is an innovative way to rapidly process tagged MR images without human intervention. This method overcomes the limitations of conventional tagging techniques where the processing and tracking of tag lines require the post-processing of many hours. Although, MRI tagging is a useful research tool for predicting and challenging lethal cardiovascular diseases, it has certain limitations. These are, basically, the high cost of the equipment and the long time required to process the sequences of images containing the tissue deformation during the cardiac cycle. *HARP* can provide reliable results within one minute and has the potential of real-time acquisitions. Therefore, it can contribute towards reducing the overall cost and developing 3D reconstruction techniques of the cardiac cycle, which will provide clinicians with a fully, detailed explanation of how the most vital muscle of human body operates. This would climax the exploration of cardiac tissue behaviour and its mechanical characteristics and it would be invaluable in various applications, such as prediction and diagnosis of heart disease, and checking the effectiveness of new drugs designed to restore the damage of stunned heart tissue. The *HARP* technique brings *MRI* closer to being established as a clinical tool and provides the medical imaging research world with an invaluable inspiration for further improvement and development. This chapter fully investigates the concepts behind *HARP MRI* and the advantages/limitations of the method. Estimation of velocity fields and instantaneous strain maps using *HARP MRI* are also investigated as a proof of flexibility, convenience and rapidity of the technique.

5.2 Introducing *HARP* – Basic Principles

There are interesting properties of MR tagging that emerge when we investigate MR imaging in the frequency domain. Indeed, information about tissue deformation can be extracted by the change of the local frequency of tag lines, [Osman98] -

[Osman01], [Bayram01]. Generally, tagging produces several one-dimension sinusoidal tag patterns at a certain spatial frequency. A local deformation of the myocardium produces a variation in the local frequencies of these patterns, which can be used to directly calculate components of the Eulerian strain tensor and velocity fields. This information can be easily extracted from the Fourier transform of a 1-D/2-D SPAMM or CSPAMM image using a bandpass filter. Firstly, we will define the mathematical formulations of tagging patterns in order to reveal the relationship between the tagged image and the motion information extracted from its frequency domain.

5.2.1 Tagging MRI – Mathematical Description

We define as $i(\bar{y}, t)$ the brightness of a MR image at position $\bar{y} = [y_1, y_2]^T$, which is the 2-D image coordinate vector. Each image coordinate \bar{y} is related to its 3-D position x by the function:

$$x(y) = y_1 \bar{h}_1 + y_2 \bar{h}_2 + \bar{x}_0 = \bar{H}\bar{y} + \bar{x}_0 \quad \text{Eq. 5.1}$$

where \bar{h}_1 and \bar{h}_2 are 3-D, orthogonal unit vectors describing the image orientation and \bar{x}_0 is the image origin. Thus, we can describe a tagged image i_{TAG} as:

$$i_{TAG}(\bar{y}, t) = i_{orig}(\bar{y}, t) \cdot f(\bar{y}, t) \quad \text{Eq. 5.2}$$

where i_{orig} is the image that would have been obtained without tagging and $f(\bar{y}, t)$ is the faded and deformed tagged pattern. $f(\bar{y}, t)$ can be approximated by the function, [Kerwin00]:

$$f(\bar{y}, t) = \mathbf{b}(t)f_0(p(\bar{y}, t)) + (1 - \mathbf{b}(t)) \quad \text{Eq. 5.3}$$

where $\mathbf{b}(t)$ represents tag fading and is a monotonically decreasing function. $f_0(\bar{y}, t)$ is the tagging pattern, which in case of SPAMM is given from Eq.4.1 – Eq.4.2. $p(\bar{y}, t)$ is the material point, which at time t is located at the spatial position \bar{y} .

1-D 1-1 SPAMM:

In case of 1-D 1-1 SPAMM an MR tag pattern is generated at end-diastole $t = 0$ by the application of an \mathbf{a} -degree pulse followed by an applied transverse gradient of direction and strength \bar{w} , followed by another \mathbf{a} -degree pulse, and completed by

crashing all lateral magnetisation, [Osman98]. In this case the tag pattern can be defined as:

$$f_0(p; \bar{w}, \mathbf{a}, \mathbf{q}) = \cos^2(\mathbf{a}) + \sin^2(\mathbf{a}) \cos(\bar{w}^T p + \mathbf{q}) \quad \text{Eq. 5.4}$$

where \mathbf{q} is a fixed shift for the SPAMM pattern. This equation can be also extracted from Eq.4.1 for $N = 2$.

2-D 1-1 SPAMM:

A 2-D 1-1 SPAMM pattern can be generated by applying two 1-D 1-1 SPAMM sequences in rapid succession. We can assume that their directions are \bar{w}_1 and \bar{w}_2 with flip angles \mathbf{a}_1 , \mathbf{a}_2 , respectively, [Osman98]. The tagging pattern is the multiplication of the two 1-D 1-1 SPAMM tagging pattern:

$$f_{0-2D}(p) = f_0(p; \bar{w}_1, \mathbf{a}_1, \mathbf{q}_1) \cdot f_0(p; \bar{w}_2, \mathbf{a}_2, \mathbf{q}_2) \quad \text{Eq. 5.5}$$

Using Eq.5.4, Eq5.5 can be written as:

$$\begin{aligned} f_{0-2D}(p) = & \frac{1}{4} [\cos(\mathbf{a}_1 - \mathbf{a}_2) + \cos(\mathbf{a}_1 + \mathbf{a}_2)]^2 + \\ & + \frac{1}{4} [\sin(\mathbf{a}_1 - \mathbf{a}_2) + \sin(\mathbf{a}_1 + \mathbf{a}_2)]^2 \cos(\bar{w}_1^T p + \mathbf{q}_1) + \\ & + \frac{1}{4} [\sin(\mathbf{a}_2 - \mathbf{a}_1) + \sin(\mathbf{a}_1 + \mathbf{a}_2)]^2 \cos(\bar{w}_2^T p + \mathbf{q}_2) + \\ & + \frac{1}{4} [\cos(\mathbf{a}_1 - \mathbf{a}_2) + \cos(\mathbf{a}_1 + \mathbf{a}_2)]^2 \cdot \frac{1}{2} \cos[(\bar{w}_1^T - \bar{w}_2^T)p + \mathbf{q}_1 - \mathbf{q}_2] + \\ & + \frac{1}{4} [\cos(\mathbf{a}_1 - \mathbf{a}_2) + \cos(\mathbf{a}_1 + \mathbf{a}_2)]^2 \cdot \frac{1}{2} \cos[(\bar{w}_1^T + \bar{w}_2^T)p + \mathbf{q}_1 + \mathbf{q}_2] \end{aligned} \quad \text{Eq. 5.6}$$

Thus, Eq.5.6 can be also written as:

$$\begin{aligned} f_{0-2D}(p) &= \sum_{i=0}^4 D_i(p; \mathbf{a}_1, \mathbf{a}_2) \cos(\bar{w}_i^T p + \mathbf{q}_i) = \\ &= \sum_{i=0}^4 D_i(p; \mathbf{a}_1, \mathbf{a}_2) f_0(p; \bar{w}_i, 90^0, \mathbf{q}_i) \end{aligned} \quad \text{Eq. 5.7}$$

where D_i can be easily deduced from Eq.5.6, and $\bar{w}_0 = 0$, $\bar{w}_3 = \bar{w}_1 + \bar{w}_2$, $\bar{w}_4 = \bar{w}_1 - \bar{w}_2$, $\mathbf{q}_0 = 0$, $\mathbf{q}_3 = \mathbf{q}_1 + \mathbf{q}_2$ and $\mathbf{q}_4 = \mathbf{q}_1 - \mathbf{q}_2$.

Considering Eq.5.2, Eq.5.3, Eq.5.7 reveals that, apart from the fading effect, a 2-D 1-1 SPAMM image is the summation of five images, four of which are sinusoidal modulated. In the Fourier domain this results in nine spectral peaks. One single peak at DC because of the constant term of Eq.5.7, four peaks in the primary sinusoid directions and four peaks in the direction of the products of these sinusoids.

Generalised SPAMM:

Generally, because the cosine function has two spectral peaks in Fourier domain, a 1-D SPAMM pattern generated with N RF pulses has $2N-1$ spectral peaks. A 2-D SPAMM pattern is the product of two 1-D SPAMM patterns and thus it has $(2N-1)^2$ spectral peaks. Therefore any SPAMM tagged image in Fourier space can be written as, [Osman00-2]:

$$I_{TAG}(p) \approx \sum_{k=1}^K I_{orig}(p) \cdot d_k \cdot e^{j\bar{w}_k^T p} \quad \text{Eq. 5.8}$$

where $K = 2N - 1$ for 1-D SPAMM and $K = (2N - 1)^2$ for 2-D SPAMM. d_k can be easily determined from the flip angles \mathbf{a} .

CSPAMM:

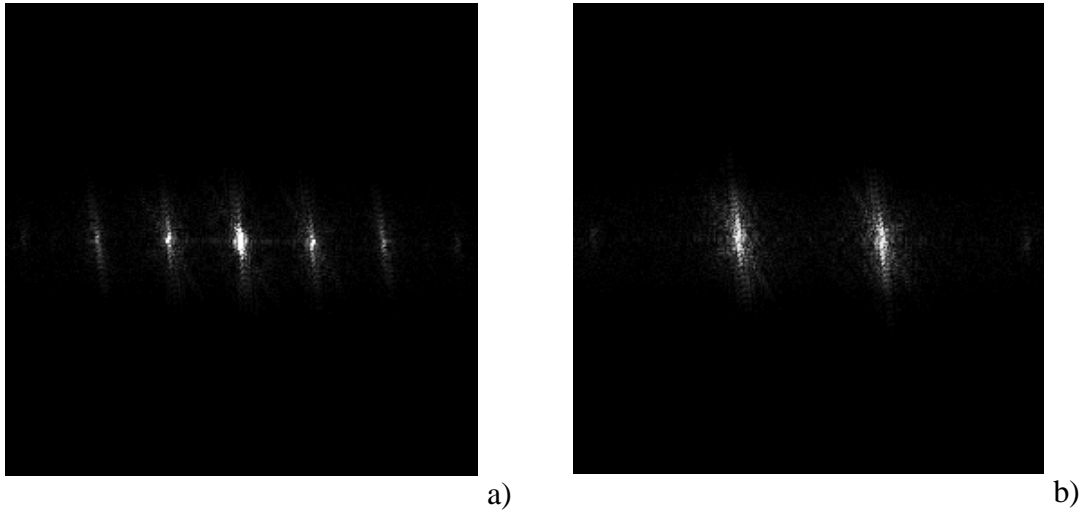


Figure 5.1: Fourier Transform – a) SPAMM spectrum, b) CSPAMM spectrum

The CSPAMM image is a subtraction of two 1-1 SPAMM images, one of which has the tag lines inverted, [Kuijer01], [Fischer93]. If we use Eq.5.3, Eq.5.4 a faded and tagged 1-1 SPAMM pattern can be written as:

$$f(\bar{y}, t) = \frac{1}{2} \left\{ [2 - 2\mathbf{b}(t)\sin^2(a)] + 2\mathbf{b}(t)\sin^2(a)\cos(\bar{w}^T p + \mathbf{q}) \right\} \quad \text{Eq. 5.9}$$

which is in full agreement with [Kuijjer01] if we set $s(t) = 2\mathbf{b}(t)\sin^2(a)$. Therefore, the CSPAMM image can be expressed as, [Kuijjer01]:

$$\begin{aligned} f_{\text{CSPAMM}}(\bar{y}, t) &= \frac{1}{2} \left\{ [2 - s(t)] + s(t)\cos(\bar{w}^T p + \mathbf{q}) \right\} - \\ &\quad \frac{1}{2} \left\{ [2 - s(t)] - s(t)\cos(\bar{w}^T p + \mathbf{q}) \right\} = \\ &= s(t)\cos(\bar{w}^T p + \mathbf{q}) \end{aligned} \quad \text{Eq. 5.10}$$

Comparing Eq.5.8 with equation Eq.5.9 we can observe that CSPAMM eliminates the DC term, Figure 5.1-b, while Eq.5.8 is better approximated from a CSPAMM tagged image, rather than a one 1-1 SPAMM tagged pattern, Figure 5.1-a. Although Figure 5.1-a is a 1-1 1-D SPAMM we observe five peaks instead of 3, Eq.5.8, because of imperfectness of RF pulses. This effect has amazingly improved in the Fourier transform of the CSPAMM image.

5.2.2 Harmonic Images

The Fourier transform of a tagged image consists of the central peak, DC component, and the harmonic peaks, as already discussed in the previous paragraph. Therefore, in the frequency domain the 2D MR image can be expressed similarly to Eq.5.8 as, [Osman00-3]:

$$I(p, t) = \sum_{k=-L}^L I_k(p, t) \quad \text{Eq. 5.11}$$

The locations of the spectral peaks in Fourier space are integer, L , multiples of the fundamental tag frequency w determined by the tagging pulse sequence. Therefore, it is easy to isolate, automatically, any one of these peaks and obtain its inverse Fourier transform, which is a complex image. We refer to the complex images corresponding to these peaks as the *DC image* and the *harmonic images*. The k -th harmonic image is given by:

$$I_k(p, t) = D_k(p, t) e^{j(k \cdot w \cdot q(p, t) + J_k)} \quad \text{Eq. 5.12}$$

where $D_k(p, t)$ is called *harmonic amplitude image* and represents the image amplitude, which reflects both the changes in geometry of the heart and the image

intensity changes caused by tag fading. $q(p, t)$ is called the *apparent reference map* and it characterises the heart motion and relates all points within an image \mathbf{p} to their reference positions. Apparent motion is analysed in the next paragraph. \mathbf{J}_k is an arbitrary phase determined by the position of application of the tag pattern. Finally, $(k \cdot w)$ is the position of the k -th harmonic peak. Eq.5.12 establishes a mathematical relationship between the harmonic image and the reference map that is the basis of HARP as once the reference map has been found the deformation of the tagging pattern is described completely.

The goal now is to estimate the *harmonic phase image*, or *angle image*, which is defined as:

$$\Phi_k(p, t) = k \cdot w \cdot q(p, t) + \mathbf{J}_k \quad \text{Eq. 5.13}$$

Unfortunately, phase unwrapping is required to determine $\Phi_k(p, t)$ from $I_k(p, t)$, which is a difficult and generally impractical procedure. Instead, we use the wrapped version of the harmonic phase image, a , which is calculated straightforwardly from the complex image using the arctangent of the ratio of the imaginary to real part:

$$a = W(\Phi) = \arctan\left(\frac{\text{imag}(I)}{\text{real}(I)}\right) \quad \text{Eq. 5.14}$$

Where, W is the wrapping function given by:

$$W(\mathbf{j}) = \text{mod}(\mathbf{j} + \mathbf{p}, 2\mathbf{p}) - \mathbf{p} \quad \text{Eq. 5.15}$$

The effect of wrapping is the essential problem in harmonic phase imaging.

5.2.3 Tagging MRI – Signal Processing Perspective

In [Bayram01] there is further investigation about the properties of spectral peaks in frequency domain. Tagging is defined as a sampling process, and thus the tagging image i_{TAG} is considered as the difference of the original image i_{orig} and its sampled version at the tag locations:

$$i_{TAG}(p, t) = i_{orig}(p, t) - i_{orig}(p, t) \cdot f(p, t) \quad \text{Eq. 5.16}$$

p expresses every point on (x, y) plane of the MR image and $f(p)$ is the tagging function defined by Eq.4.2. The spatial dimensions x, y must satisfy $0 \leq x, y \leq N - 1$.

From a signal processing perspective $f(p)$ can be also written as the sum of shah functions, \mathbf{d} :

$$f(p, t) = f(x, y, t) = \sum_{n=0}^{\frac{N}{T(t)}} \mathbf{d}(y - nT(t)) \quad \text{Eq. 5.17}$$

$T(t)$ is the tag separation, defined as a function of time because its value changes during the deformation of the tag pattern.

Now Eq.5.16 in the spatial domain can be written as:

$$I_{TAG}(\mathbf{u}, u, t) = I_{orig}(\mathbf{u}, u, t) - \frac{1}{N} I_{orig}(\mathbf{u}, u, t) \otimes_N f(\mathbf{u}, u, t) \quad \text{Eq. 5.18}$$

Where \otimes_N is the circular convolution operator with period N and $0 \leq \mathbf{u}, u \leq N - 1$.

According to [Bayram01], Eq.5.18 can be written as:

$$I_{TAG}(\mathbf{u}, u, t) = I_{orig}(\mathbf{u}, u, t) - \frac{T(t)}{N} \sum_{k=0}^{\frac{N}{T(t)}} I_{orig}\left(\mathbf{u}, u - k \frac{N}{T(t)}\right) \quad \text{Eq. 5.19}$$

Eq.5.19 reveals that the Fourier spectrum of the tagged image has replications of the untagged image Fourier spectrum separated by $\frac{N}{T(t)}$ pixels from each other. In fact,

the Fourier transform of tagged images consists of a collection of distinct spectral peaks, whose locations are determined by the spatial frequency of the tagged pattern,

$w = \frac{N}{T(t)}$. The central peak is the *DC component* while the rest are called *harmonic spectral peaks*.

Harmonic spectral peaks on each side of the DC component are anti-symmetric and thus only one of the first spectral peaks is selected by band-pass filtering to eliminate phase cancellation. In practice, the bandwidth of the filter must be chosen carefully to minimize the influence of other spectral peaks and maximize the contribution of the desired peak. The goal is to find $T(t)$ and thus the tagging function $f(x, y, t)$ and extract the tag deformation.

5.2.4 Filtering of Spectral Peak

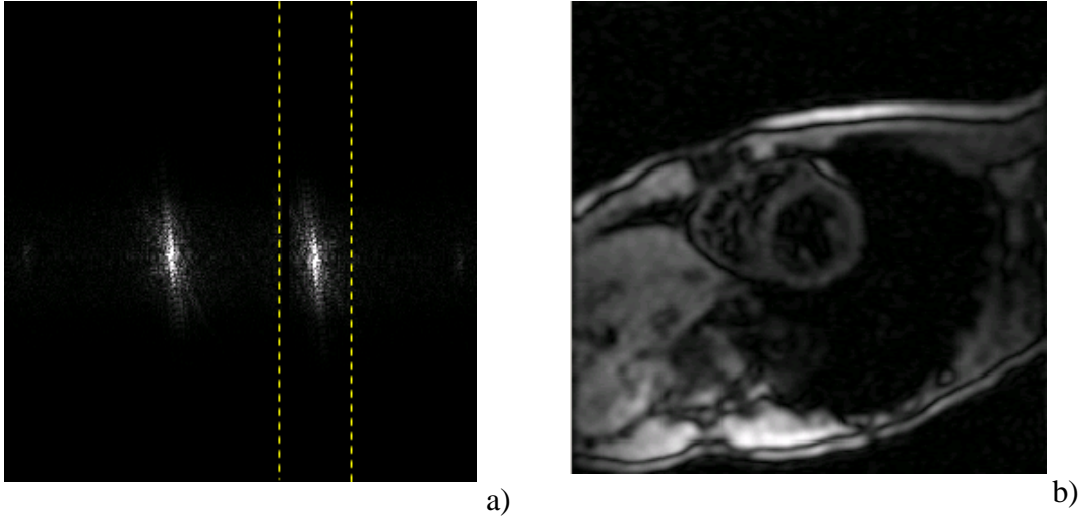


Figure 5.2: Spectral Peak Filtering – a) Fourier domain of CSPAMM and filter, b) Corresponding Harmonic Image

Filtering the harmonic peak from the Fourier transform of the tagged image is important as it affects the accuracy of the estimated motion, [Osman00-1]. The value of a harmonic peak is given by Eq.5.12 and is a complex value. The magnitude of the harmonic image looks similar to the MR image obtained without tagging, Figure 5.2-b, [Osman00-1], [Osman99]. [Osman00-1] investigates the position and the size of the spectral peaks. The size of the l -th spectral peak can be determined by computing a covariance matrix $\Sigma_l(t)$ of the power spectrum distribution. It turns out that:

$$\Sigma_l(t) = \Sigma_{D_l}(t) + \Sigma_{j_l}(t) \quad \text{Eq. 5.20}$$

where $\Sigma_{D_l}(t)$ reflects the size of the spectrum of D_l and $\Sigma_{j_l}(t)$ depends both on the motion inside the wall tissue and on the frequency w_l , Eq.5.12. Indeed, the increase in strain increases the size of the spectral peak and thus it is better to design a filter based on the largest size. However, the error also degrades with a larger filter size. The most harmful effects are when the spectral peak interferes with the DC peak, but there is also a non-negligible error when the spectral peak is not isolated from its higher frequency neighbours. In [Osman00-1] it is observed that the minimal error achievable is proportional to the tag period, which is attributed to the shift of the spectral peaks away from the DC harmonic at the higher frequency.

5.2.5 Apparent motion

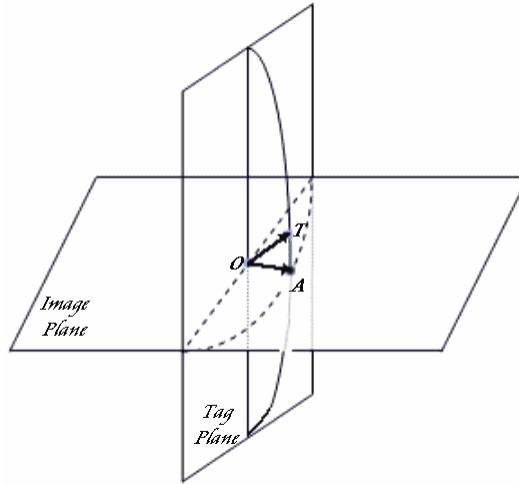


Figure 5.3: Apparent Motion

Extracting tissue deformation from tagging MRI provides information for 2D *apparent motion*, although that the true motion is three dimensional. In fact we visualise the projection of the 3D motion onto the 2D plane of the MR image, [Osman99]. This would be better understood considering a given material point O , which is on the image plane Figure 5.3 at end diastole. After time t its true position is T , while the tagging image has recorded its apparent position A . Indeed, a tag line appearing in an image plane at end-diastole is actually part of a tag plane that is orthogonal to the image plane. The tag plane distorts under motion causing this line to distort into a curve. This curve will still intersect the image at a single point A . This point can be uniquely associated with the corresponding point at end-diastole representing an *apparent motion* within the image plane, [Osman99].

Mathematically, apparent motion can be described using an *apparent reference map*, denoted as $q(p)$, [Kerwin00]:

$$q(p) = \bar{H}^T (p - \bar{x}_0) \quad \text{Eq. 5.21}$$

which is the projection of any material point from its reference position onto the image plane. Therefore, a 2D correspondence has been defined between any image position \bar{y} and its 2D apparent position $q(p(\bar{y}, t))$. This leads us to obtain a complete set of 2D apparent motion equations. Although, calculating the apparent 2D motion is a certain limitation, there is a very precise relationship between the apparent reference map $q(p)$ and the true reference map. $q(p)$ is the orthogonal projection of the true

3D material point location onto the image plane. Generally, the apparent motion may not be closely related to the true motion. However, in the cardiac setting there is a good correlation between apparent strain and true strain, [Kerwin00].

5.3 HARP MRI – Calculating velocity fields

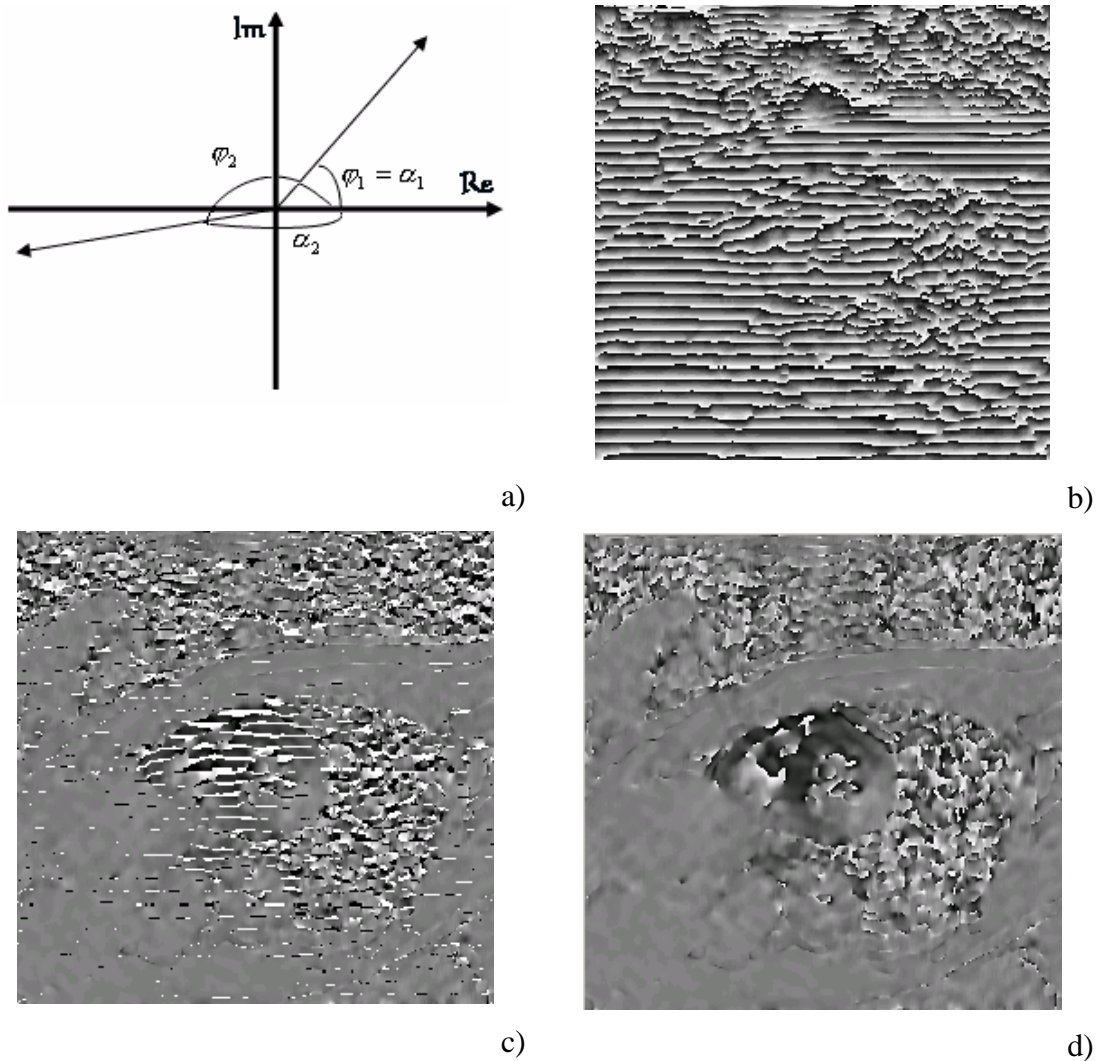


Figure 5.4: Wrapping effects – a) Relationship between the subtraction of wrapped and unwrapped images, b) Wrapped angle of Harmonic Image, c) Subtraction of two angle images of successive frames, d) Unwrapping the subtraction of the two angle images

Using HARP MRI to calculate velocity fields takes advantage of the fact that the harmonic phase of a material point remains constant as it moves, [Osman00]:

$$\frac{d\Phi(\bar{y}, t)}{dt} = 0 \quad \text{Eq. 5.22}$$

Eq.5.22 can be rewritten according the chain rule, which states that:

$$\text{If } z = f(x, y) \text{ and } x = g(t) \text{ then } \frac{dz}{dt} = \frac{\partial z}{\partial x} \frac{dx}{dt} + \frac{\partial z}{\partial y} \frac{dy}{dt} \quad \text{Eq. 5.23}$$

Therefore, from Eq.5.22 if we assume that $z = \Phi(\bar{y}, t)$ and $x = t$ then:

$$\frac{\partial \Phi(\bar{y}, t)}{\partial \bar{y}} \frac{d\bar{y}}{dt} + \frac{\partial \Phi(\bar{y}, t)}{\partial t} \frac{dt}{dt} = 0 \quad \text{Eq. 5.24}$$

According to Eq.5.24 velocity fields are expressed in terms of the harmonic phase image $\Phi(\bar{y}, t)$:

$$u(\bar{y}, t) = - \left[\frac{\partial \Phi(\bar{y}, t)}{\partial \bar{y}} \right]^{-1} \frac{\partial \Phi(\bar{y}, t)}{\partial t} \quad \text{Eq. 5.25}$$

Calculating $\Phi(\bar{y}, t)$ from the harmonic image is difficult because it requires phase unwrapping that is an impractical and very sensitive to noise process. Phase unwrapping is considered particularly problematic in the high-noise environment of cardiac MRI, [Osman00]. Instead, the wrapped version of phase is available, $a(\bar{y}, t)$, which falls into the range $[-\mathbf{p}, \mathbf{p}]$ because of the arctan operator: $a(\bar{y}, t) = \tan^{-1} \left(\frac{\text{Im}}{\text{Re}} \right)$, where Im, Re are the imaginary and real part, respectively, of harmonic image. The wrapping function $W(\cdot)$ is a non-univocal mapping between the real phase, $\Phi(\bar{y}, t)$ and its wrapped version.

$$a(\bar{y}, t) = W(\Phi(\bar{y}, t)) = \text{mod}(\Phi(\bar{y}, t) + \mathbf{p}, 2\mathbf{p}) - \mathbf{p} \quad \text{Eq. 5.26}$$

In the case that the time interval, Δt , between two successive frames is sufficiently small the difference of the phases corresponding to these frames can be assumed to be into the range of $[-\mathbf{p}, \mathbf{p}]$:

$$\left| \Phi(\bar{y}, t_{n+1}) - \Phi(\bar{y}, t_n) \right| < \mathbf{p} \quad \text{Eq. 5.27}$$

Therefore, the partial time derivative of the phase is approximately equal to the wrapped difference of the wrapped phase. This can be better understood considering Figure 5.4-a, where the real phase difference is $(2k\mathbf{p} + \mathbf{j}_2) - (2k\mathbf{p} + \mathbf{j}_1) = \mathbf{j}_2 - \mathbf{j}_1$. We have instead $\mathbf{a}_2 - \mathbf{a}_1$, Figure 5.4-c. The wrapping function $W(\mathbf{j})$ maps the difference of the wrapped phases $\Delta \mathbf{a}$ to the real $\Delta \mathbf{j}$, Figure 5.4-d.

$$\frac{\partial \Phi}{\partial t}(y, t_n) \approx \frac{1}{\Delta t} W[a(y, t_{n+1}) - a(y, t_n)] \quad \text{Eq. 5.28}$$

Finally, the partial spatial derivative of phase Φ is the same as the partial spatial derivative of a apart from the points of discontinuities of a , Figure 5.4-b:

$$\nabla \Phi = \nabla^* a = \begin{bmatrix} \nabla^* a_h \\ \nabla^* a_v \end{bmatrix} \quad \text{Eq. 5.29}$$

Where a_h, a_v are the unwrapped phase of the horizontal and vertical tags respectively.

$$\nabla^* a = \begin{cases} \nabla a & \|\nabla a\| \leq \|\nabla W(a + \mathbf{p})\| \\ \nabla W(a + \mathbf{p}) & \text{otherwise} \end{cases} \quad \text{Eq. 5.30}$$

Therefore, from Eq.5.28 – Eq.5.30, Eq.5.25 can be written as:

$$u(y, t_n) = -\frac{1}{\Delta t} \nabla^* a^{-1}(y, t_{n+1}) W[a(y, t_{n+1}) - a(y, t_n)] \quad \text{Eq. 5.31}$$

From Eq.5.31 is clear that velocity fields can be, rapidly, computed between two successive time instances using the respective harmonic images.

5.4 HARP MRI – Calculating strain fields

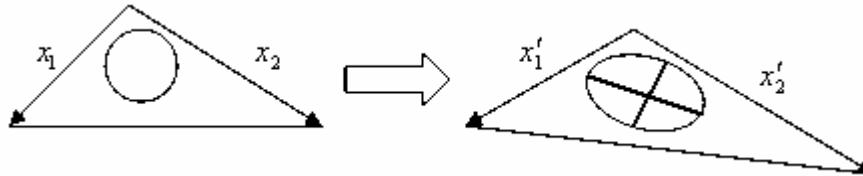


Figure 5.5: Strain eigenvectors and eigenvalues – The circle is transformed to ellipse by homogeneous motion

As it has been already mentioned (Paragraph 3.2) the concept of strain implies a measure of length change. This change can be measured either relative to the initial length, *Lagrangian Strain* or by integrating the amount of deformation during infinitesimally small time intervals, *Eulerian Strain*. Strain can be decomposed into the principal strains or (orthogonal) eigenvectors. This can be better understood if we consider the following example. A hypothetical unit circle in the initial state of the heart will be deformed into an ellipse in subsequent states. The orientation of the major and minor axes of the ellipse corresponds to the directions of the eigenvectors of the transformation and their lengths are the eigenvalues, Figure 5.5, [Axe192].

Under the perception of HARP MRI, strain can be calculated using a single frame, with reference to the initial position of the tags, [Osman98-1], [Kuijjer01]. Therefore, the deformation gradient tensor is given by the Eq.5.32:

$$F = k_1 (\nabla^* a)^{-1} \quad \text{Eq. 5.32}$$

where k_1 is the initial tag frequency, under the condition that is the same for both horizontal and vertical tags, and $\nabla^* a$ is defined by the previous paragraph, Eq.5.30.

However, two-dimensional strain parameters cannot be calculated directly from Eq.5.32 because the gradient tensor E is composed from both the rigid body rotation R and the stretch U , Eq.5.33. Decomposition is needed in order to isolate the deformation tensor U , which is independent of the rigid motion, and obtain the principal eigenvectors and eigenvalues of Eulerian strain.

$$E = RU \quad \text{Eq. 5.33}$$

Therefore, the gradient tensor E can be written as:

$$E = \begin{bmatrix} a & b \\ c & d \end{bmatrix} = \underbrace{\begin{bmatrix} \cos(\mathbf{q}) & \sin(\mathbf{q}) \\ -\sin(\mathbf{q}) & \cos(\mathbf{q}) \end{bmatrix}}_R \cdot \underbrace{\begin{bmatrix} t_x & t_{xy} \\ t_{yx} & t_y \end{bmatrix}}_U \quad \text{Eq. 5.34}$$

The strain tensor, E , (Eq.3.6) is related to deformation tensor by the equation:

$$F = U - I = \begin{bmatrix} t_x - 1 & t_{xy} \\ t_{yx} & t_y - 1 \end{bmatrix} \quad \text{Eq. 5.35}$$

5.5 Discussion

The main advantage of *HARP MRI* over conventional tagged MR analysis techniques is its rapid processing time compared with minimal manual assessment, and thus it has the potential for on-line quantitative monitoring of LV function [Garot00]. The principal idea is that the amplitude of a tagging pattern decreases at later times while the amplitude of the phase of the tagging pattern is unaffected. The motion is reflected on the increase of the slope of the phase of the tagging pattern, *local frequency*.

HARP has also been validated by [Garot00] in terms of accuracy. The investigation confirms that HARP imaging can be established as a clinical tool. The results were satisfactorily convincing. HARP imaging was an order of magnitude faster than tagging. The experiment was based on the ten volunteers who supplied with

dobutamine for a stress test. HARP accurately detected subtle changes in myocardial strain fields under increasing doses. Measurements of 2D myocardial strains by HARP are reproducible and similar to those obtained by a conventional tag motion tracking technique, both in patients with coronary artery disease (CAD) with wall motion abnormalities and in normal volunteers at rest and during inotropic stimulation. However, a certain current limitation of the technique is that it applies only to 2D images. HARP has the potential to extend to 3D but with the current scanning methods, 3D image acquisition is prohibitively long for cardiac applications. Thus the motion measured by HARP is not the true but the ‘*apparent*’ motion. Although, calculation of apparent 2D motion has its limitations it is efficient enough to apply in cardiac imaging.

5.6 References and Bibliography

- [Osman98-1] N.F. Osman and J.L. Prince, ‘Direct calculation of 2D components of myocardial strain using sinusoidal MR tagging’, to appear in Proc. of the SPIE Medical Imaging:Image Processing Conference, 1998, San Diego, California
- [Osman98-2] N.F. Osman and J.L. Prince, ‘Angle Images for Measuring Heart Motion from Tagged MRI’, to be published in the Proceedings of ICIP98, Chicago IL, Oct. 4--7, 1998
- [Osman99] Nael F Osman, William S. Kerwin, Elliot R. McVeigh and Jerry L Prince, ‘Cardiac motion tracking using CINE harmonic phase (HARP) magnetic resonance imaging’, *Magnetic Resonance in Medicine*, 42(6):1048-60, 1999 Dec
- [Osman00-1] Nael F Osman and J.L. Prince, ‘On the Design of the Bandpass Filters in Harmonic Phase MRI,’ Proc. IEEE Int’l Conf. Image Proc., Vancouver, Sept. 10-20, 2000
- [Osman00-2] Nael F. Osman, Elliot R. McVeigh and Jerry L.Prince, ‘Imaging Heart Motion Using Harmonic Phase MRI’, *IEEE Transactions of Medical Imaging*, vol. 19, no 3, March 2000
- [Osman00-3] Nael F Osman and Jerry L Prince, ‘Visualization myocardial function using HARP MRI’, *Phys Med Biol.*, 45(6):1665-82, 2000 Jun

- [Garot00] Jerome Garot, David A. Bluemke, Nael F. Osman, Carlos E. Rochitte, Elliot R. McVeigh, Elias A. Zerhouni, Jerry L Prince, Joao A.C. Lima, 'Fast determination of regional myocardial strain fields from tagged cardiac images using harmonic phase MRI', *Circulation*, 101(9):981-8, 2000 Mar 7
- [Kerwin00] W.S. Kerwin, N.F. Osman, and J.L. Prince, 'Image processing and analysis in tagged cardiac MRI', Chapter 24, *Handbook of Medical Image Processing*, I Bankman, Editor, Academic Press, 2000
- [Osman01] Osman NF, Sampath S, Atalar E, Prince JL, 'Imaging longitudinal cardiac strain on short-axis images using strain-encoded MRI', *Magnetic Resonance in Medicine*, 46(2):324-34, 2001 Aug
- [Kuijjer01] Kuijjer JP, Jansen E, Marcus JT, van Rossum AC, Heethaar RM, 'Improved harmonic phase myocardial strain maps', *Magnetic Resonance in Medicine*, 46(5):993-9, 2001 Nov
- [Bayram01] Ersin Bayram, Craig A. Hamilton and W. Gregory Hundley, 'MR Tagging From A Signal Processing Perspective', *IEEE EMBS 23 Annual Conference*, October 2001

Chapter 6 – Vector Fields Restoration

6.1 Introduction

Visualizing vector fields that represent either velocity or strain is a challenging problem. Displaying x and y component separately as colour-maps provides useful information of the general function of the myocardium, (Paragraph 1.7) and it is relatively simple. However, appropriate visualization of the regional function of ventricular muscle requires techniques that combine both the x and y component at each point of the 2D or 3D image. Clinicians need this information in order to perceive regional diminished myocardial contractility and diagnose ischemic disease and subsequently infarction, (Paragraph 1.7). In this work vector fields are demonstrated by plotting lines with length proportional to the magnitude of the vector. Generally, strain maps and velocity fields formed under the principles of HARP MRI are susceptible to noise as they are produced as a result of differentiation. Visualization of that vector fields is a process sensitive to noise and thus special techniques should be applied to alleviate this effect. In this chapter, it is represented a method of de-noising and restoring the direction of vector fields produced either from strain or velocity data. Moreover, it has been especially considered how to apply this method computationally efficiently.

6.2 Vector Fields Restoration

De-noising and restoration of the velocity fields has significant impact on the quality of the estimated displacement fields. Therefore, in our case the goal is to restore the orientation of velocity fields that have been estimated between two successive *MRI* acquisitions using the principles of *HARP* images. The technique used here for vector restoration is based on [Chan99], where the mathematical/theoretical model is established and analysed. According [Chan99], the orientation feature is a non-flat feature, non-Euclidean, that lives on the unit cycle S^1 and thus, is fully described by the angle \mathbf{J} . Moreover, it provides a systematic way for constructing the energy function, which is an extension of the classical *total variational (TV) model*.

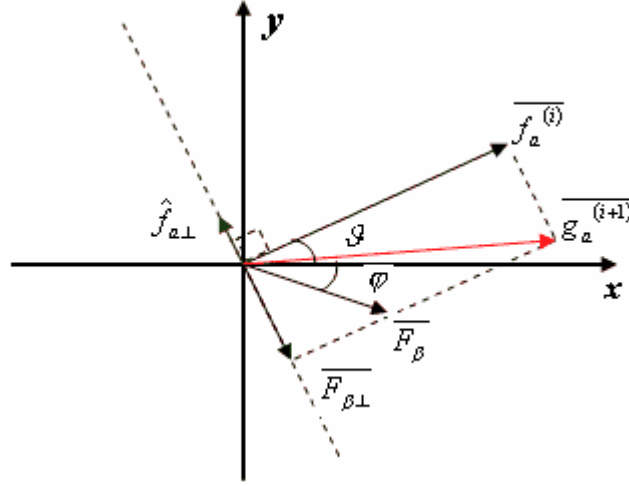


Figure 6.1: Vector Fields Restoration

[Coulon01] applies the restoration of orientation features to the discrete case. The TV fitted energy is described as:

$$\mathbf{e}^{TV}(f; \mathbf{l}) = \sum_{\mathbf{a} \in \Omega_n} e(f; \mathbf{a}) + \mathbf{l} \sum_{\mathbf{a} \in \Omega_n} \frac{1}{2} d_l^2(f_a^{(0)}, f_a) \quad \text{Eq. 6.1}$$

where d_l is the Euclidean distance, $f^{(0)}$ is the original image feature, f_a is the direction at voxel \mathbf{a} and $e(f; \mathbf{a})$ is the strength function at voxel \mathbf{a} . The strength function is a measure of smoothness of the direction map and is defined as:

$$e(f; \mathbf{a}) = \left[\sum_{\mathbf{b} \in N_a} d_l^2(f_b, f_a) \right]^{\frac{1}{2}} \quad \text{Eq. 6.2}$$

where N_a is a neighbourhood of \mathbf{a} . For a typical internal cross node $\mathbf{a} = (i, j)$ in image processing its neighbours are $\mathbf{b} = (i, j-1), (i, j+1), (i-1, j), (i+1, j)$. Minimisation of Eq.6.1 is described by a partial differential equation, which leads to the above relatively simple iterative scheme:

$$\overline{g_a^{n+1}} = \overline{f_a^n} + \Delta t \cdot \prod_{f_a} \left(\sum_{\mathbf{b} \in N_a} w_a^b \overline{f_b} + \mathbf{l} \overline{f_a^{(0)}} \right) \quad \text{Eq. 6.3}$$

$$\overline{f_a^{n+1}} = \frac{\overline{g_a^{n+1}}}{\left\| \overline{g_a^{n+1}} \right\|} \quad \text{Eq. 6.4}$$

where $\overline{f_a^{(i)}}$ the orientation feature, Figure 6.1, parameterised by the angle \mathbf{J} and the direction feature $\overline{f_a}$ is restored using its neighbours $\overline{f_b}$, where $\mathbf{b} \in N_a$. It is obvious that the restoration takes place only for the direction of vector fields while their lengths remain the same.

In order to apply Eq.6.3 – Eq.6.4 using a computational efficient way Figure 6.1 is considered, where

$$\overline{F_b} = \sum_{\mathbf{b} \in N_a} w_a^{\mathbf{b}} \overline{f_b} + \mathbf{I} \overline{f_a^{(0)}} \quad \text{and} \quad \overline{F_{b\perp}} = \prod_{f_a} \overline{F_b} \quad \text{Eq. 6.5}$$

The indexes x and y denotes the x and y components of vector fields, respectively. In this section the goal is to represent the analytical expression that connects the x and y components of the resultant vector $\overline{g_a}$ to the x and y components of the $\overline{f_a}$ and $\overline{f_b}$ features, with the most simple, straightforward and computationally efficient way.

Towards this objective angles \mathbf{J} , \mathbf{j} can be defined, univocally, by Euclidean geometry as:

$$\cos(\mathbf{J}) = \frac{\overline{f_{ax}}}{\|\overline{f_a}\|} \quad \text{and} \quad \sin(\mathbf{J}) = \frac{\overline{f_{ay}}}{\|\overline{f_a}\|} \quad \text{Eq. 6.6}$$

Similarly,

$$\cos(\mathbf{j}) = \frac{\overline{F_{bx}}}{\|\overline{F_b}\|} \quad \text{and} \quad \sin(\mathbf{j}) = \frac{\overline{F_{by}}}{\|\overline{F_b}\|} \quad \text{Eq. 6.7}$$

Furthermore, it stands that $\hat{f}_{a\perp} \perp \overline{f_a}$ and $\|\hat{f}_{a\perp}\| = 1$, therefore:

$$f_{a\perp x} = \cos(90 + \mathbf{J}) \|\hat{f}_{a\perp}\| = -\sin(\mathbf{J}) \quad \text{Eq. 6.8}$$

$$f_{a\perp y} = \sin(90 + \mathbf{J}) \|\hat{f}_{a\perp}\| = \cos(\mathbf{J}) \quad \text{Eq. 6.9}$$

However, $\hat{f}_{a\perp}$ is not always the required vector, Figure 6.1. In order to check whether we should use $\hat{f}_{a\perp}$ or the unit vector at the opposite direction, $-\hat{f}_{a\perp}$, we use the above condition, Eq.6.10, that applies in any possible orientation of $\overline{f_a}$ and $\overline{f_b}$ features :

$$\cos(\mathbf{J} + 90 - \mathbf{j}) > 0 \quad \text{Eq. 6.10}$$

Finally

$$\overline{F_{b\perp}} = \|\overline{F_b}\| \cdot \|\hat{f}_{a\perp}\| \cdot |\cos(\mathbf{J} + 90 - \mathbf{j})| \cdot \hat{f}_{a\perp} \quad \text{Eq. 6.11}$$

where $\cos(\mathbf{J} + 90 - \mathbf{j}) = \sin(\mathbf{j} - \mathbf{J}) = \sin(\mathbf{j})\cos(\mathbf{J}) - \cos(\mathbf{j})\sin(\mathbf{J})$. Therefore, using the Eq.6.5 – Eq.6.11 we can derive that:

$$\overline{F_{b\perp}} = \left| \frac{F_{b_y} f_{ax} - F_{b_x} f_{ay}}{\|\hat{f}_a^{(i)}\|} \right| \cdot \hat{f}_{a\perp} \quad \text{Eq. 6.12}$$

Based on Eq.6.12 restored velocities fields are calculated within some seconds even for a large number of iterations.

6.3 Discussion

The use of vector de-noising and restoration are not limited to displaying purposes. It can also have significant impact in the effectiveness of 2D or 3D tracking techniques, which calculate deformation from velocity data, [Kuijjer99], [Masood02]. These techniques are susceptible to accumulative errors and thus they are very sensitive to noise. In summary, an analytical expression has been extracted easily from the geometry of Figure 6.1 for straightforward and efficient application of the algorithm. This was applied to both patient and normal data and some results are described in Chapter 7.

6.4 References and Bibliography

- [Chan00] Tony Chan and Jianhong Shen, ‘Variational Restoration of Non-Flat Image Features: Models and Algorithms’, SIAM Journal on Applied Mathematics, 2000
- [Coulon01] O. Coulon, D.C. Alexander and S.R.Arridge, ‘Tensor Field Regularisation for DT-MR Images’, Proc. MIUA'01, Medical Image Understanding and Analysis, Birmingham, UK, 2001
- [Masood02] S. Masood, J.X. Gao, D.N. Firmin and G.Z. Yang, ‘Virtual Tagging: numerical considerations and phantom validation’, IEEE in Transaction on Medical Imaging, submitted 2002
- [Kuijjer99] Joost P.A. Kuijjer, J. Tim Marcus, Marco J.W. Gotte, Albert C. van Rossum and Robert M. Heethaar, ‘Simultaneous MRI Tagging and

Through-Plane Velocity Quantification: A Three-Dimensional Myocardial Motion Tracking Algorithm', *Journal of Magnetic Resonance Imaging* 9:409-419, 1999

Chapter 7 – Experiment Setup and Results

7.1 Introduction

In this study, the HARP MRI technique is adapted in order to calculate *velocity fields* and *strain maps* through out the cardiac cycle. The implications of HARP principles are investigated step by step and decisions are taken for the various parameters affecting the quality and accuracy of the results. Based on the acquisitions of CSPAMM tagged images (Paragraph 4.4) and the effectiveness of HARP (Chapter 5), deformation tensors (Paragraph 3.2) and velocity information are calculated within some seconds. Finally, vector de-noising and restoration, (Chapter 6) is applied to eliminate noise effect and improve the effectiveness of the current study in terms of early diagnosis and prevention of certain cardiovascular diseases, (Chapter 1). Results are compared between volunteers and patient data in order to validate the potential of this technique in *in-vivo* monitoring in a clinical environment. In terms of this project, a useful and flexible research tool was developed to visualise both anatomical, MR scanned images, and functional information, velocity fields, (Chapter 2), which is analytically described in the appendix.

7.2 Overview

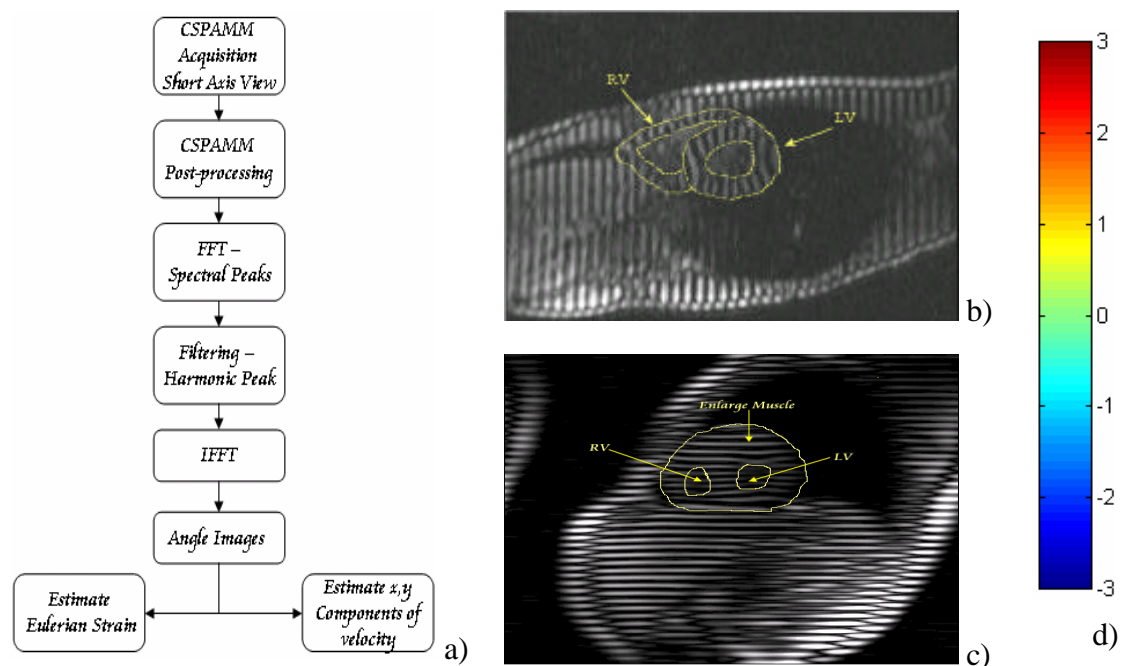


Figure 7.1: a) Overview, b) Short axis View of normal data, c) Short axis View of patient data, d) Colour-map used

A basic overview of the application is illustrated in Figure 7.1-a. Images were acquired in a normal volunteer, Figure 7.1-b, and a patient with HCM, Figure 7.1-c, (Paragraph 1.7.4). This part describes step by step the processing of the data in order to obtain HARP images and subsequently velocity fields and strain maps. Each step of the process is presented as a separate paragraph and the results are illustrated in greyscale figures or in 256 RGB colour-maps that are scaled from -3 to 3, Figure 7.1-d, unless others scaling values are indicated. The normal volunteer data is used through out this chapter, while in the end are compared to the respective patient data.

During scanning eight images are acquired for each frame, which correspond to vertical-horizontal tags, CSPAMM acquisition, and phase and magnitude format or raw data. The processing of horizontal and vertical tags is similar, apart from registration problems, while the images acquired should be processed in order to get CSPAMM. The basic steps towards the fulfilment of the experimental part of this study can be summarised as:

- The acquisition process has significant impact on the final results in terms of noise and motion artifacts. Its parameters are a trade-off between image resolution and scanning time, which is limited because of respiratory motion and artifacts introduced by patient movements.
- From k-space the magnitude and the phase of each complementary tagging grid should be processed in order to be expressed in a uniform and consistent way. The corresponding complex images are formed by the raw data. In case of horizontal tags, the complex image should be reflected and transposed, because of the way the image acquisition and reconstruction is done. Normally, reflection does not apply to vertical tags. Moreover, mis-registration between horizontal and vertical tags occurs as a consequence of the difference in frequency and phase encoding directions and specifications of the scanning hardware.
- Once the proper images have been obtained they are subtracted according to the principals of CSPAMM, (Paragraph 4.4).
- The CSPAMM image is transformed to the Fourier domain. The spectral peaks that are produced are the basis of HARP, (Paragraph 5.2.2). The tagging information is sited in one of the harmonic peaks, while the DC component is undesirable as it

adds noise and is partially responsible for the tagging fading. Thus, a band-pass filter is used to isolate the harmonic peak. Afterwards, the inverse Fourier transform of the image is obtained, which is a complex image.

- Calculating velocity fields based on Eq.5.31 is the next step. Velocity fields are derived rapidly and displayed using colour-maps for x and y component and vectors for further investigation.
- Strain is calculated under similar conditions. Here the interest is focused on displaying the principal eigenvector and eigenvalue that indicates regional myocardial deformation, (Paragraph 5.4).
- Finally, vector de-noising and restoration is successfully applied to enhance vector fields. Furthermore, a mask is applied in order to separate the myocardial wall from both the inside blood pool and outside noisy environment.

7.3 Scanning Sequence and Various Parameters

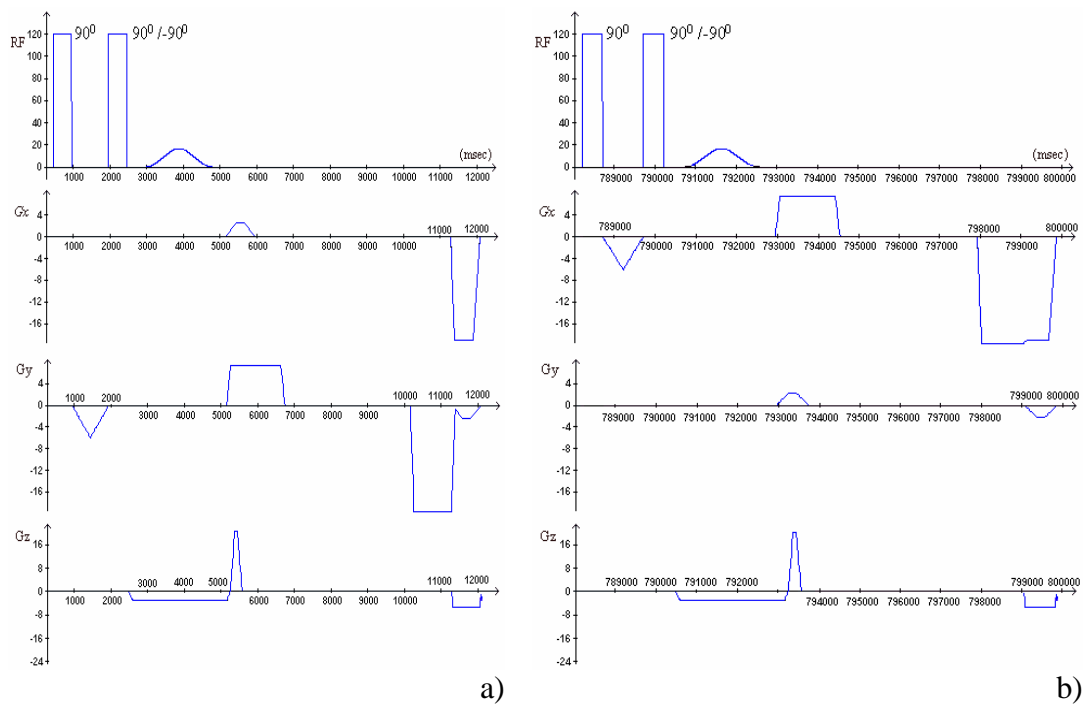


Figure 7.2: Scanning Sequence a) Horizontal Tags, b) Vertical Tags

Images were acquired in a normal volunteer with FOV 300mm by 300mm, short axis view Figure 7.1-b, while the FOV for patient data was 317mm by 340 mm, short axis

view, Figure 7.1-c. The image resolution is 32 in the phase encoding direction and 256 in the frequency encoding direction, while the rest of 256 by 256 (240 by 240 - HCM) images are filled with zeros. In addition slice thickness and tag spacing is 8mm. Finally, the number of time frames was 16 for normal volunteer data and 12 for patient with HCM.

In Figure 7.2 is, analytically, presented the pulses sequence used for this experiment. RF pulses are based on a typical CSPAMM sequence (Paragraph 4.4), therefore the pulses of Figure 7.2 are repeated twice, initially using 90^0 , 90^0 and then 90^0 , -90^0 degree pulses. Using the sequence of Figure 7.2-a horizontal tags are created while in Figure 7.2-b is represented the sequence for vertical tags. G_x , G_y and G_z are the three gradients along the three main axes (X, Y, Z) , which are responsible for the frequency encoding, phase encoding and slice selection, respectively, (Paragraph 2.5.2). Short axis slices have been acquired in a single breath hold in order to eliminate artifacts caused by respiratory motion and arbitrary movements of the subject, (Paragraph 2.5.3).

The scanning sequence consists of four separate time phases.

- Tagging: Tagging effect is created, during the two first RF pulses of 90^0 and $90^0 / -90^0$, either using G_y for vertical tags or G_x for horizontal tags.
- Slice selection: While the third RF pulse applies the G_z gradient is switched on to accomplish slice selection.
- Frequency and Phase encoding: Subsequently, G_x and G_y are used for frequency and phase encoding. Data is acquired during this time.
- De-phasing of longitudinal magnetization.

7.4 From raw data to HARP Images

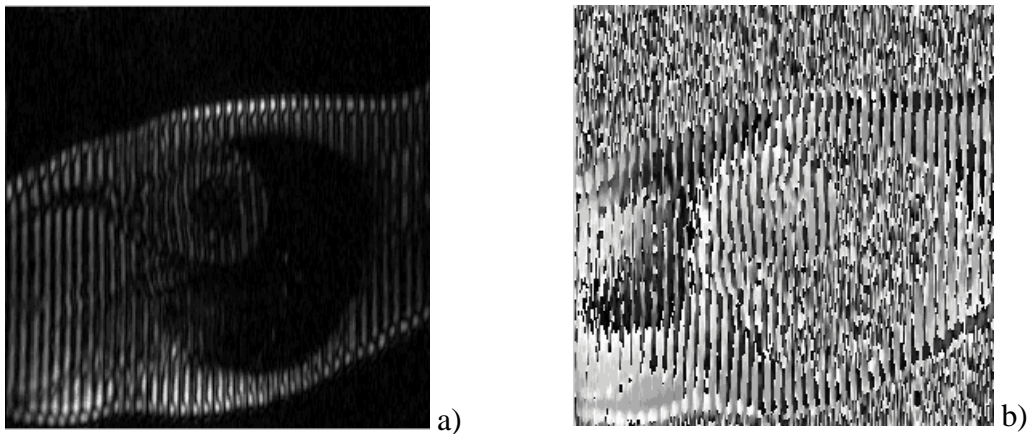


Figure 7.3: Raw data a) Magnitude image, b) Phase image

K-space data (Paragraph 2.5.2) are gathered and reconstructed to time domain automatically from the scanning system into files with complex header format, while image data are stored at the end of the file with precision of two bytes. There are separate files for magnitude and phase data, Figure 7.3 that are systematically and regularly stored in the disc in order to be able to retrieve their path easily.

7.4.1 Reconstruction of Complex Images

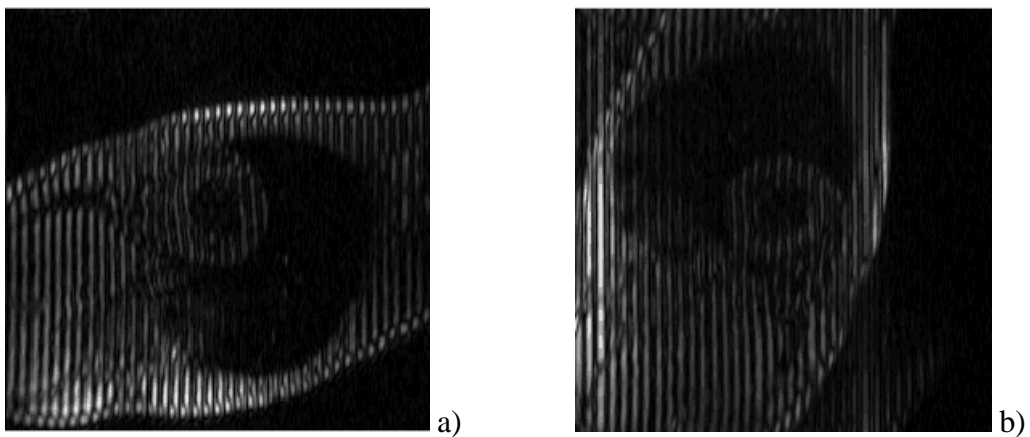


Figure 7.4: Geometrical inconveniences a) Vertical Tags, b) Horizontal Tags

Special consideration is needed to combine horizontal and vertical tags data, Figure 7.4. Horizontal tags are reflected and transposed because of the way the images have been acquired from the scanning system. Assuming that an image forms a matrix of I rows and J columns the (i,j) element of the reflected image corresponds to the $(I-i, J-j)$ element of the initial. Similarly, transposing an image requires assignment of the (i,j)

to the (j,i) element. Mis-registration problems should be also solved before processing, otherwise the results are unpredictable. Complex data are reconstructed from raw images Figure 7.3 by transforming the phase, which is within the range of -4096 to 4096 , corresponding to the range of 0 to $2p$.

7.4.2 Reconstruction of CSPAMM – Fourier Domain

CSPAMM images are reconstructed by subtracting the correspondence SPAMM images received with RF inverted pulse, (Paragraph 4.4). Tags are better resolved during the last frames of the cardiac cycle as compared to the corresponding SPAMM images, (Paragraph 4.3). In Figure 7.9-a-c-e is illustrated a series of CSPAMM images, magnitudes and phases, while in Figure 7.10-b-d-f are the corresponding SPAMM images, in order to compare fading effects.

Fourier Domain is an alternative way to appreciate the effectiveness of CSPAMM in terms of HARP MR images. In Figure 7.10 there are the corresponding SPAMM and CSPAMM spectrum for the same frames as Figure 7.9. Obviously, CSPAMM images are more appropriate for spectral peak filtering as the central peak has entirely disappeared through out the cardiac cycle, while in case of SPAMM it increases considerably during the last time frames.

7.4.3 Band-pass Filter – Harmonic Images

The process of filtering has significant impact on the quality of the resulting images in terms of accuracy and signal to noise ratio, (Paragraph 5.2.4), for both strain maps and velocity fields. The inverted Fourier Transform of the filtered peak is called the Harmonic image, (Paragraph 5.2.2). Over-filtering results in loss of information, Figure 7.11-c-d, while under-filtering causes apparent tagging effects on the harmonic image, Figure 7.11-e-f. Figure 7.12 illustrates the impact of filtering on the respective velocity images.

7.4.4 Angle Image – Wrapping effects

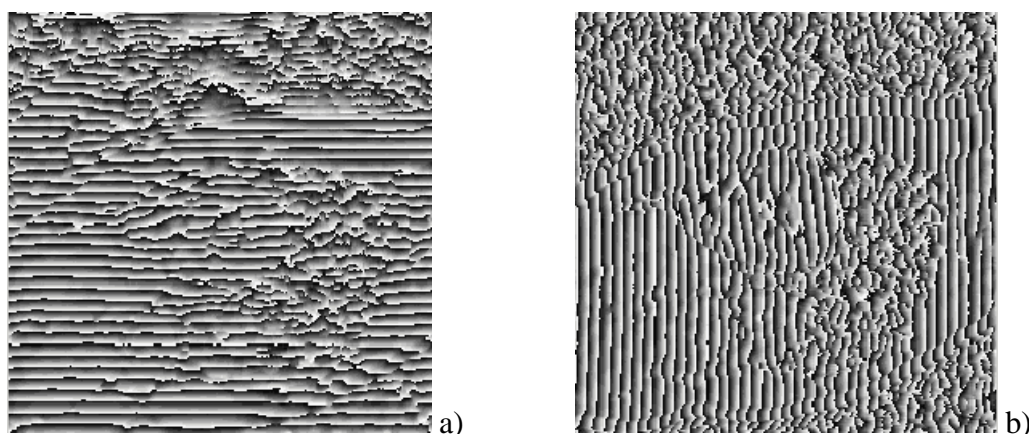


Figure 7.5: Angle Images of 4th frame a) Horizontal Tags, b) Vertical Tags

Finally, angle images are estimated from the inverse harmonic images using the arctan operator, (Eq.5.14). In Figure 7.5 the wrapping effect creates horizontal or vertical stripes from $-\mathbf{p}$ to \mathbf{p} . Although, it is not possible to directly unwrap angle images, it is relatively easy to unwrap their time and spatial difference when the first is between $-\mathbf{p}$ to \mathbf{p} , (Paragraph 5.3). This property is subsequently used to calculate velocity fields and strain maps.

7.5 Calculating Velocity Fields Using Harmonic Phase Images

7.5.1 Derivatives – Median Filter

Figure 7.13 illustrates the spatial derivatives in the x and y directions, before and after median filtering. Generally, derivation introduces noise and thus reduces the signal to noise ratio. Median Filtering was used in order to alleviate these technicalities and improve the resulting velocity fields. Although, median filtering results in smoother images, it is not completely appropriate for this application as it blurs the edges and the myocardium can become difficult to discriminate. However, there are not obvious changes in the final velocity fields.

7.5.2 Unwrapping the subtraction of two successive frames

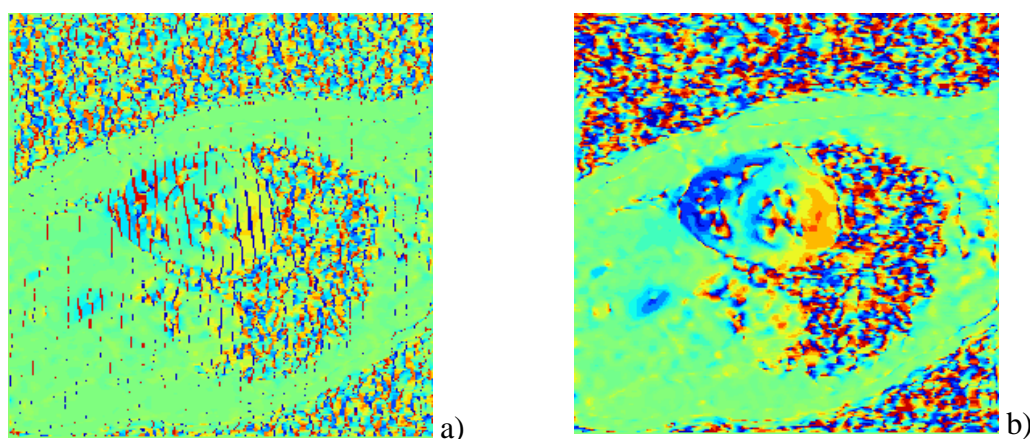


Figure 7.6: The subtraction of two subsequent angles images a) Before Unwrapping, b) After unwrapping

The process of unwrapping the subtraction of two successive frames is fully analysed in (Paragraph 5.3). Figure 7.6 illustrates the results of the unwrapping process using colour-map images scaling by default (using their minimum and maximum values).

7.5.3 Velocity Fields

Figure 7.14 illustrates the velocity fields that have been produced by processing the 3rd and 4th frame of the normal volunteer data. In Figure 7.14-a-b is presented the U_x and U_y components of velocity respectively. The scaling is between -3 to 3. For the U_y component the direction of the Y axis is from the up to down (screen displaying system), while the X axis is as normal from left to right. In Figure 7.14-c the absolute value of velocity is displayed, while in Figure 7.14-d velocity fields are represented as vectors with length the absolute value of the velocity at that point and direction that is provided by the x and y components. The U_x and U_y components of velocity are not sensitive to mis-registration problems, however in order to depict them as vectors those troubles must have been solved. Figure 7.14-d is zoomed to LV only and although the noise of the inside of the myocardium has not eliminated the boundaries of the myocardial wall are clearly discriminated from the blood pools.

The U_x and U_y components of velocity fields indicate that the left part of the LV moves towards the right part of the LV and vice versa, while the top part of the LV is moved towards the bottom part of LV and vice versa. Therefore, there is contraction and clock-wise twisting, shown in Figure 7.14-d, which agree with the fact that the

frames belong to the systolic phase of heart cycle. Moreover, the discrimination of the myocardium is straightforward for all frames of Figure 7.14, although no filtering process has applied.

7.6 Calculating Strain Fields Using Harmonic Phase Images

7.6.1 Principal Eigenvalue and Eigenvector

Estimating the strain tensor has significant contribution in early diagnosis of ischemic diseases as it indicates the distribution of mechanical stress through out the cardiac muscle and thus gives an indication of the energy consumptions of various portions of the myocardium, (Chapter 3). The principal eigenvalue is directly related to the magnitude of stretch/shrink towards the principal direction, for the point under consideration (Paragraph 5.4).

Figure 7.15 illustrates the eigenvalues and eigenvectors for both principal and not direction of the 7th frame of normal volunteer data. The value of the eigenvectors has been normalised to unit, while they direction is perpendicular to each other. The eigenvalues have been scaling from -1.3 to 1.3. Apparently, principal strain, Figure 7.15-a, has greater values than strain at the perpendicular direction, Figure 7.15-c. Furthermore, the direction of the principal eigenvectors indicates stretch/shrink towards the centre of the myocardium, which agrees well with the corresponding velocity data.

7.7 Eliminating noise – Mask

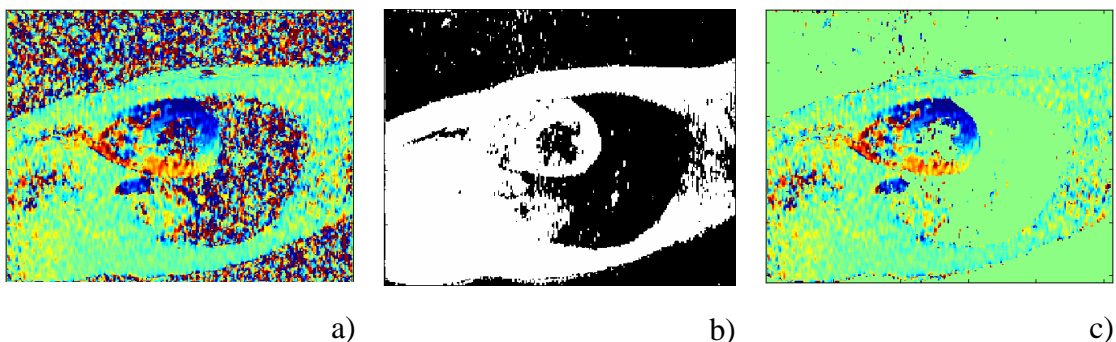


Figure 7.7: a) Velocity Field Before Filtering, b) Mask, c) Velocity Field After Filtering

The MR images have a low signal to noise ratio (SNR), Figure 7.7-a, that affects the processing and makes visualisation of velocity and strain rate difficult. The mask, Figure 7.7-b, eliminates noise from the lungs outside the myocardium and the blood pool within the LV. In practice, it constitutes a threshold filter that requires the summation of the magnitude of the inverted harmonic peak of the vertical tags and the magnitudes of the vertical tagging images before the subtraction, to be above a certain value. The threshold value is empirically chosen, usually between 15 and 40. The calculation of velocity requires two time frames, and thus, there are two masks that can be applied. However, the results do not differ significantly.

Unfortunately, the mask is not as efficient as in the first frames during the later frames of the cardiac cycle where the tagging fades and the SNR is lower. However, it contributes to a better visualisation scheme and is fully automatic. Manual or semi-automatic segmentation of the myocardial contours would allow an easier visualization of the velocity and strain fields with the myocardium at the expense of human intervention and speed.

7.8 Restoration of Vector Fields

Vector fields restoration of velocity fields is shown in Figure 7.16. Figure 7.16-a displays the vector map before restoration, while Figure 7.16-b is after. Velocity fields have been produced from the 3rd and 4th frame on normal volunteer data. The parameters that are chosen for restoring these fields are 60 iterations with the weight of the neighbour points set to 1 and the weight of the point under consideration set to 0, while the rate of change Δt is set to 0.1. Usually, an efficient number of iterations is between 30 to 60, while the weight of neighbour points should be around one in order for the vector fields to converge smoothly. The larger the weight of the point under consideration is, the larger the number of iterations needed to restore vector fields. Finally, Δt can dramatically affect the results. In the case that it has relatively large values, such as 0.2-1 or above, the results are particularly messy and meaningless. On the other hand, when Δt has small values the convergence is slow.

The results in Figure 7.16-b indicate that velocity fields have been smoothed and thus it is easier to observe the twisting myocardial motion. Vector restoration is particularly efficient at the middle wall between the right and left ventricle, where

velocity fields are affected by the blood pool of the both right and left ventricle and thus it is difficult to study their regular pattern. Moreover, the regions near the endocardial and epicardial boundaries are better studied after vector fields restoration and this is especially appreciated in case of ischemic diseases, (Paragraph 1.7).

7.9 Results

7.9.1 Comparing SPAMM and CSPAMM velocity fields

A comparison between velocities fields that have been produced from SPAMM and CSPAMM images are represented in Figure 7.18 and Figure 7.17, respectively. The results agree but the image quality and signal to noise ratio in case of CSPAMM is obviously better. Moreover, using CSPAMM images it is possible to assess myocardial motion through out the cardiac cycle, Figure 7.17-e-f, while the corresponding SPAMM images deteriorate considerably during the last frames of the cardiac cycle, Figure 7.18-e-f.

Furthermore, the results agree well with the expected cardiac cycle. The cardiac muscle starts to contract from the 1st frame and velocity comes up to its peak between the 3rd and 4th frames, Figure 7.17-a-b. In Figure 7.17-c-d the heart motion is at the last phases of systolic motion, while in Figure 7.17-e-f illustrates the peak of cardiac diastolic motion. Indeed, U_x and U_y components of Figure 7.17-e-f indicate the motion of the myocardial tissue towards the opposite direction of the blood pool of the LV.

7.9.2 Based on CSPAMM: Comparing patient data and normal data

Velocity Fields:

In this paragraph velocity fields from normal volunteer and patient with HCM are compared in order to validate the efficiency of HARP MRI in a clinical environment. HARP MRI successfully illustrates anomalies in myocardial motion of HCM patient. The cardiac systolic phase is limited to the first two time frames, Figure 7.20, of the cardiac cycle, while in the subsequent phases the myocardial muscle contracts only partly, Figure 7.20-e-f.

Better investigation of the myocardial motion of both normal volunteer and patient is provided in Figure 7.21 - Figure 7.22, respectively, which have been zoomed to LV and LV & RV, respectively. These figures illustrate velocity fields as vectors for each frame of the whole cardiac cycle for both samples. The results indicate that assessing of myocardial motion is accurate even for the last frames of the cardiac cycle, although the signal to noise ratio has been reduced as a consequence of tag fading. In normal volunteer results the myocardium wall can easily discriminated from both inside and outside for all the phases of the cardiac cycle, indicating the accuracy of HARP MRI in estimating motion and deformation near the boundaries.

The normal myocardial motion designates a smooth anti-clockwise twisting motion from the first frame, Figure 7.21-a, which increases at the second frame, Figure 7.21-b, and results in apparent contraction during the next three frames, Figure 7.21-c-d-e. The frame in Figure 7.21-f indicates temporal equanimity that is the start of diastolic phase, which is clearly illustrated at frames Figure 7.21-k-l. The two last frames of normal volunteer data has been omitted for displaying purposes as they do not have any significant contribution to the overall analysis of the cardiac cycle.

On the other hand, frames from the patient data obviously indicate the severe of his disease as it is almost impossible to discriminate the LV from the RV. Furthermore, the systolic phase starts abruptly during the first two frames, Figure 7.22-a-b, where, abnormally, anti-clockwise motion, Figure 7.22-a, is followed by clock wise contraction, Figure 7.22-b. Diastolic phase is completed at Figure 7.22-k frame where the noisy vectors at the right and left sides of the centre of the myocardium indicate the LV and RV blood pools, respectively. The enlarge wall muscle comparing to blood pools is a certain characteristic of the HCM disease.

Strain Maps:

Figure 7.23 illustrates the principal eigenvalues and corresponding eigenvectors through out the cardiac cycle of the normal volunteer. Similarly to velocity fields strain maps can be calculated during the whole cardiac cycle. However, eigenvalues are especially sensitive to the registration errors, which results in meaningless and vague maps.

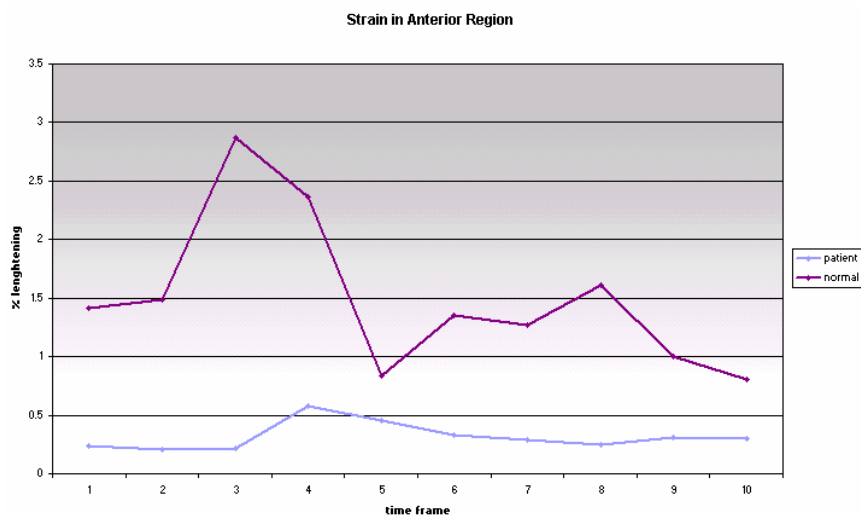


Figure 7.8: Average value for the anterior/septal region in both patient and normal. The difference in the two values can be seen although the trend of the strain development through the cardiac cycle is similar.

The direction of the principal eigenvectors indicates deformation towards the centre of the myocardium, which can be also observed in velocities fields. However, velocity fields represent a different physical entity and thus they do not directly correspond to strain maps. This is better explained, considering that a point with significant velocity may not be stretched/shrunk yet and vice-versa. The results indicate that between velocity fields and strain maps there is apparent correlation, although, a direct association of velocity fields and strain maps is not possible. Figure 7.8 has been plotted by averaging the anterior/septal region in both patient with HCM and normal volunteer. The results indicate clearly, that contraction at anterior is significantly lower in patient data than normal.

7.10 Discussion

These results show that spectral peak filtering and the MR acquisition process are significant factors in HARP MRI. CSPAMM provides images with better signal to noise ratio than SPAMM and the results agree well with the expected heart motion. Moreover, HARP based on SPAMM is more sensitive to spectral peak filtering, which is particularly significant in the last time frames when the central peak has enhanced considerably. This investigation concludes that the combination of HARP MRI and CSPAMM acquisition process provides significant functional information that has the potential of indicating myocardial abnormalities and dysfunction.

During the processing of data of the same sequence the software parameters, which determine the spectral peak filtering, do not change. This means that there is no manual intervention needed to segment the spectral peak and the processing can be carried out for all frames automatically and rapidly. Any mis-registration between the images from the two tag directions does not affect the U_x and U_y components of velocity fields, however the strain maps become meaningless. This is a factor that should be explored further in the data acquisition and reconstruction process.

In normal volunteer data the myocardial wall can be clearly discriminated from the blood pools and the outside environment, while myocardial tissue motion at the inside of the myocardial wall agrees well with what is expected through out the whole cardiac cycle. This analysis shows that HARP MRI can be easily adapted to a clinical environment with minimum cost and has the potential of accurately monitoring the heart function. The patient data are promising as they are indicating that HARP MR can detect abnormalities in both velocity fields and strain maps. Although, the signal to noise ratio is increased it is able to discriminate the anterior/septum of the myocardium as problematic as the contraction there is minimum during the whole cardiac cycle. Further investigation is needed to determine the sensitivity and specificity of HARP MRI and test its effectiveness in a clinical environment.

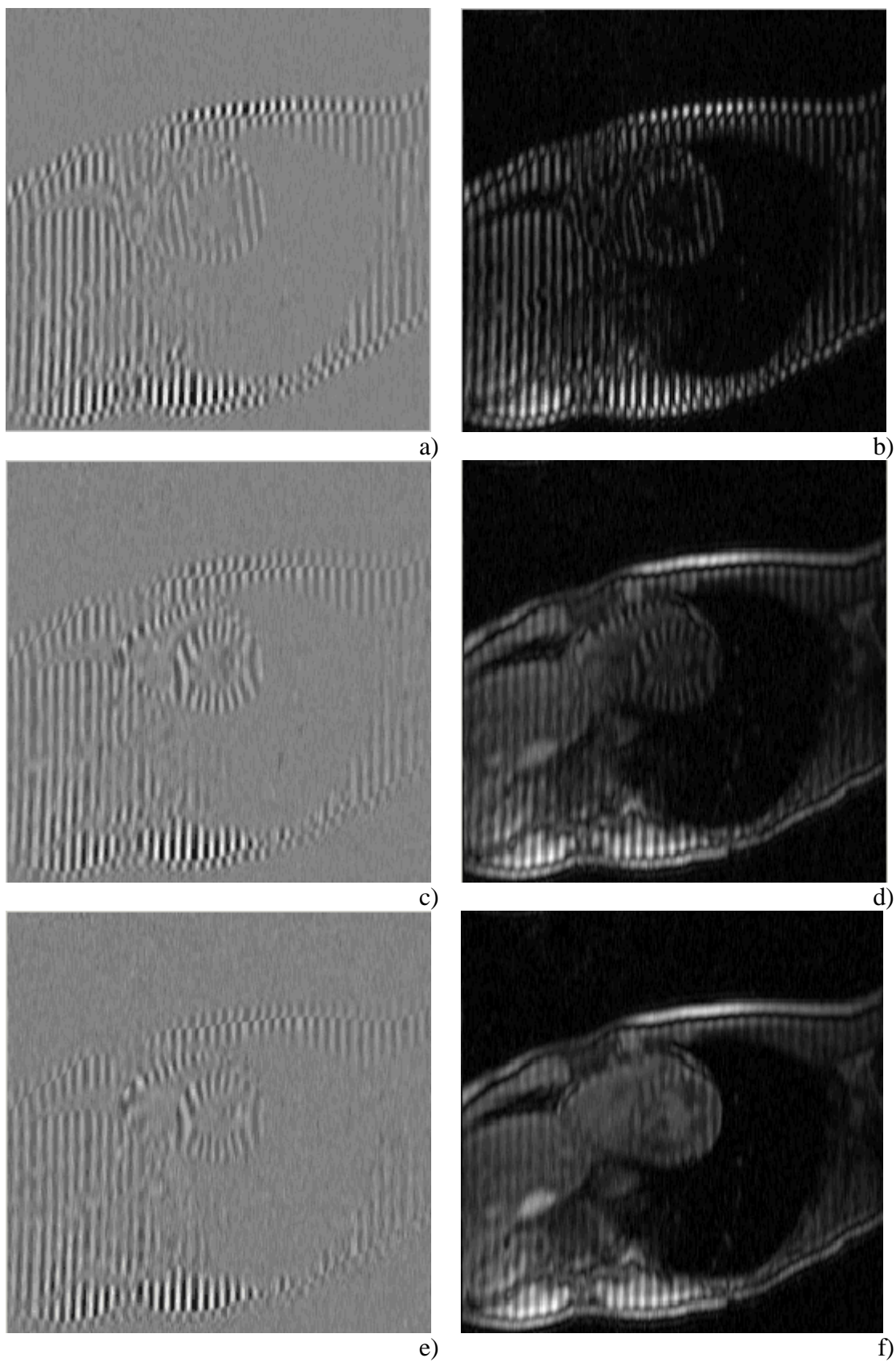


Figure 7.9: CSPAMM and SPAMM Magnitude Images a-b) 3rd Time Frame, c-d) 9th Time Frame, e-f) 12th Time Frame

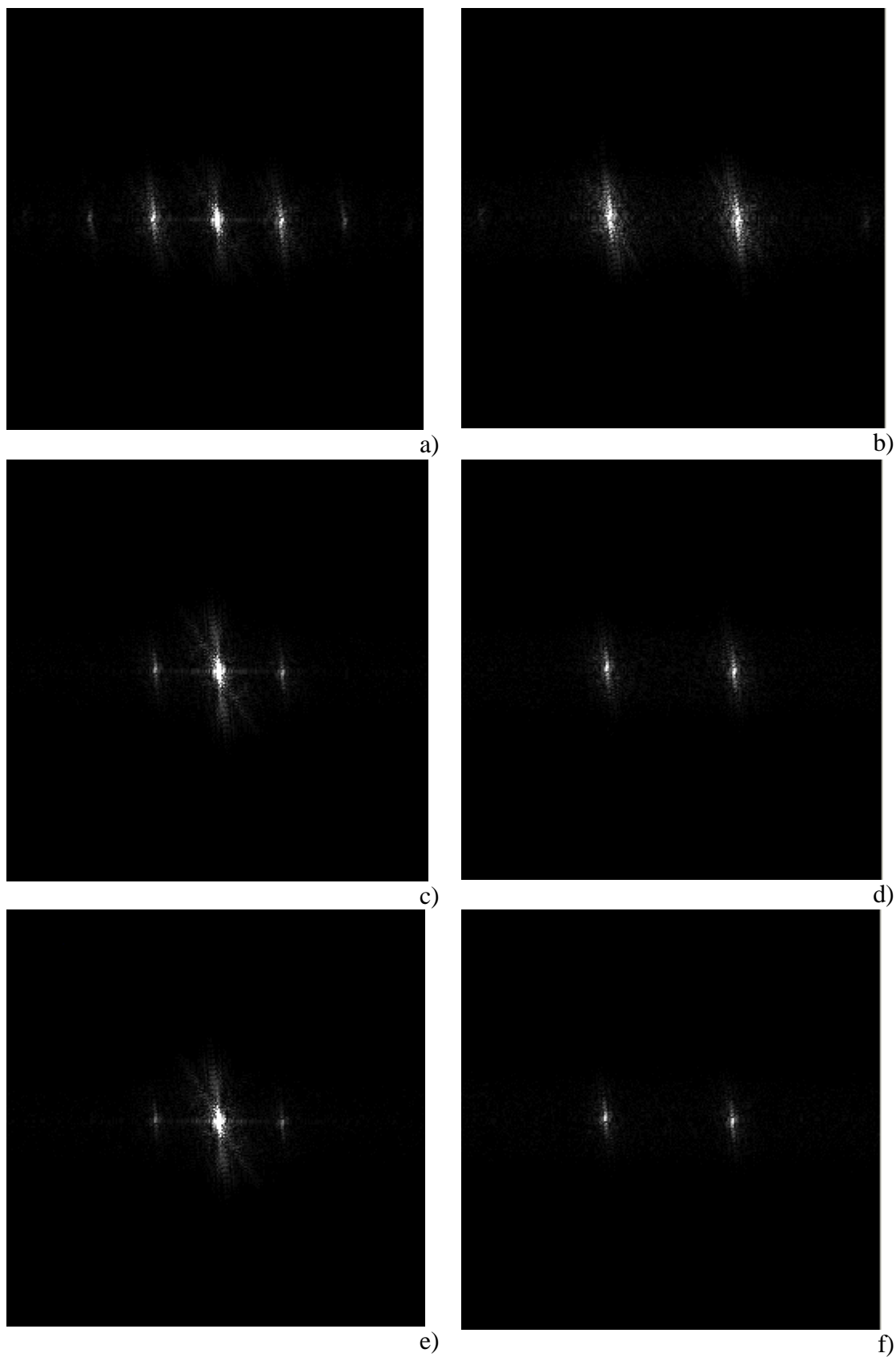


Figure 7.10: SPAMM – CSPAMM Fourier Spectrum a-b) 3rd Time Frame, c-d) 9th Time Frame, e-f) 12th Time Frame

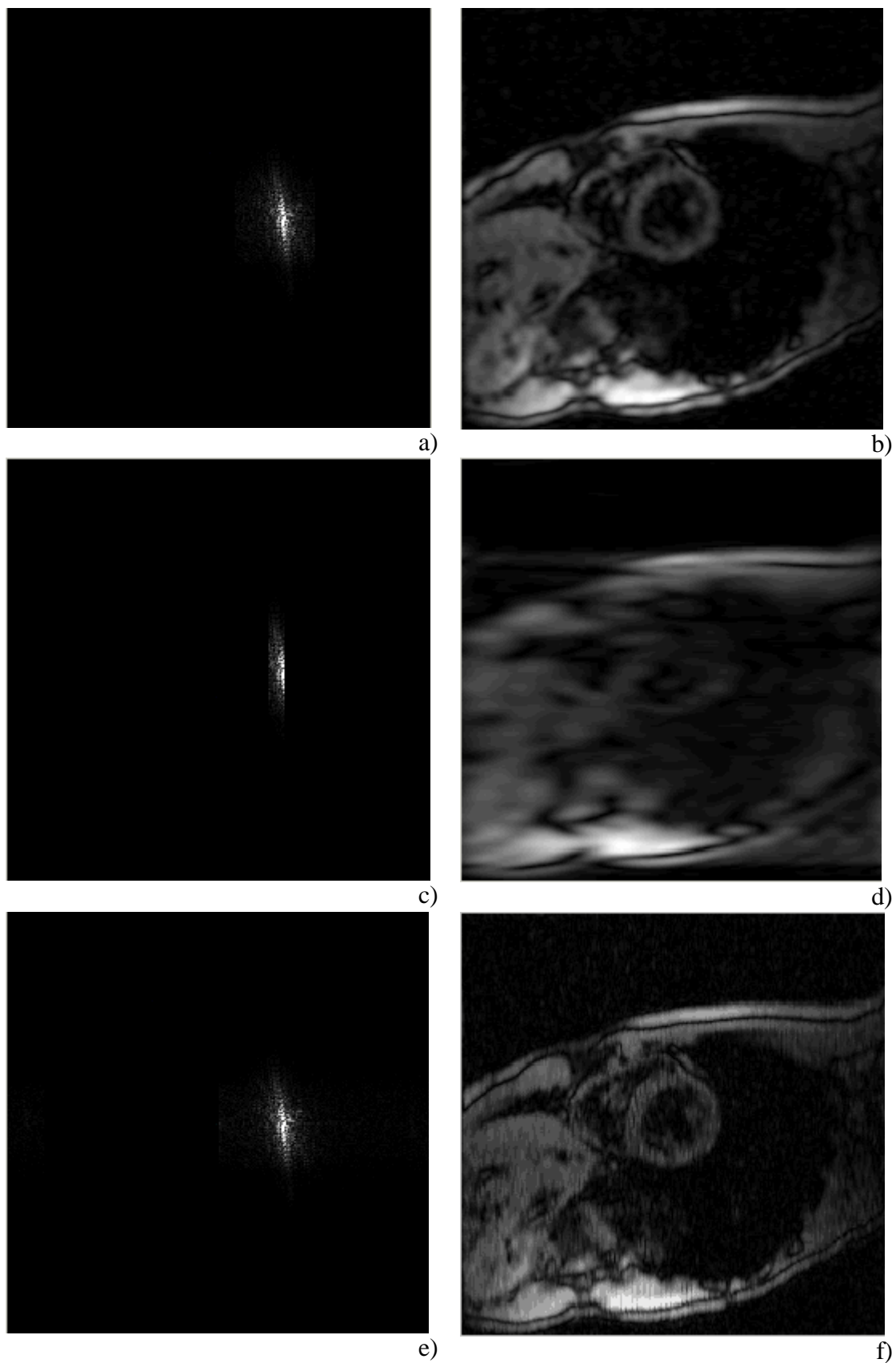


Figure 7.11: Spectral Peak Filtering CSPAMM, Vertical Tags – frame 4: a-b) normal: 10 58 0 256, c-d) Over filtering: 30 40 0 256, e-f) Under filtering: 0 150 0 256

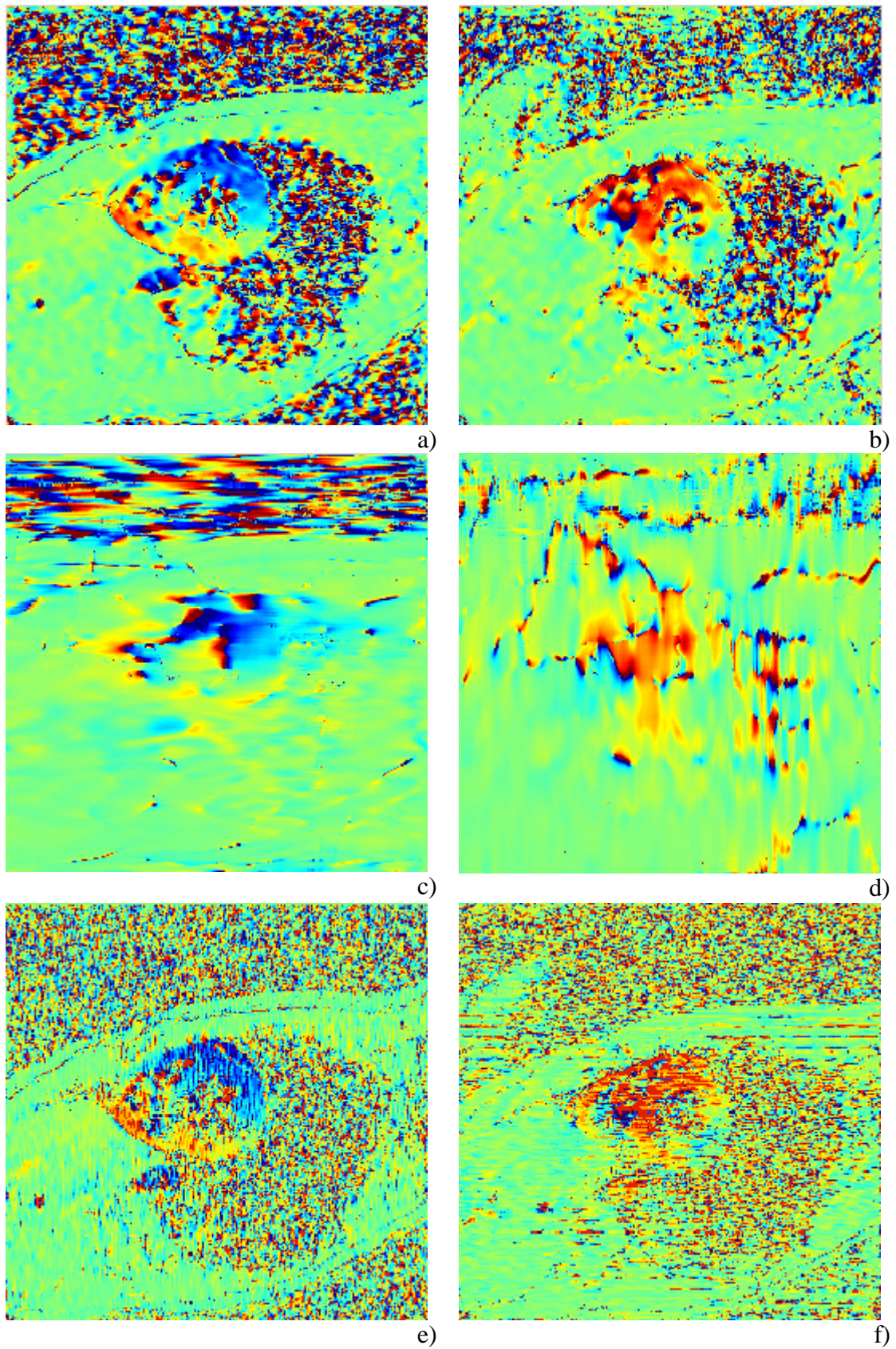


Figure 7.12: Velocity Fields, 3-4 frames, $U_x - U_y$ components a-b) Normal Filtering, b-c) Over Filtering, e-f) Under Filtering

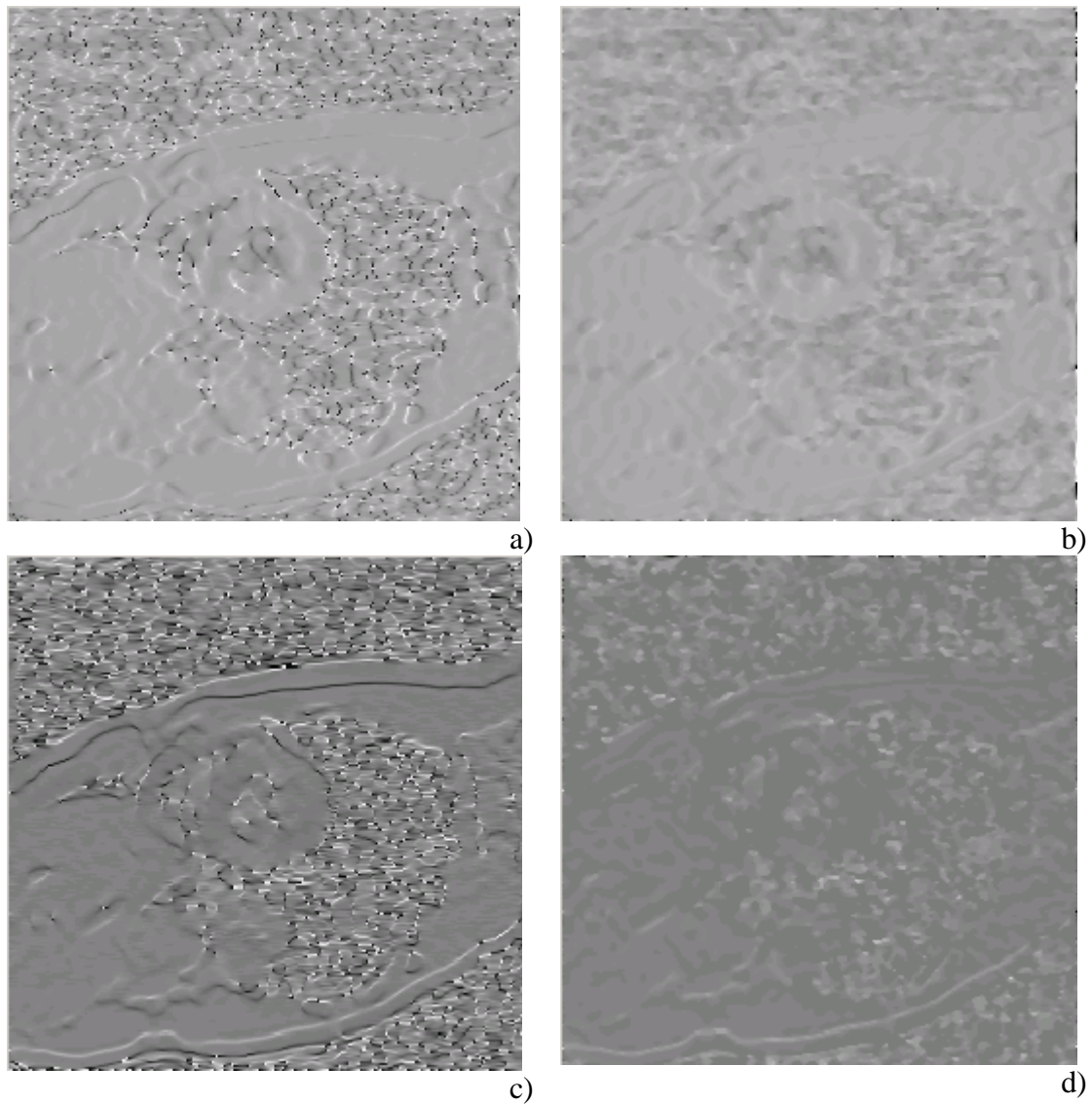


Figure 7.13: Vertical Tags Angle Derivatives before and after median filtering a) X-axis derivative before median filtering, b) X axis Derivative after Median Filtering, c) Y-axis derivative before median filtering, d) Y-axis Derivative after median filtering

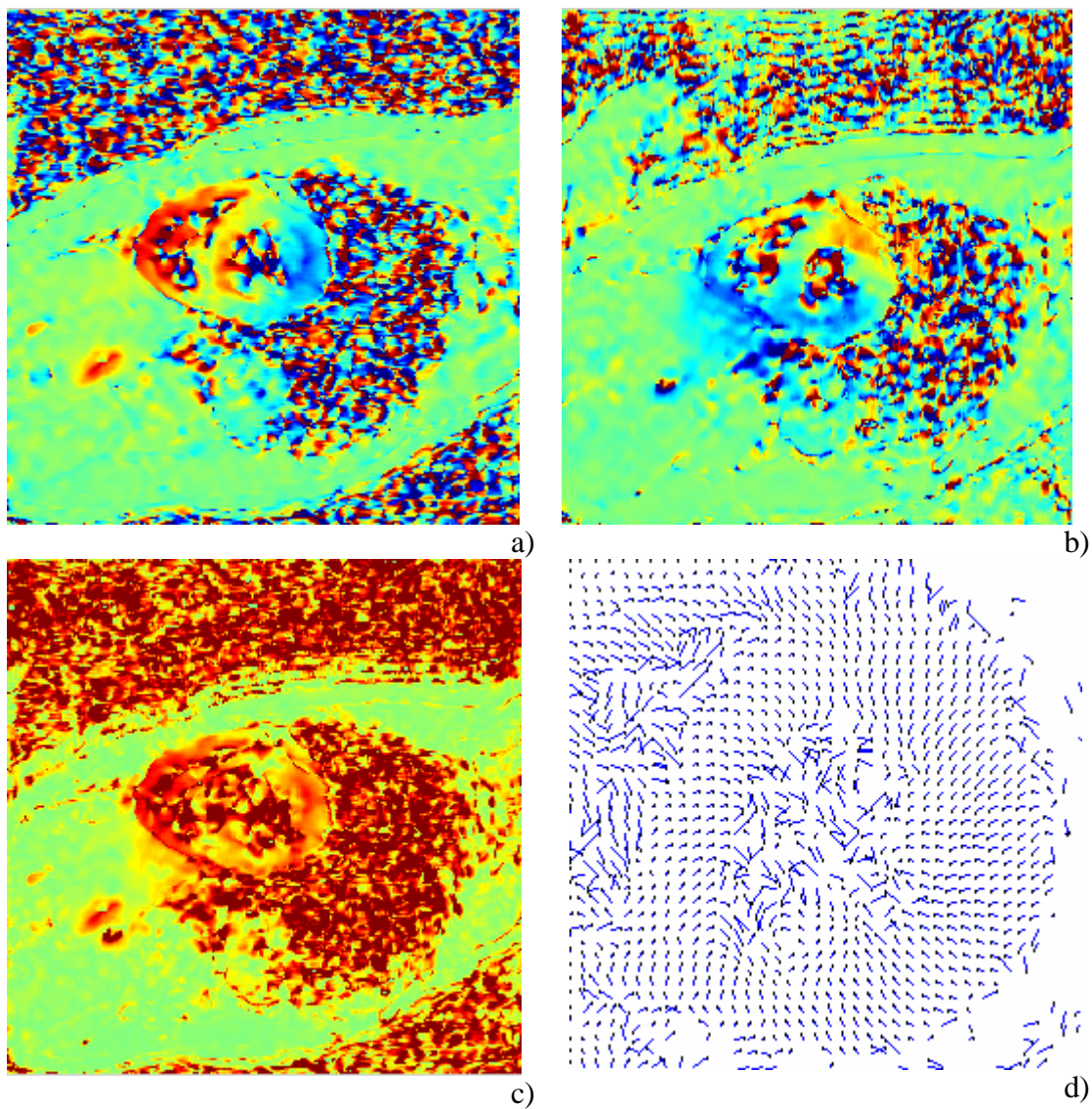


Figure 7.14: Velocity Fields 3-4 frames a) U_x component, b) U_y component, c) Absolute Value, d) Vectors

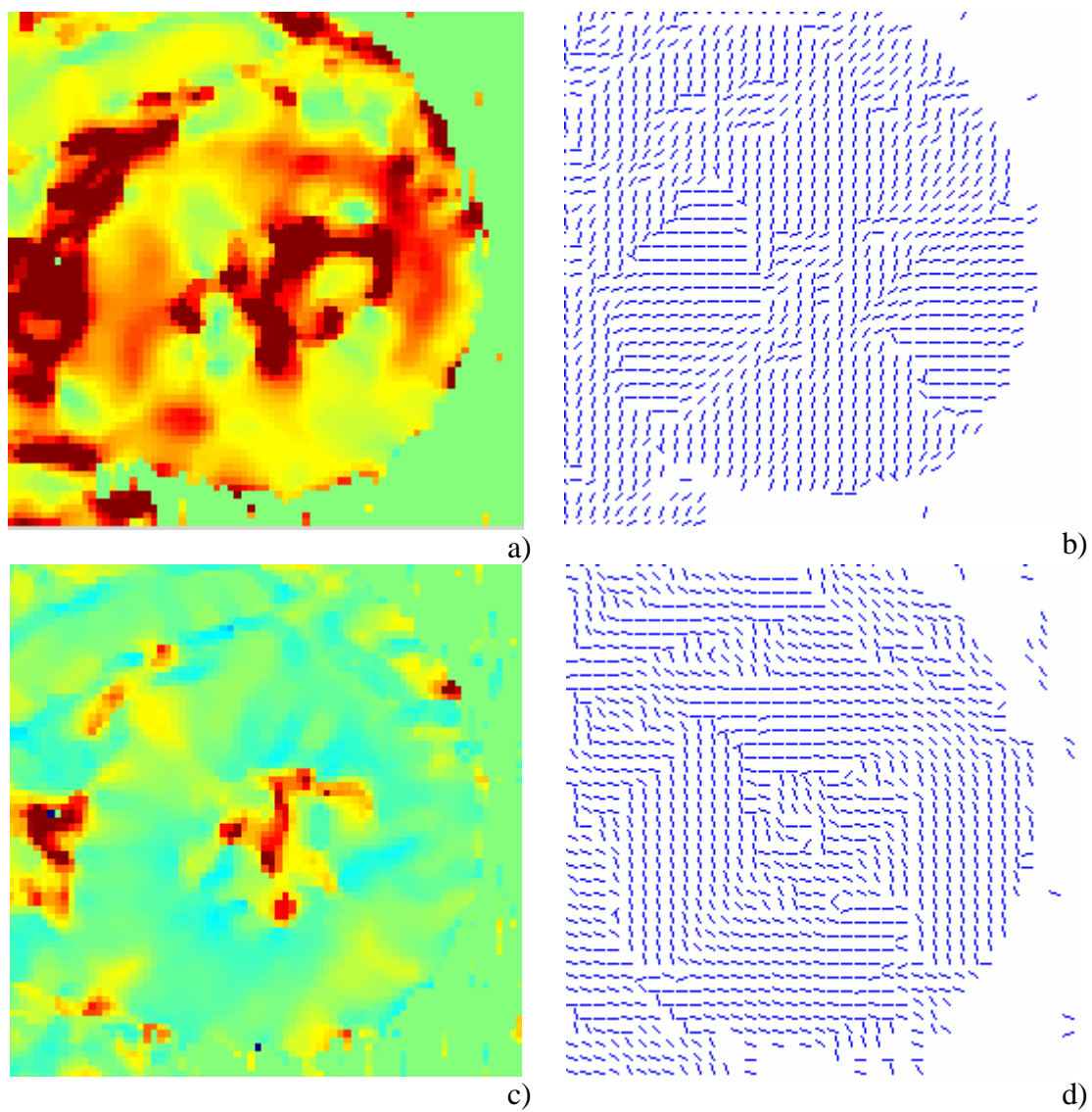
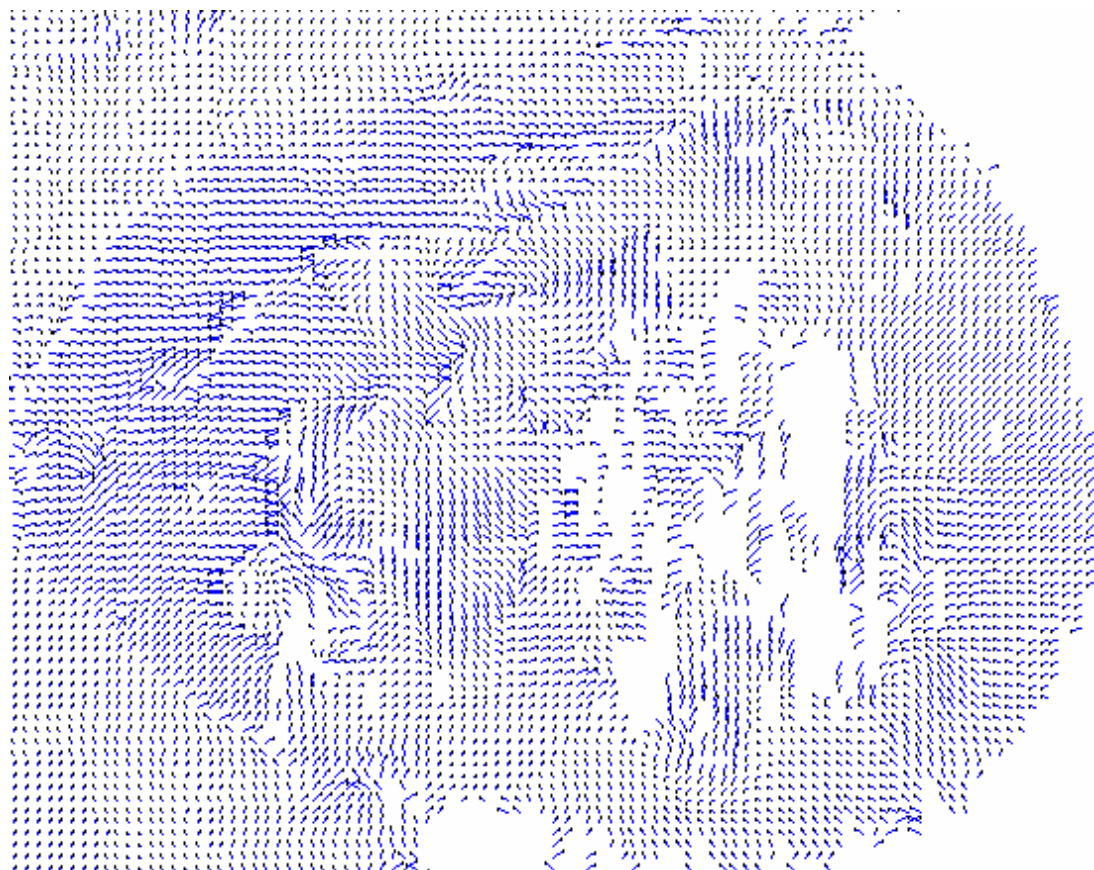
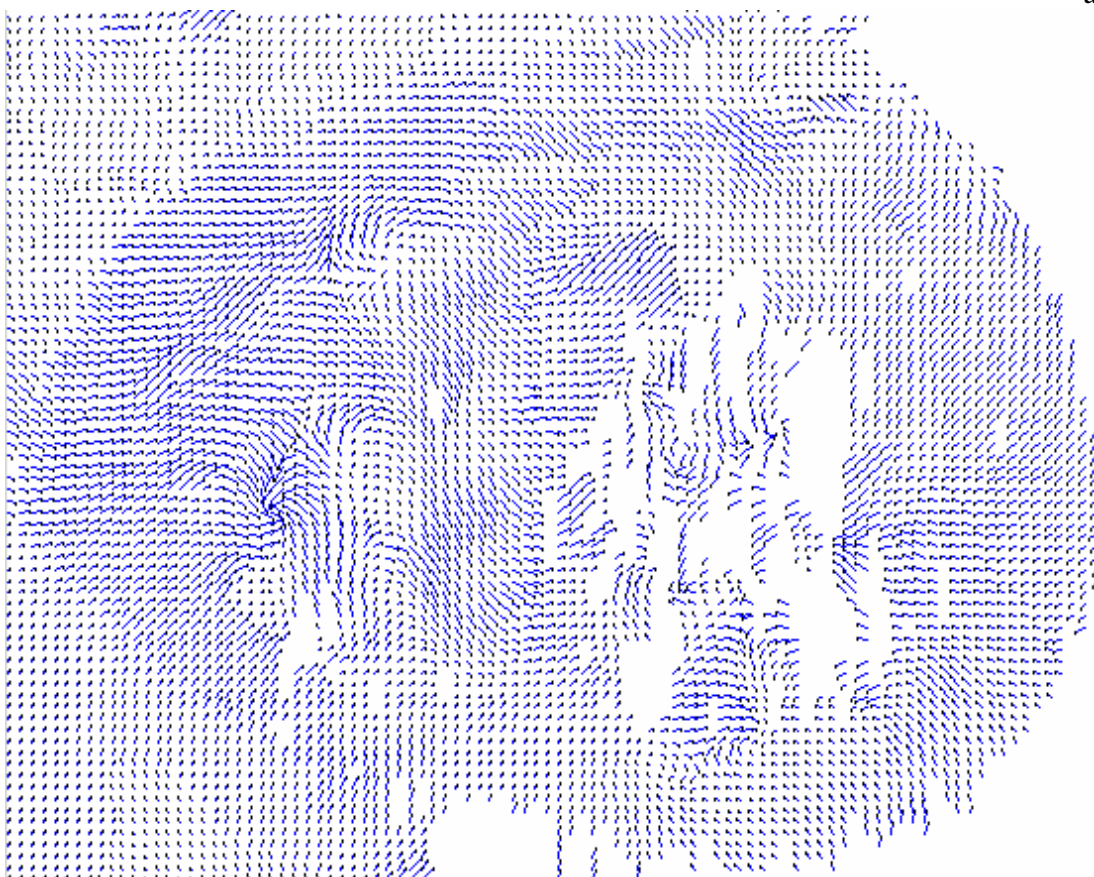


Figure 7.15: Eigenvalues and Eigenvectors of the 7th frame of patient data a) Principal eigenvalue, b) Principal Eigenvector, c) The other eigenvalue, d) Eigenvector perpendicular to Principal direction



a)



b)

Figure 7.16: Velocity Fields a) Before Restoration, b) After Restoration

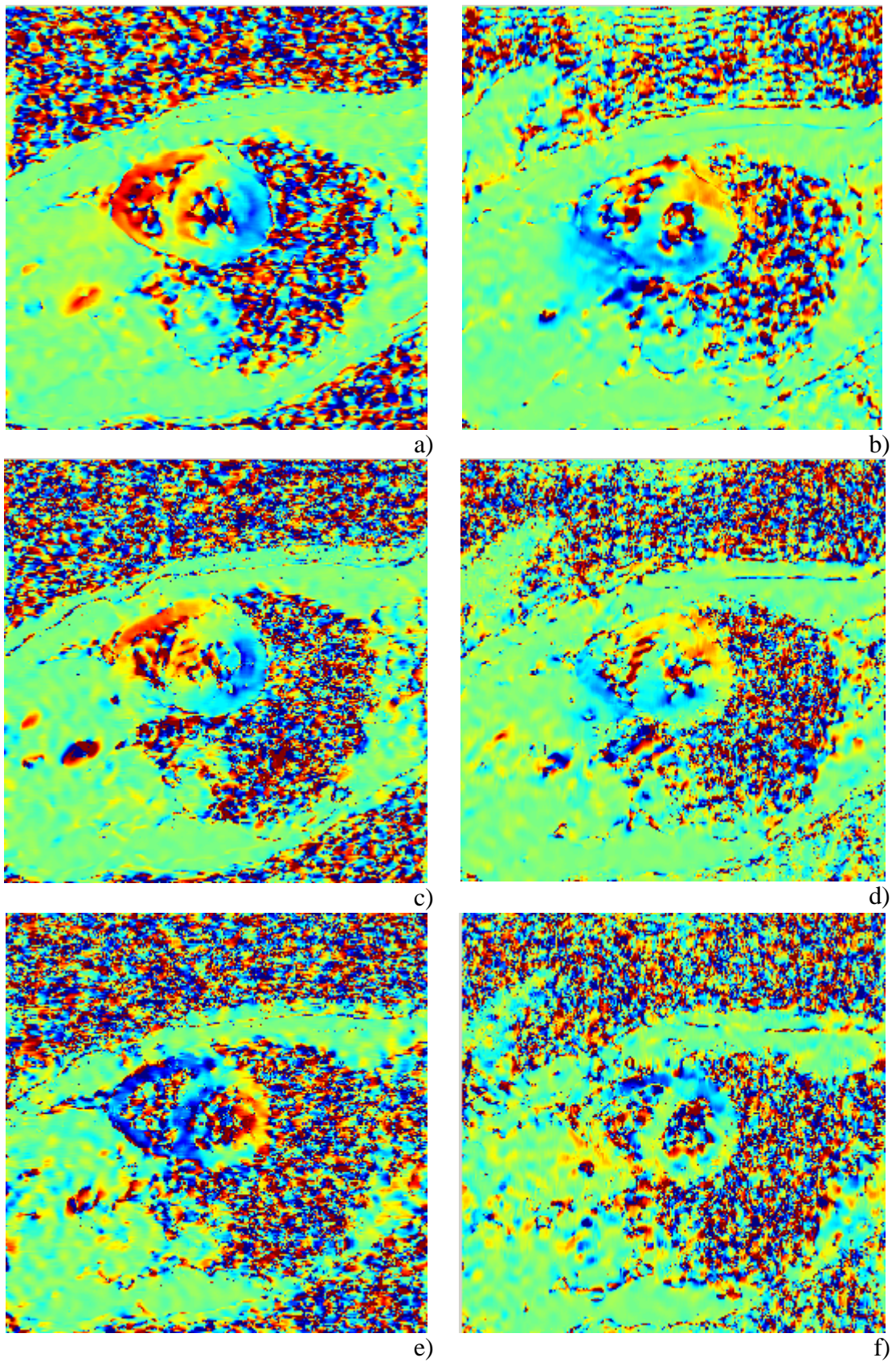


Figure 7.17: $U_x - U_y$ velocity components from CSPAMM images a-b) 3-4 time frames, c-d) 5-6 time frames, e-f) 11-12 time frames

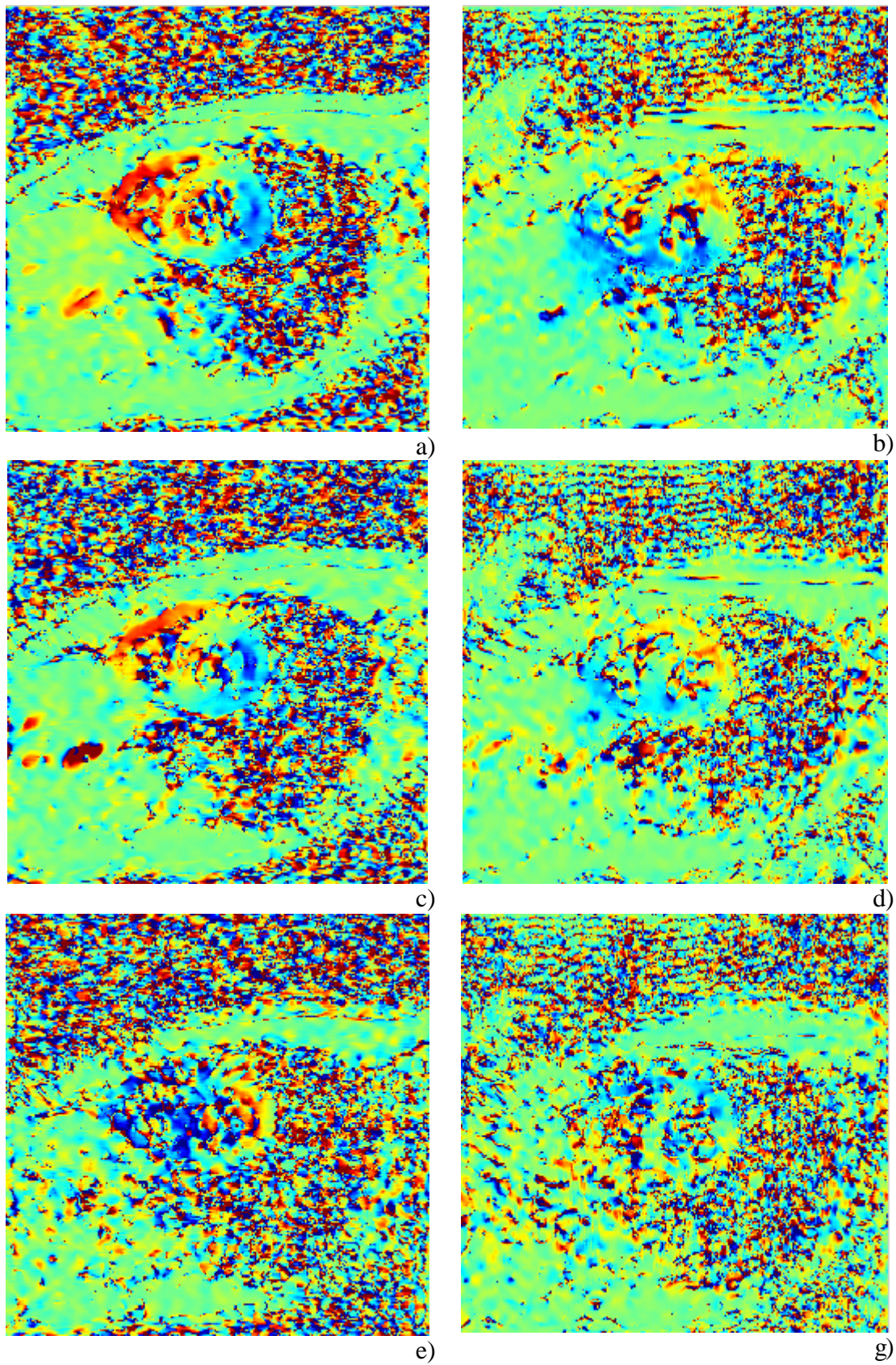


Figure 7.18: $U_x - U_y$ velocity components from SPAMM images a-b) 3-4 time frames, c-d) 5-6 time frames, e-f) 11-12 time frames

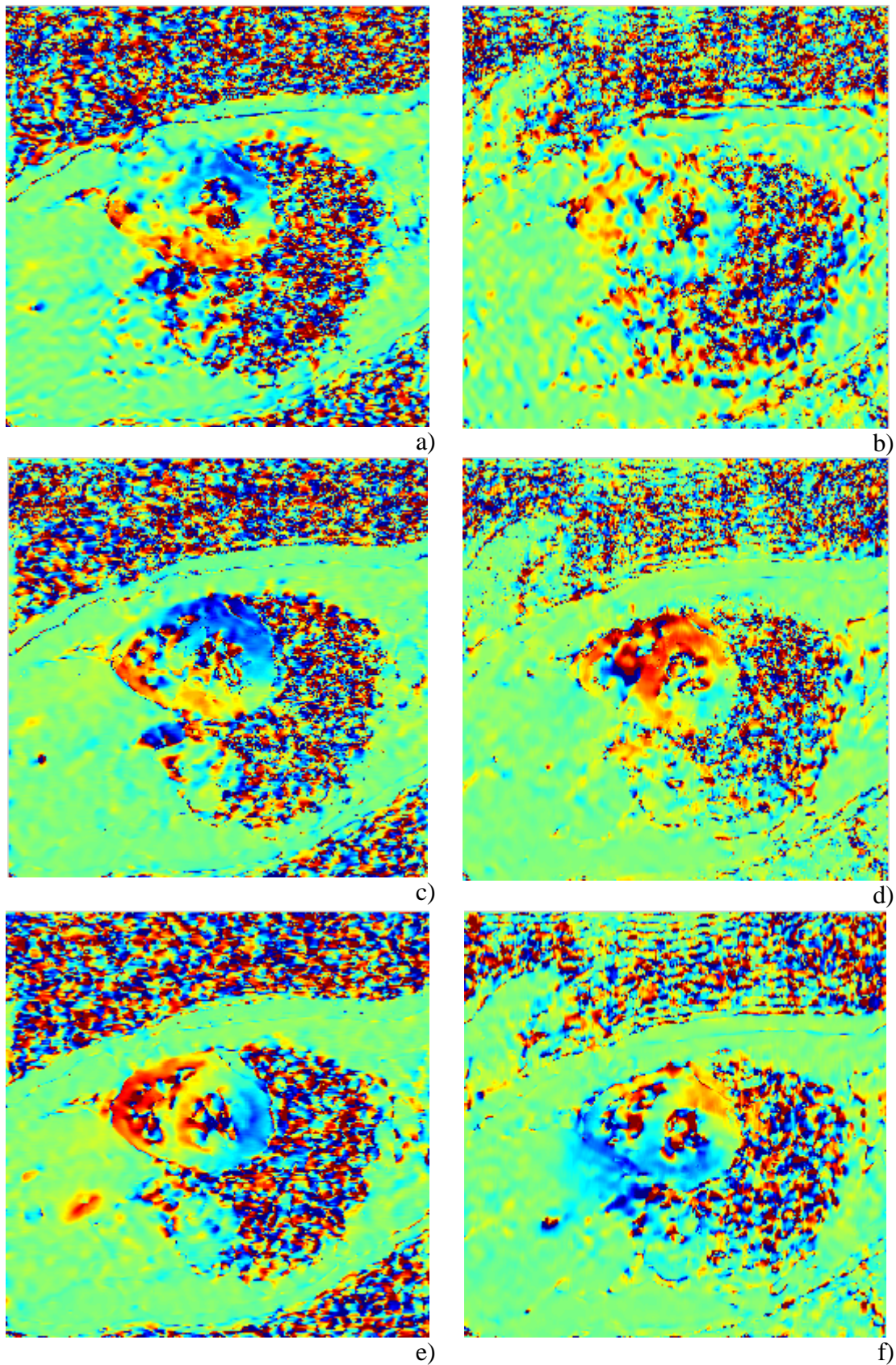


Figure 7.19: $U_x - U_y$ velocity components from CSPAMM images – Normal Volunteer data a-b) 1-2 time frames, c-d) 2-3 time frames, e-f) 3-4 time frames

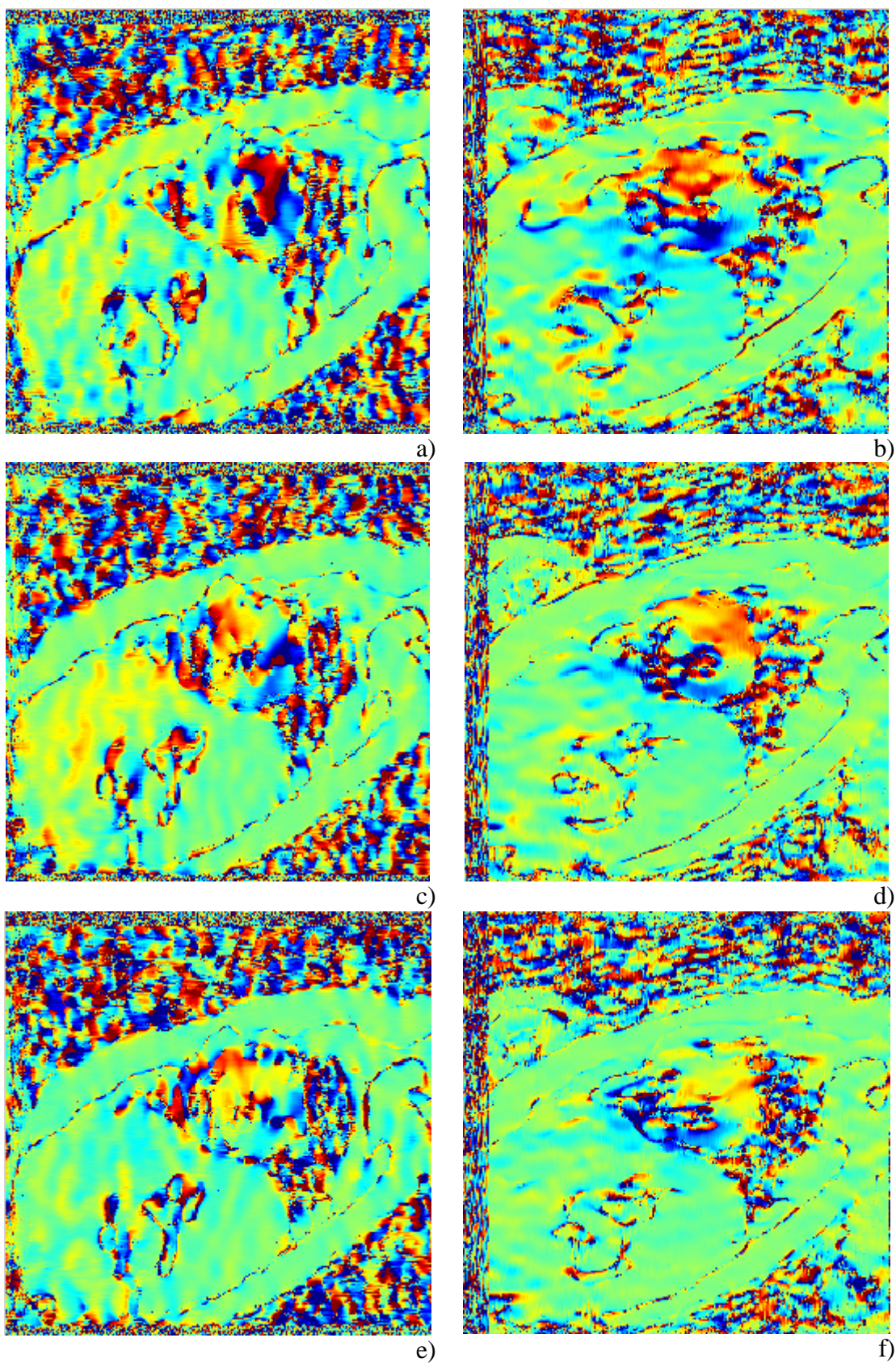
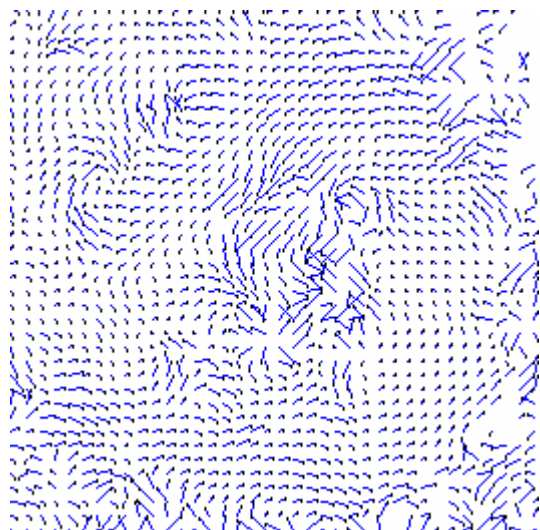
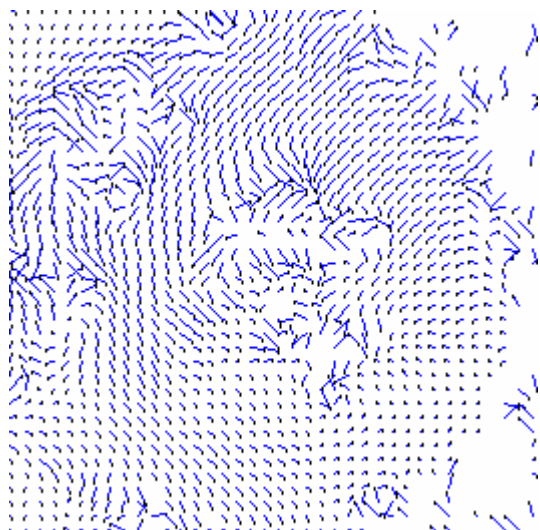


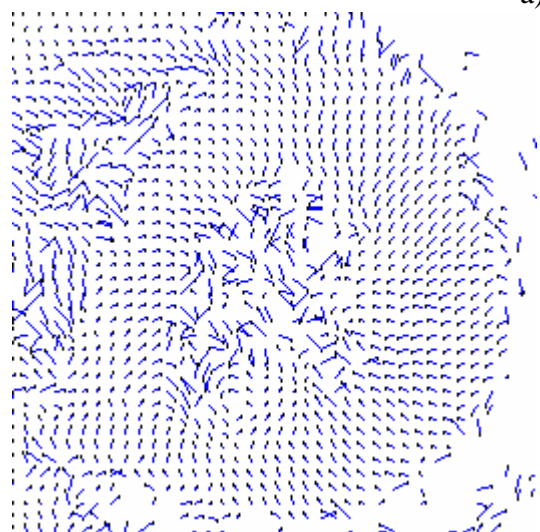
Figure 7.20: $U_x - U_y$ velocity components from CSPAMM images – HCM patient data a-b) 1-2 time frames, c-d) 2-3 time frames, e-f) 3-4 time frames



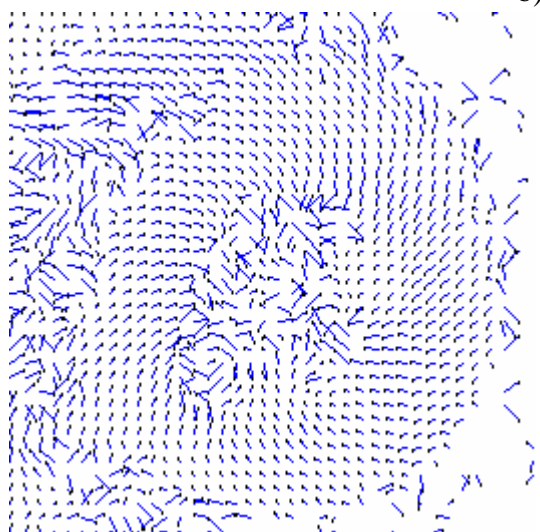
a)



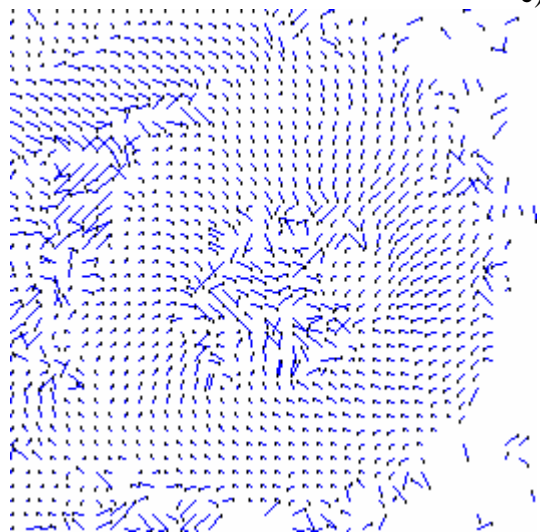
b)



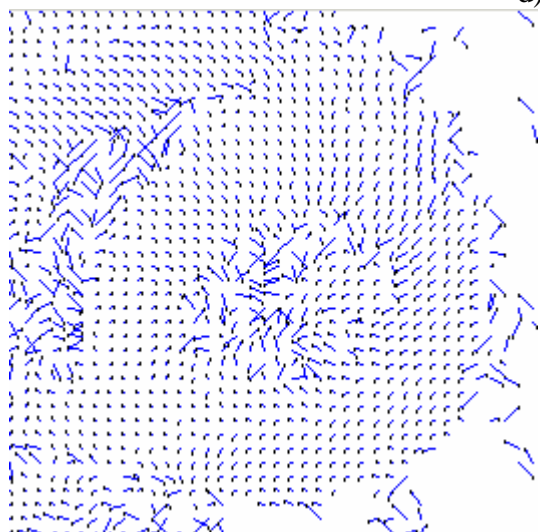
c)



d)



e)



f)

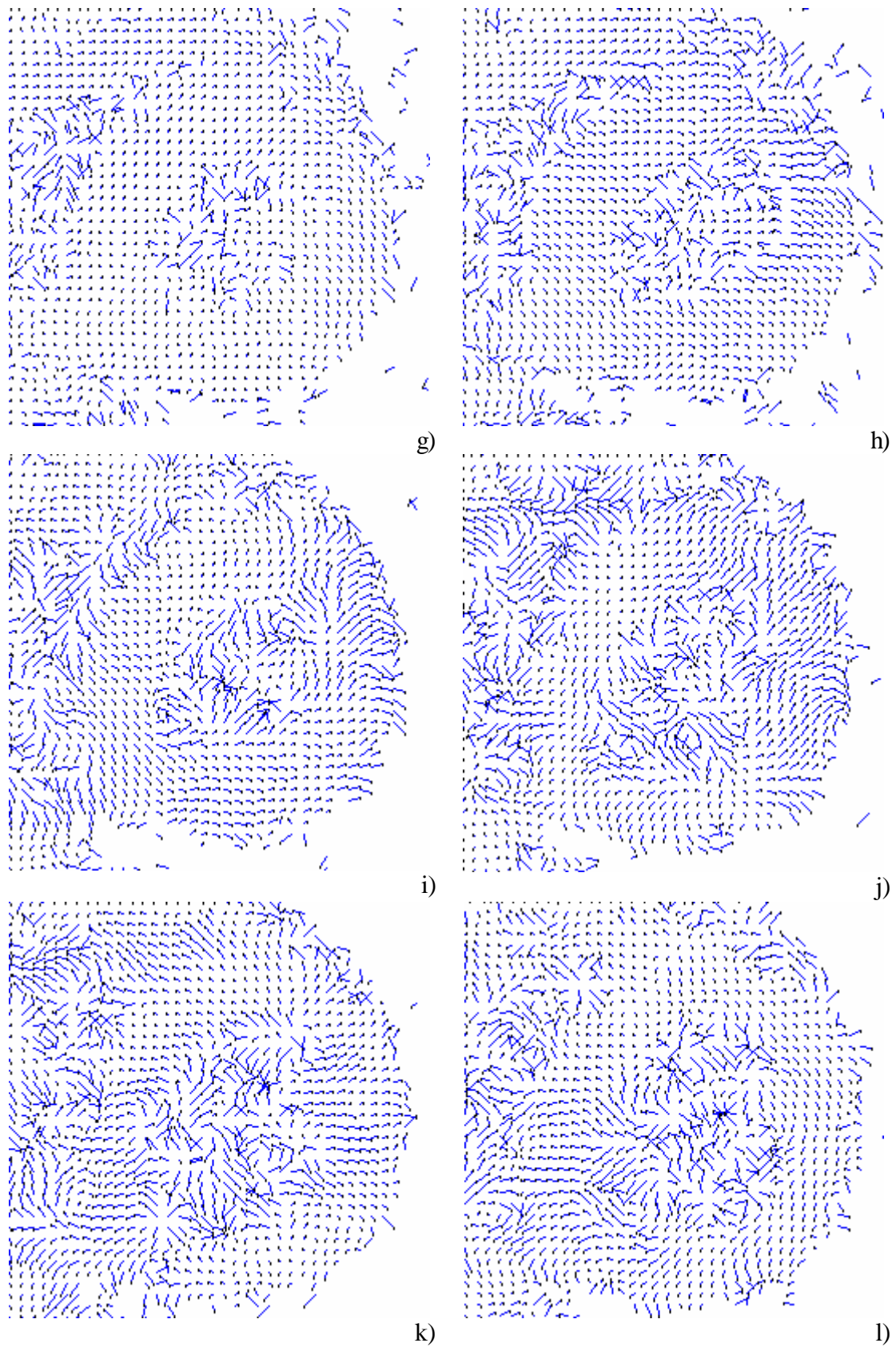
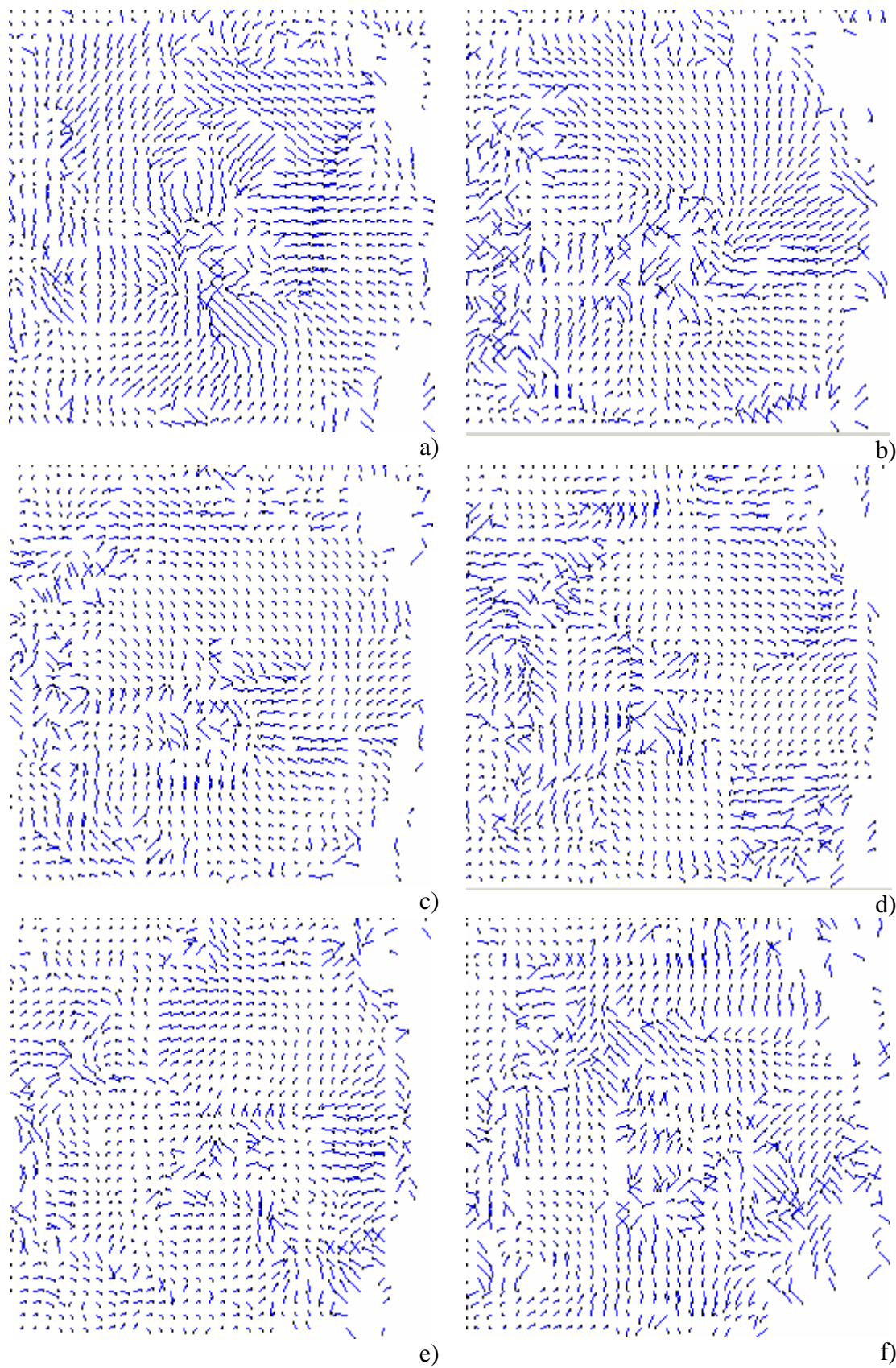


Figure 7.21: Normal Volunteer Velocity Fields Through out the cardiac cycle, LV a) 1-2 frame, b) 2-3 frame, c) 3-4 frame, d) 4-5 frame, e) 5-6 frame, f) 6-7,frame g) 7-8 frame , h) 8-9 frame, i) 9-10 frame, j) 10-11 frame, k) 11-12 frame, l) 12-13 frame



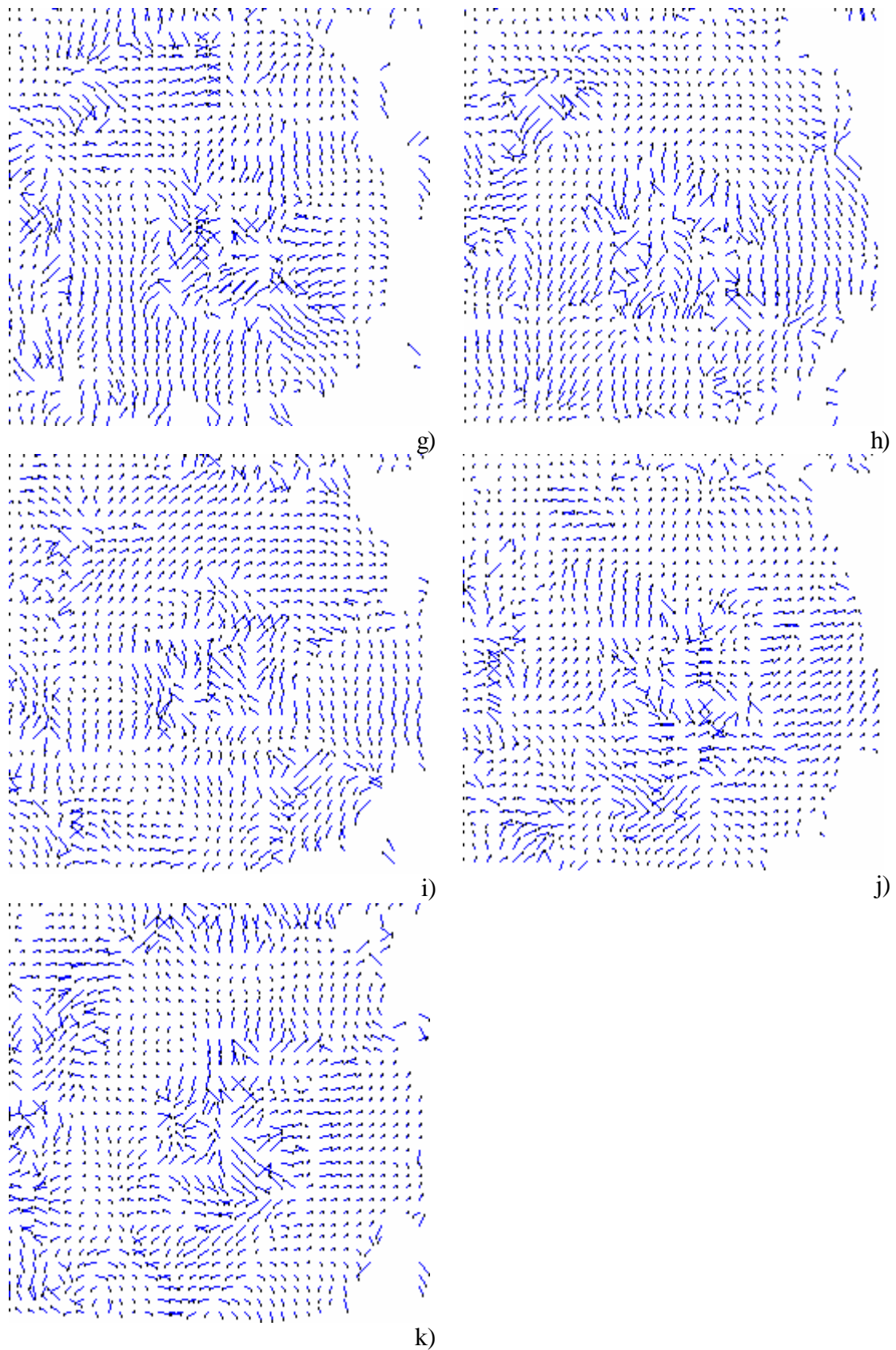


Figure 7.22: Patient Data with HCM LV & RV, a) 1-2 frames, b) 2-3 frames, c) 3-4 frames, d) 4-5 frames, e) 5-6 frames, f) 6-7 frames, g) 7-8 frames, h) 8-9 frames, i) 9-10 frames, j) 10-11 frames, k) 11-12 frames

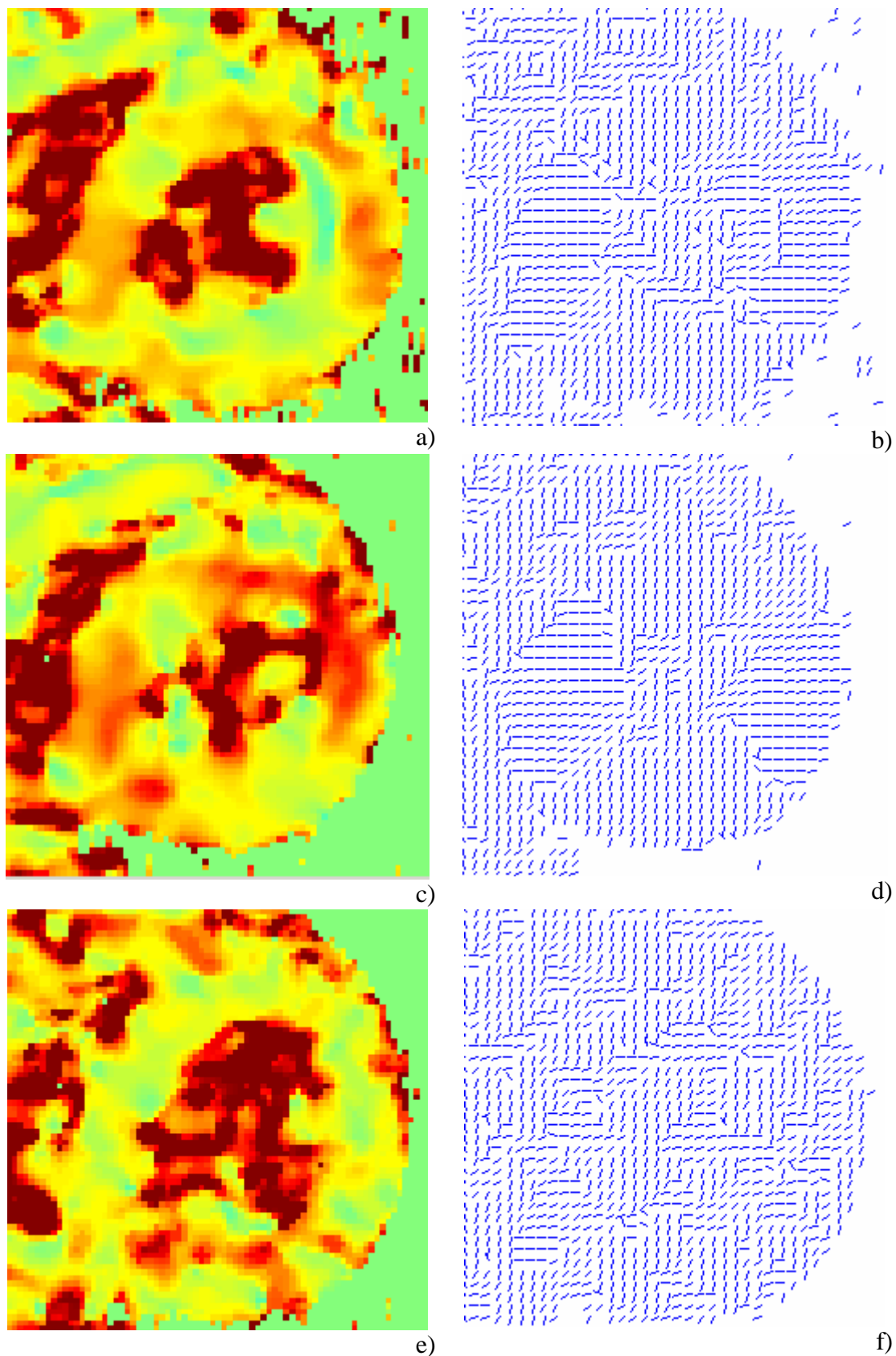


Figure 7.23: Normal Volunteer, Principal Eigenvalues – left column, Principal Eigenvectors – Right Columns, a-b) 3rd frame, c-d) 5th frame, e-f) 11th frame

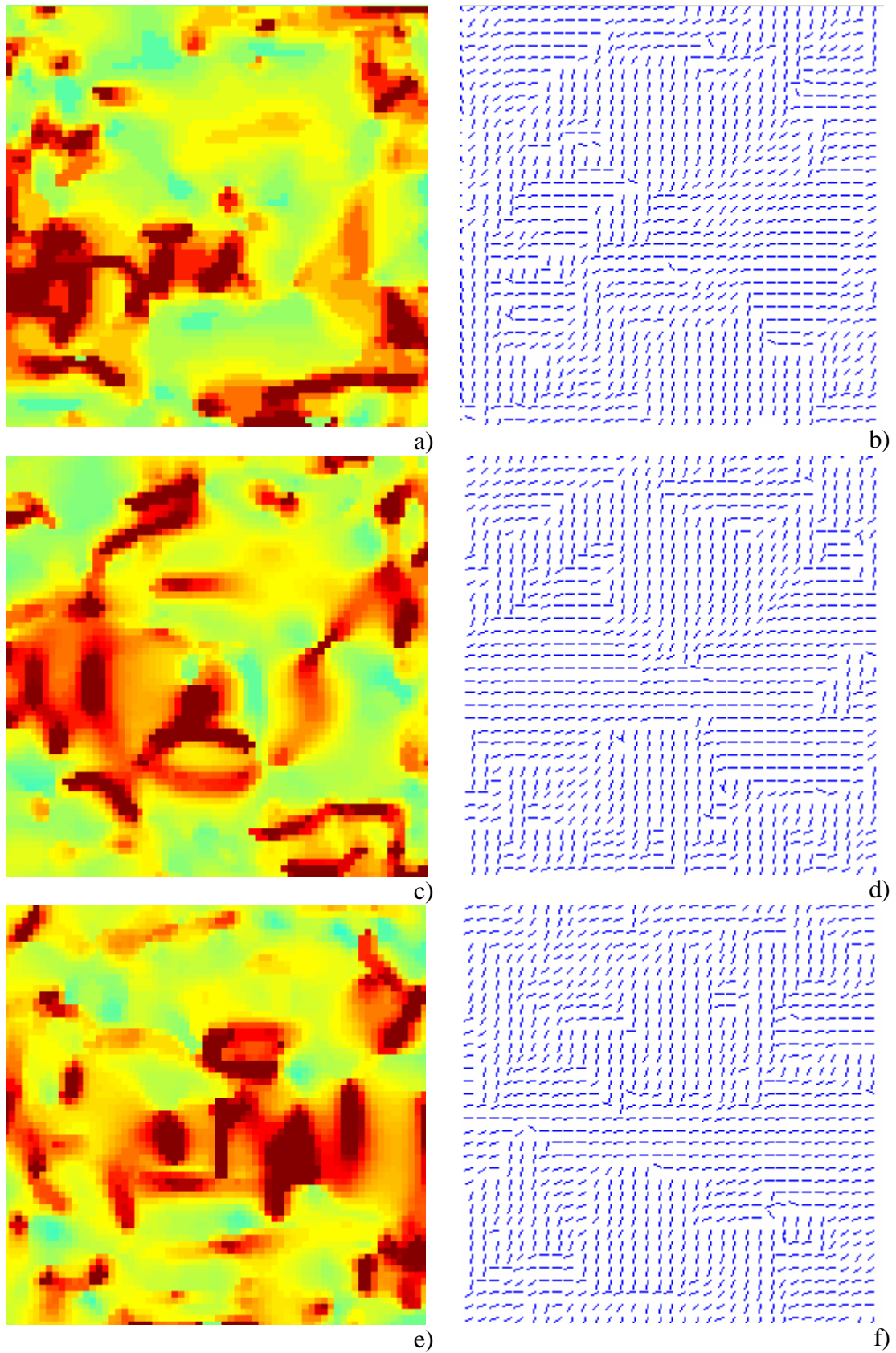


Figure 7.24: Patient Data, Principal Eigenvalues – left column, Principal Eigenvectors – Right Columns, a-b) 3rd frame, c-d) 5th frame, e-f) 11th frame

Chapter 8 – Conclusions and Future Work

8.1 Summary

Diagnosis of cardiovascular diseases at an early stage can significantly reduce the mortality rate in industrialised countries. Cardiac function has not yet been fully understood, however, it is evident that the regional assessment of myocardial contraction and perfusion is an important indicator of coronary artery disease which can lead to myocardial ischemia and infarction, and subsequently to heart failure. Moreover, it is an indication of myocardial remodelling, which is a significant factor in heart dysfunction.

The goal of cardiac imaging is to monitor 3D cardiac function with adequate temporal and spatial resolution in order to diagnose the disease and distinguish areas where the problems are. The advantage of CMRI over other imaging techniques is its potential to combine a wide variety of information, such as myocardial perfusion, wall motion, valvular flow, in one single examination. It does not expose the patient to ionising radiation, and thus it makes it possible for systematic cardiovascular screening and monitoring. The ability to image arbitrary scan planes and study flow in any direction brings the research world closer to provide clinicians with detailed in-vivo 3D cardiac cycle reconstruction. This can be later extended to an automatic way of deriving cardiac indices such as strain and deformation.

Strain is of fundamental importance in measuring cardiac regional function and myocardial viability. Its definition has been introduced by continuum mechanics that deals with the movements of materials under applied forces. Strain can be either defined as Lagrangian or Eulerian. Lagrangian strain is defined in terms of the initial length of the 3D object under deformation, while Eulerian is in terms of a length at an infinitesimally small previous time, and thus it is not constant over time. The second approximation is considered more appropriate and indicative of the cardiac mechanic function. Measuring three normal strains along the main axes and six shear strains constitutes the strain tensor. The knowledge of the strain tensor at any point of the myocardium completely defines its deformation.

Various techniques have been developed for measuring myocardial deformation based on MRI. Invasive techniques are inappropriate for standard clinical use, while there is

also doubt as to whether they alter myocardial perfusion and function. Furthermore, it is not possible to measure a large number of sites simultaneously and thus they do not have the potential of *in-vivo* monitoring. On the other hand, non-invasive techniques can be applied limitlessly in clinical use without exposing the patient to any danger.

Non-invasive techniques can be divided into two main categories. There are techniques that track material points over time based on distinct features, such as tags, while velocity field approaches integrate the Eulerian velocity, of each point, over time to yield the path of each material point and subsequently to calculate strain maps. The latter method is limited by the current technology because of the long image acquisition time needed that prevents the complete and accurate estimation of 3D myocardial deformation maps. Furthermore, the process of integration is susceptible to accumulative errors that in the noisy environment of MR scanning deteriorate the result.

MR Tagging uses a special pulse sequence to spatially modulate the longitudinal magnetisation of the subject to create temporal dark features, tags, in the image plane. The most commonly used sequence of pulses for MR tagging is SPAMM, which produces tags with sinusoidal intensity profile, which results in an overall decrease of the signal to noise ratio of the image. Later research has improved the contrast of tagging images and has added flexibility of tag spacing, thickness and high resolution. However, the main problem of tagged images is that the contrast between the tissue and the tags decreases considerably during the later phases of the cardiac cycle. Thus tracking is not possible during a complete heart cycle. CSPAMM is an innovative tagging technique for improving the contrast of tags in the image and minimise tagging fading by subtracting two tagging function with opposite flip angles. Unfortunately, the increased image quality is at the expense of scanning time because it doubles the time needed to acquire the pair of images for each frame. Furthermore, in practise the processing and tracking of tag lines required a long period of manual post-processing before HARP MRI.

HARP MRI is based on the ingenious idea that tissue deformation can be easily extracted from the local change of tag lines frequency. This information can be easily extracted from the frequency domain of the MR tagged image by filtering one spectral peak. The inverted transform of the filtered image is directly related to the apparent reference motion map, which completely characterises the apparent 2D heart motion

and relates all points within an image to their reference positions. However, phase unwrapping effects inhibit the direct motion calculation. Instead, it is comparatively easy to unwrap both the spatial and time derivative of the angle image provided by the arctan operator. Based on that observation velocity fields and strain maps can be calculated rapidly, without any human intervention.

Chapter seven investigates whether or not CSPAMM and SPAMM can be combined with HARP MRI in order to assess the myocardial motion and deformation, accurately. The combination of CSPAMM and HARP MRI can be appreciated as particularly useful for assessing myocardial deformation through out the cardiac cycle. CSPAMM provides images with better signal to noise ratio than SPAMM, while the last frames of the cardiac cycle are satisfactory and they agree well with the expected heart motion. Moreover, HARP based on SPAMM is more sensitive to spectral peak filtering, which is particularly significant in the last time frames when the central peak has enhanced considerably. Clearly, SPAMM can be used during the last time frames, where the spectral peak has been almost overcome by the DC peak and the signal to noise ratio has deteriorated considerably.

The comparison between normal volunteer and patient data verifies that HARP MRI can provide useful functional information that indicates myocardial abnormalities and dysfunction. The process is fully automatic and rapid. During the processing of data of the same sequence the software parameters, which determinate the spectral peak filtering, do not change. U_x and U_y components of velocity fields are not sensitive to registration errors between images with different tag directions, while strain maps become meaningless. The myocardial wall can be clearly discriminated from the blood pools and the outside environment, while myocardial tissue motion at the inside of the myocardial wall agrees well with what is expected through out the whole cardiac cycle. This analysis shows that HARP MRI can be easily adapted to a clinical environment with minimum cost and has the potential of accurately monitoring the heart function and detecting cardiac malfunction.

Finally, de-noising and restoration of vector fields considerably improves the visualisation and thus enhances the perception of regional myocardial contractility. Vector fields' restoration is particularly useful for the middle wall between the left and right ventricle. This region can be noisy because it is affected by the blood pools inside the right and left ventricles and it is thinner than the free wall of the left

ventricle. Furthermore, it has significant impact in the effectiveness of 2D or 3D tracking techniques that integrate velocity fields in order to estimate deformation. These techniques are susceptible to accumulate errors that can collapse the results. Therefore, vector restoration may significantly contribute to their performance.

8.2 Future Work

Future work should focus on the assessment of cardiac function near the endocardial and epicardial boundaries. These regions are noisy and measurement of deformation there is less accurate. However, they are particularly useful in early diagnosis and prevention of certain cardiovascular diseases such as ischemia and subsequently infarction. Therefore, there is the need to accurately separate the myocardial wall from the blood pools based on both anatomical and functional information. The visualisation system should be also extended to demonstrate a combination of velocity fields or strain maps with clear anatomical information in order to navigate clinicians towards the exact problematic area of the myocardium and discriminate myocardial wall regions. This would be also useful to be analysed in combination with perfusion studies.

The acquisition process is an issue that effects the accuracy of the method and imposes certain limitations in terms of tag fading, temporal and spatial resolution and motion artifacts. Systems that compensate respiratory motion are at their infancy. However, their results are promising and their use could speed up the study of cardiac mechanical properties as the image resolution would not be limited by the length of breath-hold possible. In terms of HARP MRI, acquisition speed can be reduced by scanning only the spectral peak. Furthermore, vertical and horizontal tags can be processed in parallel and thus contribute to real time visualisation of the data. This would allow a multi-slice acquisition at single breath hold and it would have great impact on the study of 3D cardiac function. The construction of 4D representation of cardiac motion with reference to any position and orientation is the ultimate goal of cardiac imaging. HARP MRI has the potential to meet this challenge.

Moreover, assessment of cardiac motion during the last frames of the cardiac cycle is limited because of the low signal to noise ratio of the images and thus minority dysfunctions in the diastolic phase may not be observed. Although, CSPAMM

successfully eliminates the central peak, it is still susceptible to spin-lattice relaxation that decreases the signal to noise ratio during the last time frames and imposes limitations to the accuracy of the process and its overall impact on statistic measurements. Further investigation should be done on this area in order to determine the exact limitations of the technique.

This investigation should also be extended to a variety of patient and normal data in order to provide a systematic record of a quantitative measure of normality and abnormality. A fuzzy system could subsequently be created to provide an automatic way of a suggested diagnosis that would have the potential of indicating the diseased myocardial regions and the extent of the damage.

Appendix – Implementation

1. Introduction

In order to fulfil the implementation requirements of this study a research tool was developed using *Visual C++ 6.0 / MFC – Dialog Based Application*. The objectives of the design was to create a flexible tool, easily adapted to various environments and expandable for further implementation and research. Although, MFC functions are used for displaying image data, special effort has been made to use pure C/C++ in order to be able to adapt the current basic classes under other interface design with minimal modifications.

Furthermore, speed and memory requirements are challenging problems when image processing systems are implemented. Comparing to *Matlab 5.2* the speed of processing has been increased more than two orders of magnitudes. Therefore, this is a further step towards the establishment of HARP MRI in clinical use and constitutes an investigation of the practical requirements for in-vivo assessment of myocardial strain and deformation.

Finally, program layout should have enough capabilities in order to require minimal source code modification when certain parameters of the scanning sequence and the raw image data have changed. This application has covered most of these parameters in terms of this project. Future upgrade versions can be easily created in order to accomplish further requirements.

In this chapter, the functionality of the interface implementation and the object oriented model behind it is described and discussed. This section can be considered as a tutorial/manual, intended to navigate those that want to use the HARP MRI application or to upgrade it.

2. Interface

2.1. Main Application

An overview of the final layout is illustrated in Figure 0.1. There are three steps before calculating and displaying velocity fields or strain maps. These are loading the text files of the filenames that contain the image data (Paragraph 7.4), using the right

parameters in the tab section (Appendix 2.2) and finally pushing the velocity or strain button to process the MR images according to the requirements posed by the input variables.

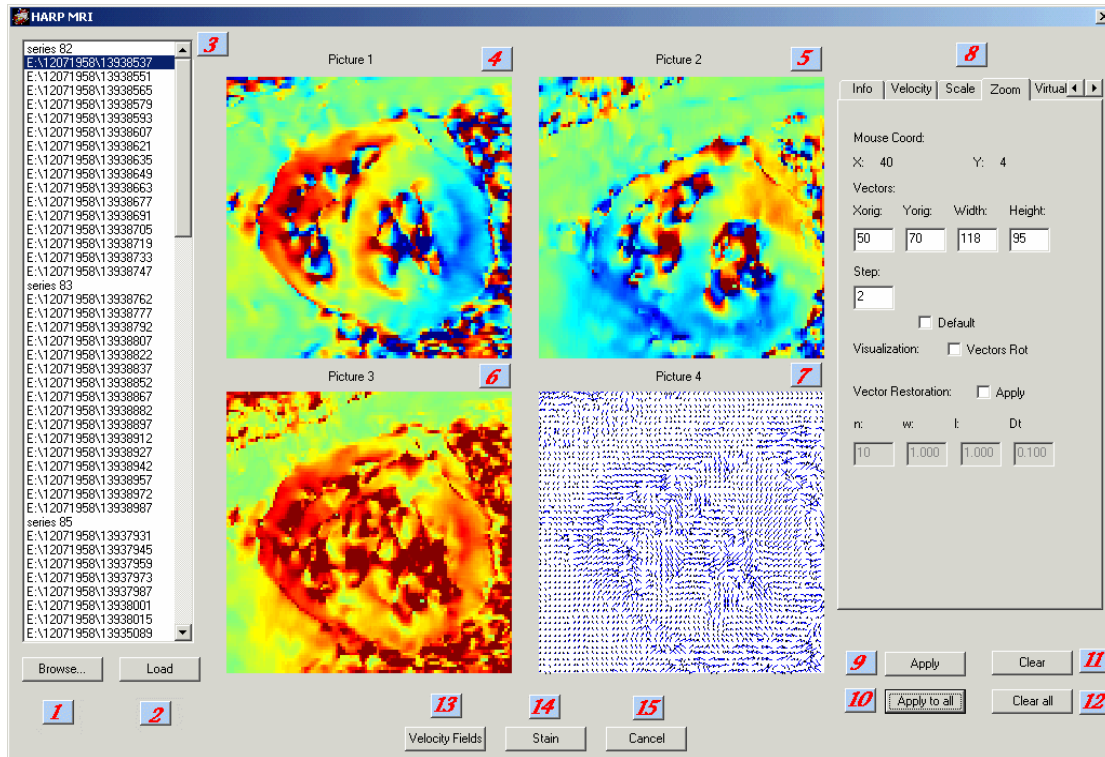


Figure 0.1: Overview of the HARP MRI application

In order to explore the functions of the *HARP MRI* application, labels with numbers have been put to each control, Figure 0.1, Figure 0.2:

1. The 'Browse...' button, label (1), raises an *Open Dialog Form*. A text file should be chosen and displayed in the panel with label 3.
2. The 'Load' button, label (2), will display the image data that are stored in the selected path in one of the available picture panels label (4) – label (7), according to the input parameters in the tabs, label (8). In the case that an error occurs while opening the data file an error message will be displayed and the displaying procedure would be aborted.
3. In the panel with label 3 the loaded text file, which is stored in a MFC class as *CListBox*, is displayed. By default the first valid path of the file is already selected, label (3). The application does not check whether or not the file has the right format. It is the user's responsibility to do so. The file should contain eight series of images which correspond to vertical – horizontal tags, CSPAMM, and

magnitude – phase data (Paragraph 7.4). Each series contains as many lines as the total phases. Therefore, each line is a time frame sorted from the initial (end diastole) to the final.

4. In panels with labels (4) – label (7) there is the capability of simultaneously displaying four images. Panel with label (4) has the ability to zoom pictures by push down the left mouse button at the top-left point and release it at the bottom-right point of the region of interest or vice versa. If there is a picture in 7th panel it will be automatically zoomed. The rest of the pictures can be zoomed only by using the tab parameters, label (8).
5. Label with number 8 illustrates the tab panel, which is used for both input and output purposes. There are several parameters that affect both displaying and processing of the image data. The user should be aware that those parameters that control display do not effect image processing and therefore they do not change the image information.
6. The ‘*Apply*’ and ‘*Apply to all*’ buttons, labels (9), label (10), force re-display of the image data, using the parameters defined in the tab controls, label (8), either to one pre-selected picture panel or to every picture panel label (4) – label (7), respectively. There are some parameters that do not affect display and the image data needs to be reprocessed. This will be better understood in the next paragraph where tab controls and their function are illustrated.
7. The ‘*Clear*’ and ‘*Clear to all*’ buttons, labels (11) – label (12), clear either the pre-selected or all picture panels, (label 4-5-6-7), respectively, by drawn a white/null rectangle on them. These buttons do not clear memory, therefore if there is image data loaded it can be displayed again by simply pushing the ‘*Apply*’ or ‘*Apply to all*’ button, label (9) – label (10).
8. ‘*Velocity Fields*’ and ‘*Strain*’ buttons, labels (13) – label (14), are the basic functions to calculate Velocity Fields and Strain maps, respectively. They use the input data from the tab panel label (8) and the path-filenames from the text panel label (3) to load image data and process those it according to HARP MRI principles (Chapter 5). Therefore, tab parameters should be carefully chosen to give reasonable results.
9. The ‘*Cancel*’ button, label (15), exits the program.

Finally, when the *HARP MRI* application starts the ‘*Velocity Fields*’, ‘*Strain*’, ‘*Apply*’, ‘*Apply to all*’ and ‘*Load*’ buttons are disabled. ‘*Velocity Fields*’, ‘*Strain*’ and ‘*Load*’ buttons are enabled when a text file is loaded using the ‘*Browse...*’ button. ‘*Apply*’ and ‘*Apply to all*’ buttons are enabled when the first image is displayed.

2.2. Tab Controls

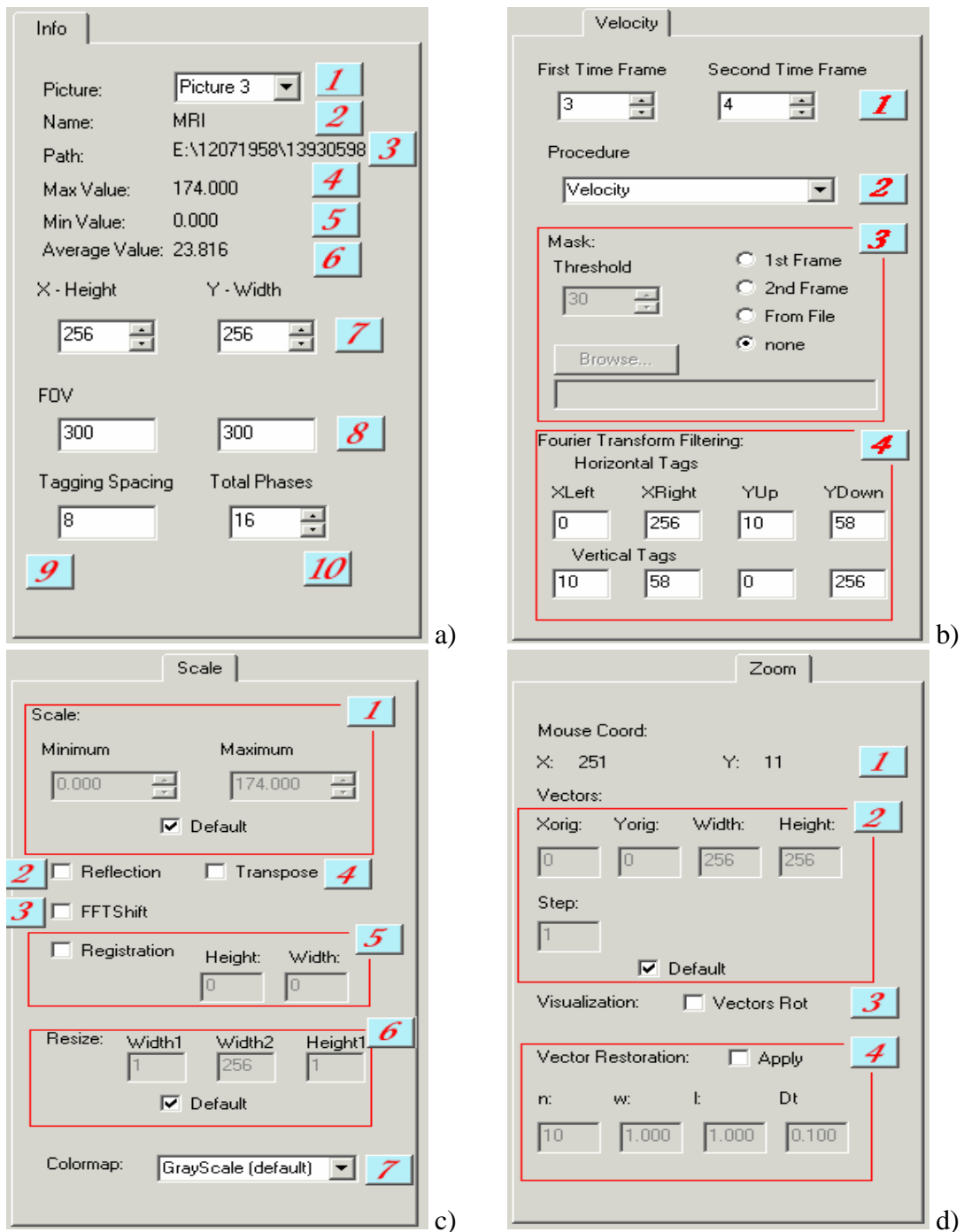


Figure 0.2: a) Info Tab, b) Velocity Tab, c) Scale Tab, d) Zoom Tab

In Figure 0.2 the four tab controls used in this application are illustrated:

Info Tab:

Generally, '*Info Tab*' contains both input and output information for the image data that are displayed:

1. The *ComboBox*, label (1) is both input and output variable. It indicates the picture panel where an image would be displayed when the '*Apply*' or '*Load*' buttons are pushed, but it is also refreshed when an image is displayed in a pre-decided picture panel.
2. The *Static Text* variables with labels (2-3-4-5-6) are used as output variables only, which contain information about the image that is displayed in the picture panel indicated by the *ComboBox*, label (1). The '*Name*', such as '*MRI*', '*Phase*', '*Magnitude*', '*Velocity*' and so on, characterises the data file that is displayed. The '*Path*' designates the entire filename, while the '*Max Value*', '*Min Value*' and '*Average Value*' indicate the max, min and average value of the image data. These values are refreshed when an image is displayed and can also be forced to be refreshed by choosing an image, label (1), and pushing the '*Apply*' button.
3. The *Edit Controls*, specified by label (7) are input variable that indicate the *height* (*X*) and *width* (*Y*) of the image data that will be loaded from disk. Obviously, they should be positive integers. The current version of HARP MRI application is not fully extended and tested for image data that do not have the same dimensions for both *x* and *y* axes. Furthermore, in the case that image data dimensions are not factors of four the display function '*StretchDIBits*' can not operate properly. However, these limitations can be easily overcome without major changes to the implementation design.
4. Finally, the *Edit Controls*, specified by label (8) – label (10), are also user defined variables that indicate the Field of View, the space in mm between tags and the total number of time frames, respectively.

Velocity Tab:

'*Velocity Tab*' contains basic information for processing MR data to produce velocity fields and strain maps using the principles of HARP MRI, (Chapter 5).

1. The *Edit Controls* indicated by the label (1) define the two frames that are needed to calculate velocity fields. In the case of strain only the first time frame is considered.
2. The label (2) illustrates the *Combo Box*, which determines the layout of the processing in order to check intermediate steps. Currently, eleven such steps are implemented: ‘*Load Frame 1 (magnitudes)*’, ‘*Load Frame 1 (phases)*’, ‘*Complex Frame 1 (ABS)*’, ‘*Load Frame 2 (magnitudes)*’, ‘*Load Frame 2 (phases)*’, ‘*Complex Frame 2 (ABS)*’, ‘*CSPAMM (ABS)*’, ‘*FTW (ABS -SHIFT)*’, ‘*Filtering (ABS-SHIFT)*’, ‘*IFFTW (ABS)*’, ‘*Preview Mask*’ and ‘*Velocity*’. Each one corresponds to each one step for calculating velocity fields, (Paragraph 5.3 – Chapter 7) and thus the layout will be the respective images.
3. Label (3) is assigned to the mask controls. A mask can be used to eliminate noise, (Paragraph 7.7). This can be either calculated from the first or the second frame or it can be loaded from a text file. The text loaded function is well written in terms of dynamically manipulating memory without prior knowledge of the text file size. However, for the loaded data to be combined conveniently with velocity fields the mask should be composed from zeros and ones. These values will be directly multiplied by the corresponding velocity fields to provide the final results.
4. Finally, the Fourier Transform Filtering, label (4), defines the corner points of the rectangle filter used to isolate the spectral peak from the rest of the spectrum, (Paragraph 5.2.4). The specified coordinates correspond to the real Fourier Transformed matrix, without *FFTShif*. The *X-Y* variables are with reference to the first element of the image matrix and specify width and height, respectively. The resulting image will keep data stored inside the specified rectangle and put zeros everywhere else.

Scale Tab:

‘*Scale Tab*’ is used as display variables input, apart from the ‘*Resize*’ part, label (6).

1. The *Edit Controls* with label 1 are used for scaling the displaying data. When the *Check Box* is checked the minimum and maximum values of the image data are used for scaling, otherwise the data are scaled between the values that are indicated.

2. The ‘*Reflection*’, ‘*Transpose*’ and ‘*FFTShift*’ Check Boxes, label (2) – label (4) are used as displaying input variables and they cause reflection, transposition and FFT Shift, respectively. The image data is transformed each time they are displayed when the *Check Box* is checked. Therefore, when the ‘*Apply*’/ ‘*Apply to all*’ buttons are used twice the images would have their original form.
3. ‘*Registration*’, label (5) is used when there is mis-registration between the horizontal and the vertical tags, (Paragraph 7.4). It is a user defined variable and applies only to vertical tags, indicating the height and width in image data coordinates that the image should be moved in terms of its first element in order to match the corresponding horizontal tags frame. These values can be either positive or negative integers.
4. Using the ‘*Colormap*’, label (7), greyscale or a 256 colour-map can be chosen.
5. Finally, ‘*Resize*’, label (6), dramatically affects the performance of the system. The user can decide the region of interest and resize the images to be in that size, saving memory and time. The images are loaded normally according to the X-Y coordinates (‘*Tab Control*’, label 7) but they are resized for further processing. This control deletes the current image data and creates new data according the dimensions given by the Edit Controls of ‘*Resize*’. Images are always square. The input values specify the position of the upper left and right corner of the region of interest.

Zoom Tab:

‘Zoom Tab’ is used to define zoom parameters and also to control and restore vector fields:

1. The static controls with label (1) indicate the mouse coordinates with reference to the upper left corner of the 1st picture panel of the *HARP MRI* application. These controls are only refreshed when the mouse is above the 1st picture panel.
2. Label (2) is used for both input and output and defines the X-Y (width-height) image coordinates of the upper left corner of the zoomed area, its height and its width. The last parameter ‘*Step*’ is an input variable that is used for visualizing

vector fields. Vectors are drawn either to each image pixel ($Step = 1$) or at specified columns and rows determined by the value of 'Step'.

3. When the checked box labelled 3 is on then the vectors are displayed using the transformation: $X = U_y$ and $Y = -U_x$, and they always look like they are rotating around the origin, Figure 0.3.
4. Finally, 'Vector Restoration', label (4), is used to determine whether or not vector restoration will apply, (Chapter 6) and to define its parameters: n is the number of iterations, w is the weight of neighbour points, l is the weight of the pixel under consideration and Dt is rate of changing the initial vector.

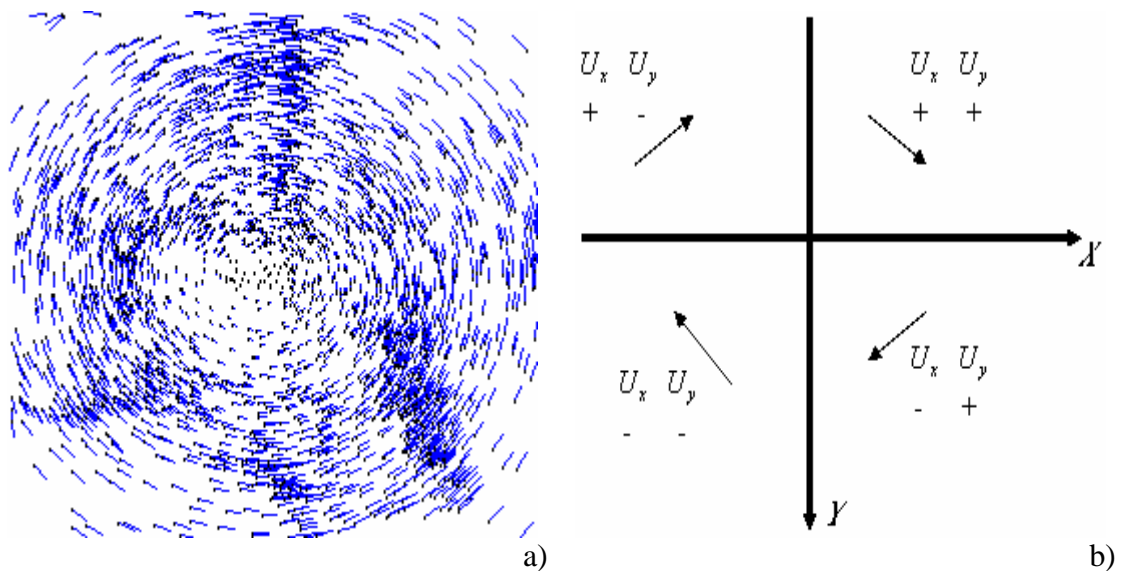


Figure 0.3: Different Visualisation Scheme

3. Description of the Object Orientated Model

3.1. Manipulating MRI Image Data

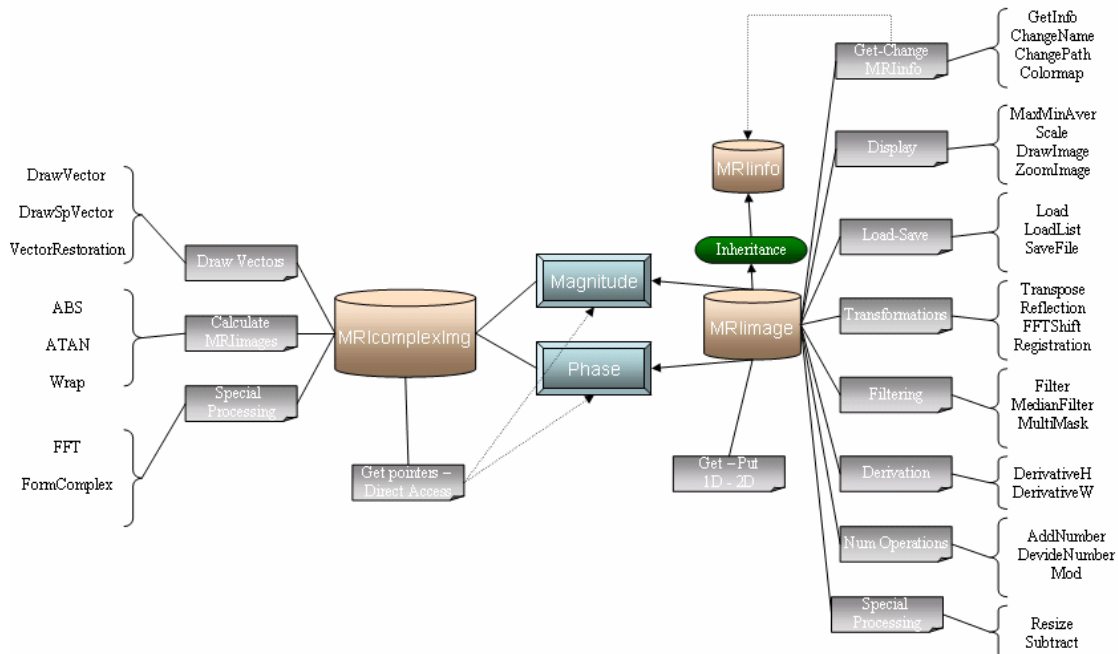


Figure 0.4: Object Orientated Model of Manipulating MRI Image Data

MR images usually can be considered as complex data that are constituted from the *magnitude* and the *phase* images. However, there is also the need to define a class that is able to manipulate data that are not complex. There are processes that affect both magnitude and phase structures, others that use them to calculate a third structure, such as the absolute value, and processes that handle only one image at a time, such as the displaying of colour-maps. The simplest and most efficient way of implementing these requirements is by creating a class, ‘*MRComplexImg*’ that integrates two similar ‘*MRImage*’ classes.

Clearly, an ‘*MRImage*’ class is both a dynamically stored structure that contains image data and a number of functions that can be used to transform this image, while ‘*MRComplexImg*’ contains two pointers that are instantiated dynamically to point to two ‘*MRImage*’ classes and can combine data from both sides.

Figure 0.4 illustrates the basic model of the *HARP MRI* application in terms of data manipulation. Consider first the right part of the diagram in Figure 0.4. ‘*MRImage*’

class inherits information from a structure called *'MRIinfo'*. This structure has been designed to contain information with regard to the image dimension, file path, name, Field of View, Tagging Spacing and so on. There are member functions that can get or change this information.

There are various functions that are used in order to load, process, save and display data. Special consideration deserves the displaying function used from *'MRIimage'* objects. *'MRIMinMaxAver'* and *'MRIScale'* are member functions that instantiate necessary information used by the *'MRIDrawImage'* and *'MRIZoom'* functions and thus they should always precede the drawing functions. An interesting point is the *'MRIResize'* function because it deletes and recreates the class data in order to reduce their size. The image data are stored in a single dimension matrix. The functions *'MRIGet'* and *'MRIPut'* can retrieve and store data, respectively, by providing easy access to them either as 1D or 2D matrixes.

Finally, the left part of Figure 0.4 indicates the member functions specially created to manipulate complex data. Most of the functions implemented for *'MRIimage'* objects have been expanded for *'MRIcomplexImg'* objects too. However, additional flexibility is added by obtaining the pointers of the phase and magnitude objects using the *'MRIGetPointer'* function. Most of the effort was concentrated on the Drawing functions that display vectors. They are the most challenging as various parameters should be considered in terms of screen and matrix coordinate transformation, scaling, zooming, window resizing and so on.